Dissertation

submitted to the

Combined Faculties of the Natural Sciences and Mathematics

of the Ruperto-Carola-University of Heidelberg, Germany

for the degree of

Doctor of Natural Sciences

Put forward by

Marcel Hellmann

born in: Solingen, Germany

Oral examination: 2011/06/01

Anomalous Diffusion and Non-classical Reaction Kinetics in Crowded Fluids

Referees: **Prof. Dr. Dieter W. Heermann**
Institute for Theoretical Physics, University of Heidelberg

Prof. Dr. Matthias Weiß
Experimental Physics I, University of Bayreuth and
BIOMS Group Cellular Biophysics,
German Cancer Research Center Heidelberg

Zusammenfassung

Diese Arbeit beschäftigt sich mit den Mechanismen und den Auswirkungen von anomaler Diffusion in dichten Flüssigkeiten unter Einsatz von Computersimulationen.
Um den zugrunde liegenden Mechnismus von Subdiffusion aufzuklären, betrachten wir die gemittelte Form aufgezeichneter Trajektorien als ein potentielles Kriterium, mit dem häufig diskutierte Modelle zuverlässig gegeneinander abgegrenzt werden können. Unsere Simulationen zeigen zudem, dass die Bestimmung dieses Mechanismus' durch inhärente Messfehler der experimentellen Daten erschwert wird.
Wir schlagen ein partikelbasiertes Modell für das Zytoplasma vor: Es vereint eine weiche Abstoßung und schwache Anziehung zwischen globulären Proteinen verschiedener Größe. Unter diesen Bedingungen zeigen Simulationen transiente Subdiffusion der Partikel, die auf experimentellen Zeitskalen jedoch in normale Diffusion übergeht. Realistischere Modelle müssen daher mehr Details über die beteiligten Wechselwirkungen berücksichtigen.
Im zweiten Teil dieser Arbeit werden mesoskopische, stochastische Simulationen eingesetzt, um die Auswirkungen von Subdiffusion auf biochemische Reaktionen zu untersuchen. Wegen ihrer kompakten Trajektorien segregieren subdiffusive Reaktanden mit der Zeit. Dies führt zu anomaler Kinetik, die stark von klassischen Theorien abweicht. Andererseits kann Subdiffusion die Produktivität eines mehrstufigen Prozesses deutlich erhöhen, wenn die reaktiven Partikel in einem Zwischenschritt dissozieren und erneut assoziieren müssen.

Abstract

This thesis investigates the underlying mechanism and the effects of anomalous diffusion in crowded fluids by means of computer simulations.
In order to elucidate the mechanism behind crowding-induced subdiffusion we discuss the average shape of tracer trajectories as a potential criterion that allows to reliably discriminate between frequently proposed models. Our simulations show that measurement errors inherent to single particle tracking generally impair the determination of the underlying random process from experimental data.
We propose a particle-based model for the crowded cytoplasm that incorporates soft-core repulsion and weak attraction between globular proteins of various sizes. Under these prerequisites simulations reveal transient subdiffusion of proteins. On experimental time scales, however, diffusion is normal indicating that realistic, microscopic models of crowded fluids require further detail of the relevant interactions.
In the second part of this thesis, the impact of subdiffusion on biochemical reactions is studied via mesoscopic, stochastic simulations. Due to their compact trajectories subdiffusive reactants get increasingly segregated over time. This results in anomalous kinetics that differs strongly from classical theories. Moreover, for a two-step reaction scheme relying on an intermediate dissociation-association event, subdiffusion can substantially improve the overall productivity because spatio-temporal correlations are exploited with high efficiency.

Contents

List of Figures

List of Tables

Chapter 1

Introduction

1.1 Motivation

Chemical reactions are the basis of all biological processes. Many of these reactions ultimately rely on the physical encounter of two or more proteins in the cell and are hence fundamentally influenced by

1. *diffusive transport* of the participating agents,

2. their potentially low copy number (*stochasticity*).

The interior of the cell resembles a tremendously complex and *crowded* medium. Being the most abundant macromolecules, proteins occupy approximately 20 to 40% of the total volume. The dynamics of an arbitrary protein is changed by numerous other proteins around (*crowders*) into an *anomalous diffusion*, i.e. the dynamics is not only slowed down but changes qualitatively. In the modeling of chemical reactions, the effect of crowding has been widely neglected so far. Consequently one part of this work deals with the simulation of reaction-subdiffusion systems. Furthermore, stochastic aspects due to the particle character of reactants are studied as they may lead to dramatically different results as compared to the established (classical) mean-field approaches.

There are different models for anomalous diffusion that can be used to simulate particle trajectories. The particular mechanism realized in complex, crowded fluids like the interior of a cell is still a matter of debate. During the past few years, increasing evidence has been collected that viscoelasticity underlies the observed subdiffusion but a conclusive answer is still lacking. One way to address this issue is to statistically analyze the behavior of individual tracer trajectories from microscopy experiments. Along this line, a criterion is developed that allows to reliably decide which of the various models for subdiffusion describes the observed behavior best.

1.2 Chemical Reactions in the Cell

This section shall provide a brief introduction to the biology and biochemistry of a cell. The focus is on terminology and basic concepts. If no explicit citation is given,

the presented facts are textbook knowledge taken from the celebrated "Molecular Biology of the Cell" by B. Alberts *et al.* [1].

1.2.1 The Cell

In physical terms, a *living organism* is superficially an open, thermodynamic system that maintains a state of low entropy by converting energy and matter from the outside in a self-organized way. In biological terms, the attribute living is assigned to entities that conduct a stable *metabolism*, dynamically adopt to environmental changes, reproduce themselves, and undergo evolution[1]. Cells can be considered as the "atoms of life" in the sense that the smallest organisms meeting these criteria consist of just a single cell. On the other end of the scale, "macroscopic" organisms like mammals are agglomerates of up to 10^{13} highly specialized and interacting cells.

From the perspective of life the cell is basic, but in fact it resembles a highly complex entity. Essentially, it can be considered as a reaction vessel confined by a semipermeable membrane that contains thousands of different chemicals. These give rise to the life-relevant processes by a complicated network of reactions and interactions. The cell's outer boundary is the *plasma membrane*, formed by a double layer of lipids. It separates the interior, the *cytoplasm*, from the outside, the *extracellular space*, while still allowing for a strictly regulated exchange of molecules between these two domains. One can distinguish between *prokaryotic cells* that contain no internal subcompartments and *eukarytic cells* that possess a sophisticated internal organization, cf. Figure 1.1. This includes membrane enclosed subcompartments (e.g. mitochondria, nucleus, Golgi apparatus) and a vast network of filaments and tubules. Prokaryotic cells are evolutionary older, and members of this family are exclusively single-cell organisms. The *Escherichia coli* bacterium resembles the best studied model organism among prokaryots and hence serves as the prototypical experimental system. Eukaryotic cells, on the other hand, form single- (e.g. yeast, protists) and all higher, multicellular organisms comprising animals, fungi, and plants. Their complex inner structure involves the above mentioned system of filaments and tubules, the *cytoskeleton*, which determines the shape of the cell. In contrast to the skeleton of vertebrates, this structure is highly dynamic and allows the cell to flexibly change its shape and even to move on a substrate.

Cells contain a tremendous variety of molecules that ranges from simple ions (e.g. K^+, Na^+, Ca^{2+}, Cl^-) over small metabolites like sugars (e.g. sucrose, ribose) and lipids (e.g phospholipids in the membranes) to large macromolecules. These chemicals are dissolved in water that contributes 70% of the cell's weight. Biological macromolecules are of special interest since they constitute a domain of unimaginable versatile chemicals that make life possible in the first place. They consist of a sequence of simple repeating units (*monomers*) that form a chain (*polymer*) with emergent properties. The three prominent families of biological polymers are polysaccharides, nucleic acids, and proteins, Table 1.1. Proteins in particular can be considered as

[1]The given definition of life suffices for the context of this work. Actually a more precise and universal definition of life is still vividly debated, see for example [2]

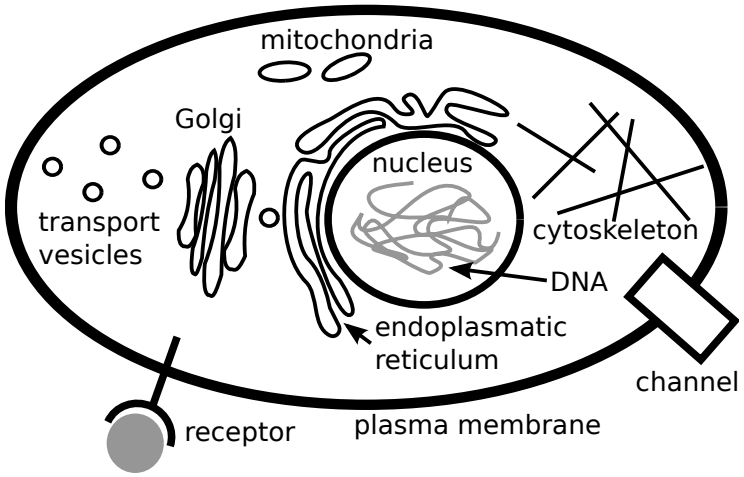

Figure 1.1 Sketch of an eukaryotic cell. The *cytoplasm* is separated from the outside by the plasma membrane. In contrast to a prokaryotic cell, it is organized in membrane enclosed subcompartments, so called *organelles*. The mitochondria, for example, host the respiratory chain that converts the energy contained in nutrients. The *nucleus* contains the heredity information as a long DNA polymer. The filamentous cytoskeleton provides structural integrity.

"tools" that keep the cellular "machinery" running. They do this by performing a wide variety of tasks: *Enzymes* are highly efficient catalysts which promote reactions that otherwise would take place too slowly or never. *Motor proteins* generate forces, *structural proteins* build up the cytoskeleton. *Membrane-resident transporters* selectively exchange molecules between cytoplasm and extracellular space. This list could be continued and the crucial importance of proteins is reflected in their abundance: They contribute 18% (15% in *E. coli*) to the total weight of a cell which is by far the highest fraction of any chemical.

family	monomer	example
polysaccharides	sugar	glycogen (energy storage in liver cells)
nucleic acid	nucleotide	DNA, RNA (carrier of heredity information)
proteins	amino acid	GFP (green fluorescent protein)

Table 1.1 The three major families of macromolecules found in cells.

1.2.2 Basic Biochemistry

All life-relevant processes in the cell are based on chemical reactions. Metabolism, i.e. the turnover of external energy and material, relies on a highly complex network containing an unimaginable number of reactants, intermediates, and products. To occur spontaneously, many of the involved reactions would actually require very high temperatures as compared to the regime where life is possible. This holds, especially, for the formation, breaking and modification of covalent bonds. These reactions require much higher energies than provided by thermal energy $k_{\mathrm{B}}T$ under physiological conditions[2]. In these cases, enzymes serve as highly specific and tremendously efficient *catalysts*. They lower the activation barrier so that reactions take place with sufficient rapidity at ambient temperature. Often an enzyme is specialized to assist in a very particular reaction. However the question arises how it identifies the correct agents among the plethora of chemicals in the cell. Enzymes, and proteins in general, bind to other chemical agents (*ligands*) in a non-covalent manner, i.e. by hydrogen, ionic, or van der Waals bonds. Hence, a single bond can easily break due to thermal fluctuations, but when many act in a concerted manner, cooperative effects eventually lead to a tight association. Then the molecules are said to have a high *affinity* to each another. The opposite case, i.e. association to a "wrong" ligand, corresponds to low affinity and thus weak and short-lived binding. Consequently, the large difference between binding affinities provides a reliable means to provide specificity.

An ubiquitous forward-backward reaction pair that is catalyzed by enzymes is the *phosphorylation/dephosphorylation*, cf. Figure 1.2: A phosphate group is covalently attached to or removed from a particular amino acid side chain of a protein. Enzymes that catalyze a phosphorylation reaction are called *kinases* and their counterparts are *phosphatases*. The addition/removal of phosphate groups regulates protein function in eukaryotic cells: Since the phosphate ion carries two negative charges, its presence can induce major conformational changes in the protein, e.g. when positively charged residues are attracted to the phosphorylated site and negatively ones are repelled from it. By such a structural change, new binding sites may emerge that enable the modified protein to act as an enzyme itself. On the other hand, the phosphate can be part of a structure that serves as a recognition site for other proteins. Thus the phosphorylation may also trigger the formation of protein complexes that eventually provide the desired functionality. Vividly spoken, (de)phosphorylation reactions can switch a protein on and off. This conceptually simple mechanism is actually of central importance: According to estimates one third of all proteins in a typical mammalian cell incorporate a kind of phosphorylation-switch.

It has been stated above that the association of an enzyme E to its substrate S represents the first step in any enzymatic reaction. In the following we will focus on a frequently applied model reaction , the so called *Michaelis-Menten scheme* for

[2] "Physiological conditions" refers to a tempretaure of $T = 37\ ^{\circ}\mathrm{C} = 310\ \mathrm{K}$. Then the thermal energy amounts to $E_{th} = k_{\mathrm{B}}T = 4.28 \times 10^{-21}\ \mathrm{J} = 0.027\ \mathrm{eV}$. For comparison: A typical covalent bond has an energy of several eV.

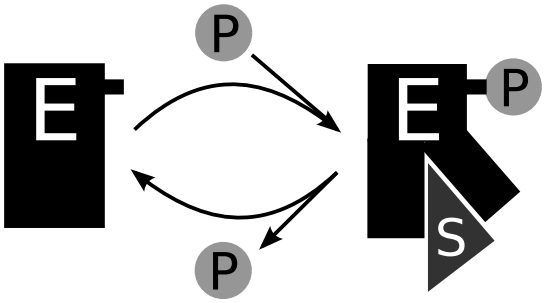

Figure 1.2 Sketch of a (de)phosphorylation cycle. The enzyme E is inactive when no phosphate is bond (left). The covalent attachment of a phosphate (P) by a kinase (not shown) induces structural changes that transfer E to its active state (right). Consequently it becomes able to bind and act on its substrate S. If a phosphatase removes the phosphate from E, it returns to its quiescent state.

enzyme-catalyzed reactions:

$$\mathrm{E} + \mathrm{S} \underset{k_2}{\overset{k_1}{\rightleftharpoons}} \mathrm{C} \overset{k_3}{\rightarrow} \mathrm{E} + \mathrm{P} \; . \tag{1.1}$$

The enzyme and substrate first form an intermediate complex C with rate k_1 that may either decay again with rate k_2 or lead to a reaction with rate k_3 releasing the enzyme and the product. This model assumes that the production step can be reduced to a single rate-determining reaction and is restricted to one intermediate complex. For example, E could phosphorylate its substrate S that consequently assumes its active form P. The advantage of the catalysis lies in the rate k_3 which is typically several orders of magnitude faster than the spontaneous rate of $S \rightarrow P$ at ambient temperature.

When investigating enzyme kinetics one is interested in the catalytic reaction rate $v = k_3[C]$, where $[\,\cdot\,]$ stands for concentration. The approach of Michaelis and Menten assumes that, after mixing of E and S, the concentration of C rapidly reaches a nearly constant *steady-state* value given by

$$k_2[C] + k_3 = k_1[E][S] \, . \tag{1.2}$$

Straightforward calculations give the relation between $[C]$ and the total enzyme and substrate concentrations $[E_0]$ and $[S]$:

$$[C] = \frac{[E_0][S]}{K_m + [S]} \quad \text{with} \quad K_m \equiv \frac{k_2 + k_3}{k_1} \, . \tag{1.3}$$

With this the *Michaelis-Menten equation* for the reaction rate is obtained

$$v = \frac{k_3[E_0][S]}{K_m + [S]} \, . \tag{1.4}$$

In the limit of very high substrate concentration, practically all enzymes will be bound in a complex. Hence there is a maximum reaction rate $v_m = k_3[E_0]$ and one rewrites the Michaelis-Menten equation:

$$v = \frac{v_m[S]}{K_m + [S]}\,. \tag{1.5}$$

K_m resembles an approximate measure of the substrate-enzyme affinity since it is equal to $[S]$ at $v = 0.5v_m$. Generally, the lower K_m the tighter the enzyme binds to the substrate. k_3 is also called *turnover number*. For $[S] \ll K_m \Rightarrow [E] \approx [E_0]$ and the reaction rate becomes $v = k_3/K_m[S][E]$. In other words, the ratio k_3/K_m gives the rate constant for the reaction between free E and free S. For some enzymes ("perfect enzymes") the catalysis is diffusion-limited, i.e. k_3/K_m takes on a maximum value between 10^8 and 10^9 $\mathrm{s}^{-1}\mathrm{M}^{-1}$ that is determined by the rate of E-S collisions. This kind of analysis is widely applied in the field of (*in vitro*) enzyme kinetics, but a debate has arisen whether the underlying assumptions are generally met in the cell , see e.g. [3, 4].

1.2.3 Signaling and Biochemical Networks

One demanding task a cell faces frequently is the adaption to a constantly changing environment. Vividly spoken, it has to "sense" critical changes, for example the depletion of a nutrient, and respond accordingly, for example by promoting metabolization of an alternative nutrient. In more technical terms, the cell has to receive and process signals from the outside. Moreover, in a multicellular context of a tissue, cells have to communicate in order to act in a concerted manner. This means they must not proliferate and divide in an arbitrary, unsynchronized fashion that would be hazardous for the integrity of the tissue. To this end, cells exchange chemical signals like growth factors. Actually, if a cell looses sensitivity to certain signals and behaves independently of its surrounding this is one characteristic of cancer [5]. One emphasis of cancer research is hence on biochemical signal processing. In this field the focus shifts away from single reactions to a system view on biochemical *networks*. Owing to the overwhelming complexity, this approach requires computer-assisted modeling to interpret experimental data. The used terminology is borrowed from technical signal processing. As artificial signal processing devices, biochemical networks are built of basic modules like switches and feedback loops. The components of the "circuits" are realized by reaction schemes, like a (de)phosphorylation cycle that emerges from the interplay of a kinase and a phosphatase [6].

The pathway of the epidermal growth factor receptor (EGFR) represents a thoroughly studied example of a signaling cascade in eukaryotic cells and furthermore is a target of cancer therapy [7]. It illustrates the complexity and modularity of biochemical networks that are necessary to translate an extracellular signal to a cellular response in terms of a changed gene expression pattern. Here we will only roughly describe the basic concepts and omit the overwhelming detail of the involved proteins and their interactions, see Figure 1.3: In the first step, the

signaling agent (EGF) binds to a membrane crossing receptor protein (EGFR). This induces conformational changes in the receptor and a tyrosine kinase domain on the cytoplasmic side is activated that phosphorylates specific tyrosine residues on a small set of intracellular signaling proteins, the so called *second messengers*. This is the onset of the next layer of signal processing. As the signal is transported further downstream towards the genome, it gets more and more interconnected with other cellular pathways. In this way various signals can be integrated to a coherent biochemical "picture" that consequently triggers an adequate adaption of the cell.

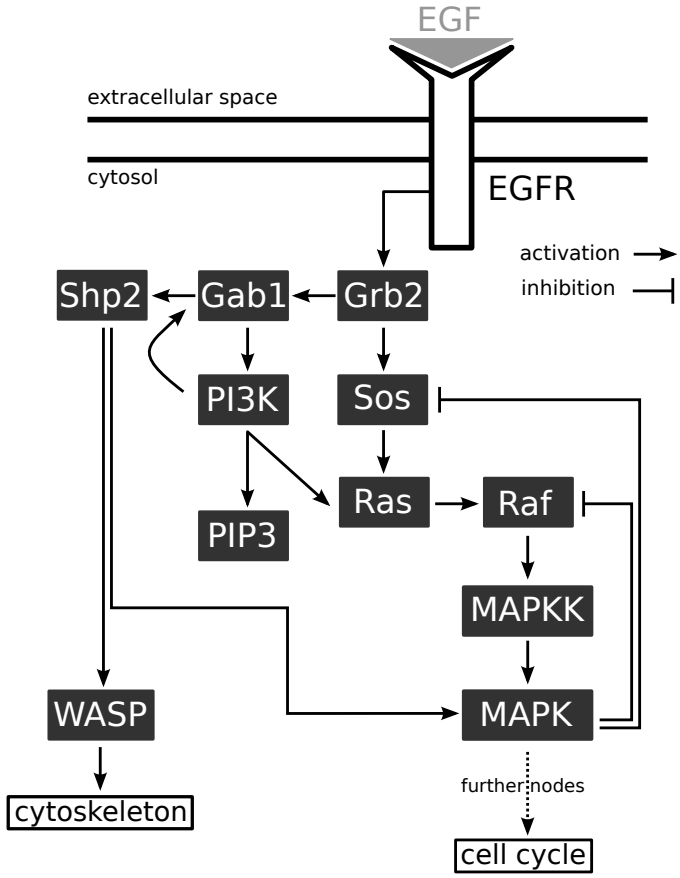

Figure 1.3 A small part of the signal processing network that originates in the epidermal growth factor receptor (EGFR). Each dark shaded box corresponds to an enzyme species or family addressed by its abbreviated name (e.g. Sos stands for "son of sevenless"). The interactions between the proteins are given in terms of activation and inhibition via (de)phosphorylation. Some components of this network are shared by other pathways to provide crosstalk between different signals.

In the context of the EGFR pathway an the mitogen-activated protein kinase (MAPK) cascade deserves further explanantion: This module is ubiquitous in eu-

karyots and it is involved in various physiological processes [1, 8]. MAPK has two sites that may be phosphorylated by a kinase and hence it is an example for a *multisite protein phosphorylation* motif [9]. One important distinction in this context is between *distributive* and *processive* kinases. Processive kinases may phosphorylate multiple sites on a protein while in a complex with the substrate whereas distributive kinases require perpetual association-dissociation cycles. Depending on the mode of the involved enzymes and the possible phosphorlation patterns etc. a vast variety of signal processing modules may be realized. The MAPK cascade, in particular, consists of three layers, where in each layer a kinase turns on the kinase of the next layer by phosphorylation, cf. Figure 1.4. To be fully active, MAPK must carry phosphates on both phosphorylation sites. This is highly specifically performed by the upstream *MAPK-kinase*, which in turn is activated by the *MAPK-kinase-kinase* (called *Raf* in the context of the EGFR pathway, cf. Figure 1.3). This scheme can, for example, give rise to bistability [10] and ultrasensitive response [11].

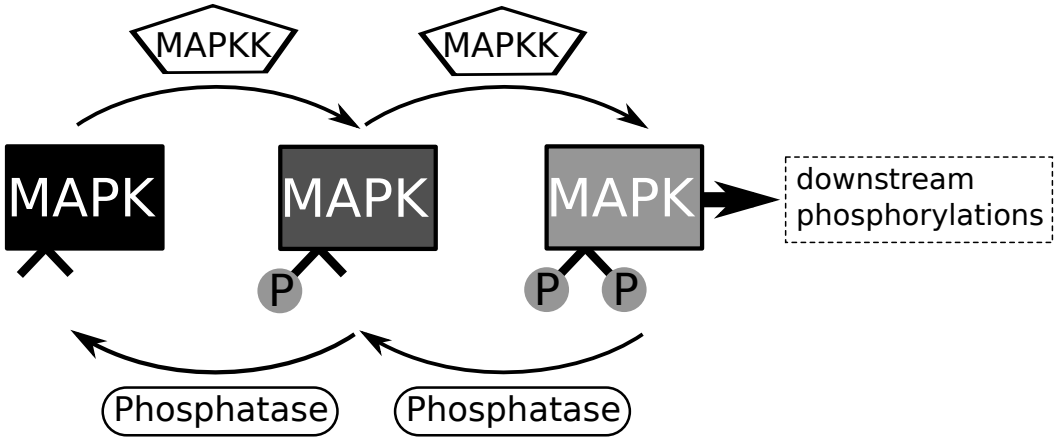

Figure 1.4 Sketch of the mitogen-activated protein kinase (MAPK) phosphorylation cycle as an example for multi-site phosphorylation. MAPK possesses two phosphorylation sites and in order to be active and trigger downstream signaling, both sites must have a phosphate bound. Both phosphorylation reactions are catalyzed by MAPK-kinase (MAPKK) which works antagonistically to phosphatases that switch MAPK off.

1.2.4 Macromolecular Crowding

The classical approaches for modeling biochemical reactions typically assume a dilute solution of reactants in aequous solution [12, 13]. This, of course, neglects the complex internal organization of eukaryotic cells and the huge number of macromolecules that are present without taking part in a particular reaction. For the reaction of interest, these other agents appear as inert *crowders* which, firstly, reduce the available space by their volume, and secondly, bind transiently to the reactants with low affinity.

Both aspects alter the reaction kinetics as the accessible volume for the reactants is smaller, and their diffusional transport may be qualitatively modified to *anomalous diffuion*, see Section 1.3.

The cytoplasm of living cells thus resembles an example of a *crowded* or *complex fluid* [14]. Estimates state that macromolecules occupy 20 to 40% of the cell volume [15] and hence the effects of crowding on biochemical reactions must be appreciated in models and experiments [16], cf. Figure 1.5 (a). This also applies to processes on the cellular membrane, where more than 20% of the total area can be occupied by proteins [17].

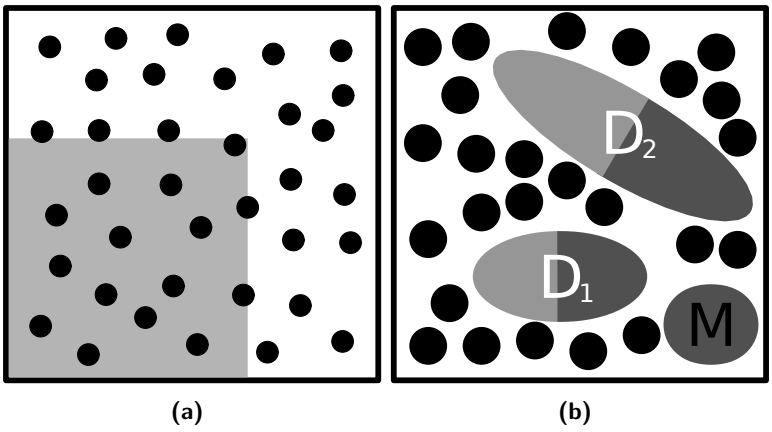

Figure 1.5 (a) An illustration for molecular crowding. The black circles and the gray shaded square occupy approximately 40% of the total area of the box. (b) Dimerization reaction in the presence of crowders (black circles). The dimer D_2 occupies a larger volume than two monomers (M) and hence is energetically less favorable than D_1, since more energy has to be spent on the displacement of crowders.

Volume exclusion due to macromolecular crowding changes reaction rates and equilibria as compared to bulk solution [18]. The underlying mechanism is universal and unspecific and consequently affects most macromolecular reactions. For example, a thermodynamic analysis shows that crowding can substantially enhance or inhibit dimerization depending on the character of the dimer, cf. Figure 1.5 (b): If it is "compact" and occupies less volume than two monomers, a dimerization is favorable, while the opposite is true if it has an extended shape that needs a comparably large volume. On the other hand, crowding hampers the motion of macromolecules and hence decreases the diffusion constant. Hence, one expects that increased crowding lowers the diffusion-controlled association rate. In the reaction-limited regime, however, the energy barrier for necessary conformational changes resemble the bottleneck. As the transition state of a dimer is typically as compact as the product complex, crowding will effectively lower the energy barrier. So in summary the presence of inert crowders decelerates fast (diffusion-limited) and accelerates slow

(reaction-limited) associations.

1.3 Anomalous Diffusion

1.3.1 Phenomenology of Diffusion

In the early 19th century the botanist Robert Brown (1773–1858) discovered that small pollen particles undergo an erratic movement – a phenomenon that afterwards became known as *Brownian motion*. In 1905 Albert Einstein [19] presented a theoretical description of Brownian motion in the framework of statistical mechanics and showed that the random displacements of individual particles leads macroscopically to a spreading of their concentration, that is *Fickian diffusion*. In the picture of Einstein, the erratic movement, e.g. of colloids in water, emerges from perpetual, uncorrelated impacts of solvent molecules onto the dissolved particle. Thus, the regime of Brownian motion is indeed the *mesoscopic* scale: On one hand, the solutes are small enough to experience substantial thermal fluctuations, but on the other hand they are so large that the impacts of the solvent particles may be treated in a statistical manner. The typical sizes of particles that undergo Brownian motion thus stretches from the nano- to the micrometer scale.

One way to classify diffusion processes is the scaling of the *mean square displacement* (MSD) $\langle \delta^2 \rangle$ with time t, i.e. the time course of the average area explored. In the context of this work the focus lies on power-law scalings:

$$\langle \delta^2 \rangle \sim t^\alpha, \quad \text{with} \quad \alpha > 0\,. \tag{1.6}$$

The special case of a linear scaling ($\alpha = 1$) corresponds to Brownian motion. It is closely related to an unbiased random walk (see below) and thus constitutes a canonical scenario. Here, it will also be addressed as *regular* or *normal* diffusion in the context of diffusive transport phenomena. *Anomalous diffusion*, in turn, is defined as any non-linear scaling of the MSD with time [20], i.e. $\alpha \neq 1$. The *diffusion anomaly* α may take any positive real value. Notable regimes are

1. $\alpha < 1$: subdiffusion,
2. $\alpha = 1$: normal diffusion (Brownian motion),
3. $\alpha > 1$: superdiffusion,
4. $\alpha = 2$: ballistic motion.

This work focuses on subdiffusion ($\alpha < 1$) since this mode of motion is frequently observed in complex fluids. In the following we summarize experimental methods and evidence for anomalous subdiffusion and models for its physical mechanism.

1.3.2 Experimental Techniques

Fluorescence Correlation Spectroscopy (FCS)

Fluorescence correlation spectroscopy (FCS) is a well established technique to study anomalous diffusion *in vitro* and *in vivo* [21, 22, 23]. Figure 1.6 depicts the essential setup: As a fluorescent microscopy technique, FCS relies on excitable dyes that emit fluorescence light when they relax back to their ground state. By virtue of confocal laser optics, the excitation beam is permanently focused onto a small spot with radius r_0 (typically $\approx 320\,\mathrm{nm}$ [24]), the *confocal volume*, within the specimen. When a fluorescent tracer enters the confocal volume it emits fluorescence light that is recorded by an appropriate detector, e.g. an avalanche photodiode. The time series of the fluorescence intensity $F(t)$ contains information about the number of tracers within the confocal volume and its autocorrelation $C(\tau) = (F(t)-\langle F\rangle)(F(t+\tau)-\langle F\rangle)\rangle/\langle F\rangle^2$ allows to extract properties of the diffusion process, cf. Figure 1.7. This is achieved by fitting a model autocorrelation function to the data. In particular, for anomalous subdiffusion in three dimensions the corresponding model reads [25]

$$C(\tau) = \frac{1/N}{1 + (\tau/\tau_D)^\alpha \sqrt{1 + q(\tau/\tau_D)^\alpha}}\,, \tag{1.7}$$

where τ_D and α are fitting parameters; τ_D corresponds to the mean residence time that a tracer spends within the confocal volume; q accounts for the unavoidable elongation of the confocal volume along the optical axis, with a typical value of $q \approx 1/36$ [24]. N denotes the average number of tracers that contribute to the signal and usually falls into the range $1 < N < 10$. In case of normal diffusion, the diffusion coefficient can be estimated from the mean residence time through $\tau_D = r_0^2/(4D)$.

By concept, FCS measures the average diffusion behavior of an ensemble of tracers and individual features of the trajectories are lost. This renders FCS a rather robust method, but it cannot be used alone to determine the underlying dynamics of tracers. At the moment it seems, that only higher moments of the observables can give a conclusive answer in this respect.

Single Particle Tracking (SPT)

Single particle tracking (SPT) denotes a category of microscopy experiments that study the motion of individual nano-particles [26]. The markers are usually fluorescent dyes, colloidal gold, or latex beads. In general, the two- or even three dimensional coordinate $\mathbf{x}$ of the particle under observation is recorded at a frame rate φ (e.g. the standard video rate: $1/25\,\mathrm{s}^{-1}$; modern devices reach up to $1/500\,\mathrm{s}^{-1}$). Since the tracer is smaller than the optical wavelength, the center of its Airy disk defines its position. Consequently, the uncertainty of the particle position can be considerably smaller than the optical wavelength, i.e. several nanometers. The accuracy gets worse for moving tracers and faster frame rates. The error on $\mathbf{x}$ can lead to severe misinterpretations like apparent subdiffusion where diffusion should be normal [27] and wrong conclusions about the process behind subdiffusion, see Section 3.1.

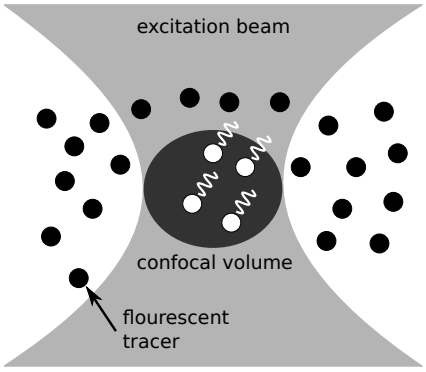

Figure 1.6 Sketch of a FCS setup. Fluorescent tracers, e.g. a labeled protein species, diffuse in the specimen while the excitation beam resides at a fixed position. Whenever a tracer enters the confocal volume (dark shaded area) it contributes to the measured fluorescence signal, cf. Figure 1.7 (a).

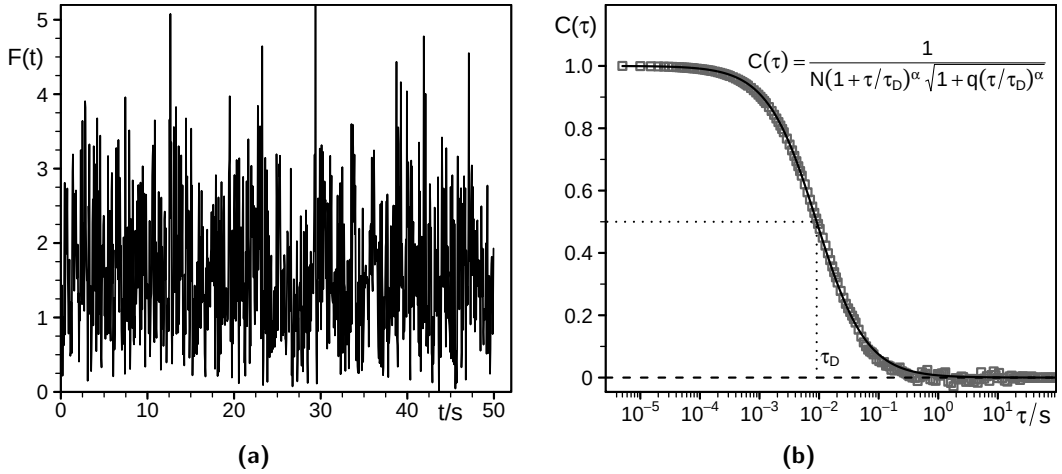

Figure 1.7 Analysis of a simulated FCS measurement. The fluorescence signal (a) is autocorrelated (b) and subsequently fitted with an adequate model. For subdiffusion, e.g., the model $C(\tau)$ reads as Equation (1.7)

A crucial point in every SPT setup is to detect the photons emitted from or scattered by individually moving particles. Here, wide-field microscopy resembles a well established approach where a large spatial area is monitored, e.g. by a CCD camera [28]. The unavoidable noise, e.g. due to dark states of the label, render it a demanding task to reconstruct the trajectory of a single particle from the sequence of frames [29].

A detection method that combines the advantages of confocal imaging with the ability to follow the tracers' motion has been proposed by Enderlein [30], see Figure 1.8: A laser beam (Gaussian shape, waist w) that is sharply focused onto a plane describes a circular trajectory with radius R and period T. During each rotation the number of detected photons is recorded with high temporal resolution. After every full period, the center of the circular trajectory is moved into the direction where the majority of the photons has been collected. As this corresponds to the direction where the tracer came closer to the circulating beam, the center of the circle consequently follows its motion. This technique allows to record very long trajectories; even for a moderate signal-to-noise ratio the average tracking time is several orders of magnitude larger than the escape time from a static focus. Furthermore, extensions to this approach allow for highly resolved trajectories in three dimensions [31].

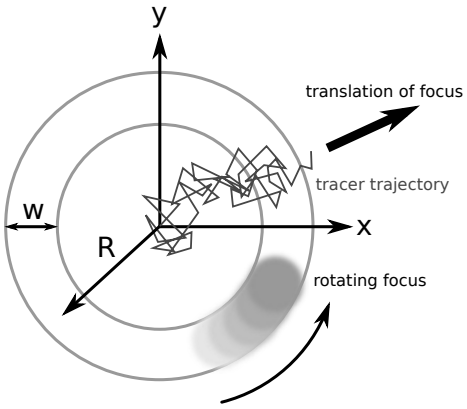

Figure 1.8 The principles of the rotating focus technique for single particle tracking (SPT). The Gaussian excitation beam of width w is tightly focused on the plane of diffusion and describes a circular trajectory with radius R around the tracer. After a full period the center of the circle is moved into the direction where most photons have been detected, because there the tracer closely approached the rotating focus.

One straightforward analysis on the time series of recorded coordinates is the calculation of the time- and ensemble-averaged MSD [32], cf. Section 1.3.4. From this the diffusion anomaly α and the diffusion coefficient D can be obtained. Furthermore, one can study geometrical aspects like the trajectory shape [33], see Section 3.2. The empirical probability distribution function of these quantities yield precious information about tracer diffusion, e.g. the coexistence of fast and slow populations [34]. But, as mentioned above, SPT data can readily provoke wrong interpretations due to measurement uncertainties [27, 32]. Moreover, the intrinsic stochasticity of the process under investigation may be misleading [33, 34]. Hence, the robust analysis of SPT data requires care, experience, and often a consistency check with computer simulations.

In all, SPT outperforms FCS in terms of detail since, in principle, the whole distributions of quantities like the diffusion coefficient are accessible. It thus provides

a constantly advancing technique for the analysis of diffusion processes in complex environments like the cytoplasm, see Section 3.2. The other side of the coin is that drawing reliable conclusions from the data requires much effort in terms of data recording, the generation of good statistics, and a subsequent careful analysis.

1.3.3 Evidence for crowding-induced Subdiffusion

Up to now, a plethora of experiments has detected subdiffusion of tracer particles in crowded fluids. Using FCS, for example, it has been explored in the cytoplasm and nucleoplasm of living cells [25, 35]. This applies for dextran tracers of various sizes as well as for nano-gold particles with a radius of approximately 5 nm. Furthermore, to check for the influence of complex structures like the cytoskeleton or membrane enclosed organelles these have been disrupted by drugs. It turned out that the measured α is almost independent of these treatments, implying that subdiffusion originates primarily from the crowded nature of the cytoplasm without the need for any ordered structures [25]. Guigas *et al.* [35] confirmed this interpretation by showing that osmotic stress leads to alleviated subdiffusion of nano-gold in the cytoplasm.

Along this line, *Xenopus laevis* egg extract served as another example for a biological, crowded solution [35]. Naturally, there are neither membranous nor skeletal structures and again subdiffusion occurred with very pronounced anomalies down to $\alpha = 0.52$. Other *in vivo* studies relied on tracers that are relatively huge and allow the tracking of individual particles. In the cytoplasm of *E. coli* bacteria Golding and Cox [36] tracked the diffusion of individual fluorescently labeled mRNA molecules with a physical size of order ~ 100 nm. They observed subdiffusion with $\alpha = 0.70$. A similar value was discovered for lipid granules (300 nm in diameter) in living yeast cells [37]: For short times ($10^{-4} \ldots 10^{-3}$ s) optical tweezer measurements give $\alpha = 0.73$ and for longer times multiple particle tracking reveals $\alpha = 0.68$ ($0.1 \ldots 1$ s) and $\alpha = 0.70$ ($1 \ldots 10$ s), respectively. Again, only slightly changed values were obtained when the cytoskeletal filaments of the cell were disrupted by drug treatment.

The nucleoplasm of eukaryotic cells is of special interest in the context of diffusion experiments since it contains the heredity information in form of DNA. Intriguingly, the two metres of human DNA are thronged into the cell nucleus of just some micrometers in size. This demands a sophisticated way of folding that still allows active genes to be reliably processed by the cell machinery. Wachsmuth *et al.* [38] studied the diffusion of EGFP through the nucleoplasm and found subdiffusion consistent with $\alpha \approx 0.87$. Bancaud *et al.* [39] took a closer look and detected subdiffusion with $\alpha = 0.73 \ldots 0.79$ depending on the method (FCS/SPT) and the locus. Regions with low gene activity ("heterochromatin") are more dense and lead to slightly enhanced subdiffusion as compared to highly active regions ("euchromatin"). Guigas *et al.* [35] report a pronounced, average subdiffusion with $\alpha = 0.56$ of nano-gold through the nucleoplasm. As in the cytoplasm, osmotic stress weakens the effect.

Artificial, complex fluids usually consist of only a single or few crowding species and hence promise a better control of anomalous diffusion than biological fluids that contain thousands of macromolecules. Various combinations of tracers and crowders have been discussed: Banks and Fradin [40], for example, studied dextran, BSA and streptavidin solutions and tracers of various sizes, namely streptavidin (52.8 kDa), FITC-dextran (282.0 kDa), fluorescin (376.3 kDa), and various dextrans. They find the most pronounced subdiffusion ($\alpha = 0.76$) for streptavidin in a solution of 276 kDa-dextran at a concentration of 200 g/l. In contrast, diffusion appears less anomalous when the crowders are notably smaller than the tracers. Interestingly, the diffusion of large tracers – BSA, fluorescin and FITC-dextran – in 401 kDa-dextran solution is still normal even at high crowder concentrations. In a recent FCS study, Szymanski and Weiss [24] report $\alpha = 0.81$ for labeled apoferritin in a solution of 500 kDa-dextran at 20% per weight.

Another experimental perspective on subdiffusion evolved from the pioneering work of Mason and Weitz [41]: In the field of *microrheology*, the thermal motion of tracer particles is exploited to obtain the mechanical properties of the medium. More precisely, from the measured MSD the storage and loss moduli of the bulk fluid are computed. Normal diffusion implies uncorrelated increments and corresponds to a purely viscous fluid. Subdiffusion, in contrast, is linked to a non-vanishing elastic component that imposes an anti-correlation of the tracer increments and hence *viscoelasticity*.

A remarkable study in this context has recently been published by Sprakel *et al.* [42, 43]. They used different tracers, namely Silica (radius 70 nm and latex particles (radius 110 nm) in complex fluids containing two classes of transient polymer networks. The first system consisted of entangled homopolymers while the second additionally had associative agents that lead to a cross-linking between the polymer chains. Two possible particle-network interactions could be identified, *sticking* and *non-sticking* conditions. In the sticking scenario, the polymers in the solution adsorbed to the tracer that consequently became (transiently) a part of the network, while in the non-sticking setting the polymers avoided contact with the colloids. The measured tracer MSDs showed three regimes as sketched in Figure 1.9:

1. At short times ($t < 10^{-4}$ s), the behavior depended on the tracer-network interactions. For sticking conditions, the tracer diffused like a monomer in a Rouse polymer, i.e. $\alpha = 0.5$, while for non-sticking conditions it diffused normally.

2. For intermediate times (10^{-4} s $< t < 1$ s), the elastic component dominated, giving rise to a plateau in the MSD (*elastic caging*).

3. For long times ($t > 1$ s), tracer diffusion was normal. Due to the transient nature of the polymer networks, this regime was dominated by the macroscopic viscosity of the fluid.

In a related study Pan *et al.* [44] followed the diffusion of BSA-coated nanoparticles with diameters ranging between 100 and 1000 nm. As crowding agent they

used the small protein lysozyme (14.4 kDa). Even for small crowder concentrations (20 g/l) they observe distinctly anomalous diffusion with $\alpha = 0.6$ on the millisecond time scale. Higher concentrations lead to a further drop down to 0.45 at 286 g/l. For longer times the anomalous diffusion crosses over into normal diffusion according to the situation described above. Hence, the lysozyme solution exhibits viscoelasticity due to the formation of a transient network. These two discussed studies nicely illustrate three important aspects of subdiffusion in complex media: First, it is a transient phenomenon, i.e. the measured anomaly depends on time. Second, the interactions between solutes and fluid and within the fluid influence the outcome. And third, subdiffusion is intimately linked to viscoelasticity.

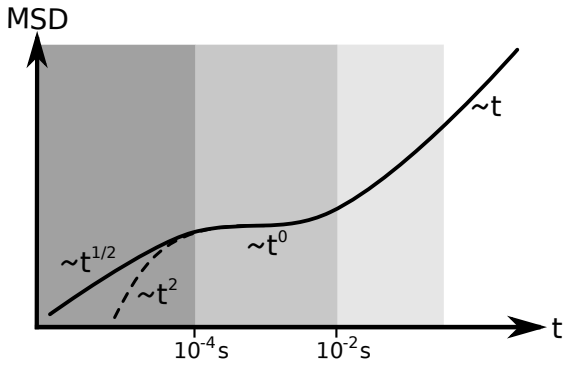

Figure 1.9 Sketch of the MSD measured for a colloid in a viscoelastic fluid. The given cross-over times were chosen according to [43]. The short time behavior depends on whether the tracer incorporates into the network of the crowding agents (sticking vs. non-sticking conditions, cf. text and [43]). If this is the case, the tracer behaves as part of a Rouse polymer at short times, i.e. $\alpha = 0.5$, while in the opposite case the initial dynamics is ballistic ($\alpha = 2$). At intermediate times a plateau ($\alpha \approx 0$) indicates *elastic caging*. For long times diffusion becomes normal, i.e. purely viscous ($\alpha = 1$).

There are also studies that report on *slowed down*, normal diffusion, i.e. $\alpha = 1$, in crowded fluids. Goins *et al.* [45], for example, found via FCS that eGFP-calmodulin (43 kDa) diffuses normally through dextran-solutions of various concentrations and crowder sizes. In fact, they detect various values $\alpha < 1$ with the minimum $\alpha = 0.87$. They claim that this value is too close to unity to be interpreted as anomalous diffusion. In their review, Dix and Verkman [46] discuss further experiments that apparently contradict the notion of anomalous diffusion in biological fluids.

Membranes like those that enclose the cell and its compartments can be considered as two-dimensional fluids. In analogy to the cytoplasm they contain numerous proteins and hence constitute a complex medium for diffusive tracers where as much as 20% of the total area is occupied [17] Indeed, subdiffusion of proteins has been detected with pronounced diffusion anomalies varying between $\alpha = 0.5$ and $\alpha = 0.8$ [47, 48].

In addition, anomalous subdiffusion also occurs on artificial membranes with and without crowding [28, 49]. Only recently Harland *et al.* [50] claimed that pure phospholipid bilayers exhibit viscoelasticity.

In summary, various *in vivo* and *in vitro* experiments show crowding-induced subdiffusion in the cytoplasm, on membranes and in artificial polymer solutions. Given the vast range of possible tracer-crowder combinations it is a challenging task to rationalize the experimental findings and predict the occurrence and degree of anomalous diffusion. Due to the mesoscopic nature of diffusion phenomena, all kinds of tracer-crowder and crowder-crowder interactions as well as their size ratio determine the observed behavior.

1.3.4 Theoretical Models for Normal and Anomalous Diffusion

Brownian Motion

The *random walk* (RW) is a prototypic discrete random process in time and space with a vast range of applications [51]. A "random walker" moves on a d-dimensional lattice with a constant (small) distance r between neighbouring nodes by randomly jumping to a nearest neighbor site in every instant of time. Assuming a symmetric, unbiased RW, the probability to proceed to a particular neighbor site is $1/(2d)$. Let $\mathbf{S_n}$ be the position of the walker after n steps. Then the displacement in x-direction reads

$$S_n^1 - S_0^1 = \sum_{i=1}^{n} X_i \,, \tag{1.8}$$

where the sequence $\{X_i\}$ contains independently and identically distributed random numbers according to

$$\mathbb{P}(X_i = k\delta) = \begin{cases} \frac{1}{2d} & \text{if } |k| = 1 \,, \\ 1 - \frac{1}{d} & \text{if } k = 0 \,. \end{cases} \tag{1.9}$$

However, Brownian motion takes place in continuous time and space, and particle experience a large number of erratic of impacts during an observation period. In other words the number of steps n is large and the central limit theorem states that the distribution of the displacements becomes approximately normal in this case, $\mathcal{N}(0, \frac{1}{d} n r^2)$. Let τ denote the discretization of time, i.e. jumps take place at times $\tau, 2\tau, 3\tau \ldots$. τ is small in the sense that in any reasonable observation time t numerous jumps occur, namely $n = \lfloor t/\tau \rfloor$. Hence the distribution of the displacements becomes $\mathcal{N}(0, \frac{1}{d} t r^2/\tau)$. Taking the limit τ and $r \to 0$ in such a way that $\sigma^2 \equiv \frac{1}{d} r^2/\tau$ remains constant leads to $\mathcal{N}(0, \sigma^2 t)$. As all spatial directions are mutually independent the displacement vector $\mathbf{S}(t) - \mathbf{S}(0)$ actually follows a multivariate normal distribution.

Mathematically, the continuous limit of the random walk, and thus Brownian motion, is described by the *Wiener process* $W = \{W(t) : t \geq 0\}$ $(W(0) = w)$ with the following characteristics [51]:

1. W is a *Gaussian process*: Each finite-dimensional vector $(W(t_1), W(t_2), \ldots, W(t_n)$ has the multivariate normal distribution $\mathbf{N}(\mu(\mathbf{t}), \mathbf{V}(\mathbf{t}))$ for some time dependent mean vector μ and covariance matrix $\mathbf{V}$.

2. W has *stationary independent increments*: That means

   - the distribution of $W(t) - W(s)$ depends only on the distance $t - s$ and
   - the variables $W(t_j) - W(s_j)$ with $1 \leq j \leq n$ are independent whenever the intervals $(s_j, t_j]$ are disjoint.

3. The differences $W(s+t) - W(s)$ $(s, t > 0)$ are distributed according to a normal distribution with zero mean and variance $\sigma^2 t$, where σ is a positive constant.

4. W has continuous sample paths.

One can prove, that a random process with these features indeed exists, see e.g. [51].

The trajectory of a Wiener process exhibits (statistical) self-affinity and self-similarity and thus resembles a *random fractal* [52]. The Hausdorff and box counting dimension of a trajectory in $\mathbb{R}^d$ $(d \geq 2)$ is $d_W = 2$.

There are conceptual impairments with the Wiener process as a model for Brownian motion: It can be shown that almost all sample paths are nowhere differentiable functions of t. Consequently, the arclength of a sample path is infinite with respect to every finite time interval. On short time scales the Wiener process thus describes unphysical behavior but the agreement with experiments is good for longer periods. There are improved models to overcome the difficulties on short time scales, a prominent example being the Ornstein-Uhlenbeck process [51].

Given the covariance of W the expected value of W^2 is $\langle W(t)^2 \rangle = \sigma^2 t$. This value complies with the MSD of Brownian particles:

$$\langle \delta^2 \rangle \equiv \sigma^2 t = 2dDt\,, \tag{1.10}$$

where D denotes the *diffusion coefficient*. D is a measure for the mobility of the diffusing particles in a given solvent. It thus specifically depends on the particle and solution properties as size, shape, and viscosity. For small particles, like macromolecules or colloids, the Reynolds number is very small[3]. Thus Stokes' law applies that gives the frictional force on a sphere with radius R dragged with constant velocity u through a fluid of viscosity η:

$$F_S = 6\pi\eta R u\ . \tag{1.11}$$

Now, the diffusion coefficient D can be expressed through F_S by the so called *Einstein-Stokes equation* [19]

$$D = \frac{k_\mathrm{B} T}{6\pi\eta R}\ . \tag{1.12}$$

[3] In fluid mechanics, the Reynolds number Re gives a dimensionless measure for the relative importance of viscosity and inertia in fluid flow around an object. It is defined as the ratio $\overline{u}\rho l/\eta$, where $\overline{u}$ denotes the mean flow velocity, ρ the density of the fluid, l a characteristic length scale and η the (dynamic) viscosity of the fluid. A small value of Re corresponds to viscous flow. This limiting case is also known as *Stokes regime*. [53]

An alternative formulation of Brownian motion has been proposed by Paul Langevin in 1908. In an elegant manner it combines Einstein's interpretation with Newton's equation of motion to a stochastic differential equation for the particle position $\mathbf{x}$, known as the *Langevin equation*:

$$m\frac{d^2x}{dt^2} = -m\zeta\frac{dx}{dt} + \xi(t)\,. \tag{1.13}$$

In this formulation the perpetual impacts of solvent molecules onto a Brownian particle of mass m are summarized in a *stochastic force* $\xi(t)$. ζ denotes the friction coefficient, i.e. the dissipation of kinetic energy in the medium. According to the ideas of Einstein, the impacts should contribute no measurable displacement on the average, hence one demands

$$\langle\xi(t)\rangle = 0 \quad \text{and} \quad \langle\xi(t)\xi(t')\rangle = \phi(t-t')\,. \tag{1.14}$$

The motion of the particle is studied for times $\tau > \tau_c$ where τ_c gives the scale on which the correlation function ϕ deviates significantly from zero. The function $\phi(\tau)$ can hence be written in terms of a Dirac δ-function:

$$\phi(\tau) = \sigma\delta(\tau)\,. \tag{1.15}$$

The *friction coefficient* ζ and the variance of the stochastic force σ are linked by a *fluctuation-dissipation theorem* known as the *Einstein relation*

$$\sigma = 2\zeta m k_\mathrm{B} T\,. \tag{1.16}$$

The description of Brownian motion by virtue of the Langevin equation is a starting point for stochastic simulation algorithms as will be described later.

Ergodicity

The MSD of a diffusion process can be defined in two ways, namely

1. as an *ensemble average*

$$\langle\delta^2\rangle_\mathrm{E}(t) \equiv \frac{1}{N}\sum_{i=1}^{N}\left(x_i(t) - x_i(0)\right)^2\,, \tag{1.17}$$

2. or as a *time average*

$$\langle\delta^2\rangle_\mathrm{T}(\tau) \equiv \frac{\int_0^{t-\tau}\left[x_i(t'+\tau) - x_i(t')\right]^2 dt'}{T-\tau}\,, \tag{1.18}$$

where the *lag time* τ takes the role of t.

According to the *quasi-ergodic hypothesis* a system is called *ergodic*, if every trajectory – excluding a set of zero measure – comes arbitrarily close to every point of the phase space in finite time. For *ergodic* systems time and ensemble average are equivalent, i.e.

$$\langle \delta^2 \rangle_{\mathrm{T}} = \langle \delta^2 \rangle_{\mathrm{E}} \,, \tag{1.19}$$

for long times t. Systems with *broken* ergodicity can, for example, arise after symmetry breaking phase-transitions when some regions of the phase space are no longer accessible for the system. Bouchaud [54] introduced the term of *weak ergodicity breaking*. The attribute "weak" refers to the fact that phase space does not *a priori* fragment into isolated subvolumes. In contrast, the dynamics is governed by power law distributed sojourn times with a diverging mean. Anomalous diffusion according to the continuous time random walk is one example for such a system.

Continuous Time Random Walk (CTRW)

A continuous time random walk (CTRW) [20, 55] is an extension of the regular random walk. In contrast to its ancestor, the jump lengths r and the waiting times t may differ for each step and follow some probability density function $\psi(r,t)$. In case of independent jump lengths and waiting times ψ separates: $\psi(r,t) = \lambda(r)w(t)$. Different CTRW realizations can be characterized by the *mean waiting time* (also *characteristic waiting time*) T and the *jump length variance* S^2:

$$T = \int_0^\infty \mathrm{d}t \, w(t)\, t \tag{1.20}$$

$$S^2 = \int_{-\infty}^\infty \mathrm{d}x \, \lambda(x)\, x^2 \,. \tag{1.21}$$

In this respect, one has to consider especially processes with diverging T and S^2. For finite waiting time and jump length variance, the long-time limit is always normal diffusion since the central limit theorem applies. Here, we will focus on scenarios where T diverges and hence subdiffusive motion emerges. In particular, the distribution $w(t)$ shall obey a power-law decay for long times

$$w(t) \sim \left(\frac{\tau}{t}\right)^{1+\alpha} \quad \text{for} \quad 0 < \alpha < 1 \,. \tag{1.22}$$

Consequently, the random walker will encounter extremely long waiting times with non-zero probability. For the limited observation in a simulation this implies that the walker is practically stuck. An ensemble of walkers hence tends towards a frozen state, where the majority of particles is at rest. In mathematical terms, the CTRW has non-stationary increments and shows aging, i.e. the outcome of a measurement depends on the time when the measurement is performed.

The CTRW exhibits weak ergodicity breaking [56]. This means time and ensemble averages of quantities like the squared displacement behave differently: If a set of CTRW-trajectories is analyzed one finds that the time average MSD scales linear with the lag time, i.e. $\langle \delta^2 \rangle_{\mathrm{T}}(\tau) \sim \tau$, while the ensemble average shows a subdiffusive scaling law $\langle \delta^2 \rangle_{\mathrm{E}} \sim t^{\alpha}$. The diffusion coefficient D_α obtained from the time-averaged MSDs is a random variable among the ensemble of trajectories [57, 58]. In general, time-averaged quantities show a broad distribution around the ensemble average for systems under weak ergodicity breaking [59]. This feature of the CTRW separates it from other models – especially fractional Brownian motion and obstructed diffusion – and hence has been discussed as a means to determine the mechanism of experimentally observed subdiffusion [57, 58].

Fractional Brownian Motion (FBM)

Fractional Brownian motion (FBM) is a generalization of Brownian motion in the sense that the increments are still stationary but no longer independent. It was initially discussed by Mandelbrot and van Ness [60], but we will first give a definition that emphasizes the close relationship to BM. A real-valued process $B = \{B(t) : t \geq 0\}$ that starts from $B(0) = b$ is called *fractional Brownian motion*, if the following characteristics are met [52]:

1. B is a *Gaussian process.*
2. B has *stationary increments*: That means
   - the distribution of $B(t) - B(s)$ depends only on the distance $t - s$, but
   - the variables $B(t_j) - B(s_j)$ with $1 \leq j \leq n$ are in general *not independent* even for disjoint intervals $(s_j, t_j]$.
3. The differences $B(s+t) - B(s)$ $(s, t > 0)$ are distributed according to a normal distribution with zero mean and variance $\sigma^2 t^{2H}$, where σ is a positive constant, and $0 < H < 1$ the *Hurst parameter.*
4. $B(t)$ has continuous sample paths.

The newly introduced Hurst parameter H describes the self-similarity of the process. In analogy to BM, the incremental process of FBM

$$dB(t, s) \equiv B(t + s) - B(t) \tag{1.23}$$

is called *fractional Gaussian noise* (FGN).

Several interesting properties can be derived from the definition of FBM and FGN:

- The special case $H = 1/2$ is equivalent to BM.

- The probability function of FGN reads

$$P(B(t+s)-B(t)\leq x)=\frac{1}{\sqrt{2\pi\sigma^2 s^{2H}}}\int\limits_{-\infty}^{x}\mathrm{e}^{\frac{-u^2}{2\sigma^2 s^{2H}}}du\ . \tag{1.24}$$

- Using its path integral representation, Sebastian [61] calculated the propagator of FBM:

$$G(B_t,t|B_0,0)=\left(\frac{2H\Gamma^2(H+1/2)}{2t^{2H}\pi}\right)^{1/2}\exp\left(-\frac{(B_t-B_0)^2\Gamma^2(H+1/2)2H}{2t^{2H}}\right). \tag{1.25}$$

- The increments are statistically invariant under an affine transformation.
- The MSD gives $\langle B(t)^2\rangle=\sigma^2t^{2H}$, so the diffusion anomaly relates to H as $\alpha=2H$.
- The autocorrelation function for FGN yields

$$C(\tau)\equiv\langle dB(t+\tau,s)dB(t,s)\rangle=\frac{\sigma^2}{2}\left((\tau+s)^{2H}-2\tau^{2H}-(\tau-s)^{2H}\right)\ , \tag{1.26}$$

  which becomes

$$C(\tau)\approx H(2H-1)\tau^{2H-2}\text{ for large lags, i.e. }\tau\gg s\ . \tag{1.27}$$

- Based on $C(\tau)$ one can define three regimes [60, 62, 63]
  1. $0<H<\frac{1}{2}$: $C(\tau)<0$, i.e. increments are *anti-correlated*. This regime corresponds to an *anti-persistent* process and subdiffusion. $C(\tau)$ decays to zero for $\tau\to\infty$ with a power law $\sim\tau^{-1\ldots-2}$, so $C(\tau)$ is summable and FGN constitutes a *short memory process*.
  2. $H=\frac{1}{2}$: $C(\tau)=0$, i.e. increments are *uncorrelated*, as expected for memory-free Gaussian noise.
  3. $\frac{1}{2}<H<1$: $C(\tau)>0$, i.e. increments are *correlated*. Now FGN is *persistent* and $C(\tau)\to0$ like $\sim\tau^{0\ldots-1}$. In this case, $C(\tau)$ is not summable and hence indicates a *long memory process*.

In their systematic discussion, Mandelbrot and van Ness defined FBM in a different way [60]. As before, the Hurst parameter is bound to $0<H<1$ and b is an arbitrary real number. The following random function $B(t)$ resembles *(reduced) fractional Brownian motion* for $t>0$:

$$\begin{aligned}B(0)&=b\,,\\ B(t)-B(0)&=\frac{1}{\Gamma\left(H+\frac{1}{2}\right)}\left(\int\limits_0^t(t-\tau)^{H-1/2}\,\mathrm{d}W(\tau)\right.\\ &\quad\left.+\int\limits_{-\infty}^{0}\left[(t-\tau)^{H-1/2}-(-\tau)^{H-1/2}\right]\mathrm{d}W(\tau)\right)\ .\end{aligned} \tag{1.28}$$

The integrator dW corresponds to (regular) Brownian motion. Thus $B(t)$ resembles a fractional derivative or integral of BM. The special case of BM is recovered for $H = \frac{1}{2}$, i.e. when all t-dependent terms under the integrals vanish. This notation makes clear that FBM differs from BM by a memory kernel that creates a dependence between the next step and all previous steps of the process.

Although CTRW and FBM share some characteristics and both give rise to anomalous diffusion, they are quite different. In contrast to a CTRW, FBM is ergodic for $H < 3/4$, i.e. time- and ensemble-averaged MSD are equivalent in the subdiffusive regime [64]: The time average MSD shows sublinear scaling with lag time τ ($\langle\delta^2\rangle_\mathrm{T} \sim \tau^\alpha$), while a CTRW appears like normal diffusion with respect to τ. The anti-persistence of FGN below $H = \frac{1}{2}$ implies that a step in positive direction will be followed by one in negative direction with high probability, and vice versa. Nevertheless, the average residence time that the process spends within a finite spatial domain does not diverge like for a CTRW [65].

The Langevin equation has been presented before as a convenient formulation of Brownian motion. In close analogy a *fractional Langevin equation* (FLE) can be derived for FBM [66, 67]:

$$m\frac{d^2x}{dt^2} = -\overline{\gamma}\int_0^t \frac{1}{(t-t')^\alpha}\frac{dx}{dt'}dt' + \xi(t)\,, \tag{1.29}$$

where $\overline{\gamma}$ denotes a generalized friction constant, $\gamma = 1/m\overline{\gamma}\Gamma(1-\alpha)$. Now, $\xi(t)$ resembles FGN with zero mean, and the fluctuation-dissipation relation

$$\langle\xi(t)\xi(t')\rangle = k_\mathrm{B}T\overline{\gamma}|t-t'|^{-\alpha} \tag{1.30}$$

In contrast to the conventional Langevin equation the friction term in Equation (1.29) contains an integral over a memory kernel with a power-law decay. The memory kernel for Brownian motion simply is the δ-function.

Obstructed Diffusion (OD)

Another way of generalizing the random walk is to confine its motion to a topological subset of the embedding space [68, 69]. A concrete realization for such a *disordered environment* emerges when a set of lattice nodes is inaccessible to the random walk. The deletion procedure can, for example, follow a percolation approach, i.e. randomly place a given number of obstacles among the lattice sites, or rely on an iterated formula to create a deterministic fractal support like a Sierpinski gasket. Now, also the support of the walk has a fractal dimension d_f that describes how the fractal is embedded into the d-dimensional "outer" space. In particular, d_f relates the "mass" M of the fractal contained within a hyper-sphere of radius R:

$$M \sim R^{d_f}\ . \tag{1.31}$$

As stated above, the random walk itself exhibits statistically self-similar behavior and has a fractal dimension $d_W = 2$. So, for a random walk on a fractal support the

interplay of the fractal dimensions d_W and d_f will somehow determine the transport properties. In fact, d_W changes and hence diffusion becomes anomalous. The MSD of the random walk then scales as [68]

$$\langle \delta^2 \rangle \sim t^{2/d_W} \quad \Rightarrow \alpha = \frac{2}{d_W} \ . \tag{1.32}$$

The *spectral dimension* d_S describes how the number of distinct sites visited by the random walk grows with time:

$$S(t) \sim t^{d_S/2} \quad \text{with} \quad d_S = \frac{2d_f}{d_W} \tag{1.33}$$

The term *obstructed diffusion* is usually assigned to a random environment formed by stochastically distributed obstacles in a system. Such a setting corresponds to the percolation problem [70]: At a critical obstacle concentration f_p (*percolation threshold*) there is one macroscopic, contiguous cluster of empty sites, the *percolating cluster*. Above this threshold the accessible space consists of numerous, isolated ("microscopic") islands. The resulting set of vacant sites constitutes a random fractal with fractal dimension d_f depending on the obstacle concentration f [68, 71]:

1. Below f_p there is an infinite cluster of vacant sites, but also an upper scale $\xi(f)$ for its statistical self-similarity (i.e. a finite correlation length). So above $\xi(f)$ the mass of the cluster does not scale like a fractal (R^{d_f}), but rather like a homogeneous object (R^d). In this case, a random walk exhibits normal behavior, i.e. $d_W = 2$ for $R > \xi(f)$.

2. At f_p (on the 2D square lattice: $f_p = 1 - 0.59274 = 0.40726$ [72]) there is a single infinte self-similar cluster of vacant sites that spans the whole system. The percolation threshold marks a phase transition, so the correlation length diverges and there is no upper scale for self-similarity. In this scenario, a random walk encounters dead-ends on all scales and thus anomalous diffusion emerges with $d_W > 2$. In particular, for two embedding dimensions: $d_f = 91/48$ and $d_W \approx 2.87$ (i.e. $\alpha \approx 0.697$ [71]).

3. Above f_p the vacant sizes are arranged in isolated clusters with a typical size of $\xi(f)$. Each cluster resembles a finite fractal object. As $t \to \infty$, an ensemble of random walks will feel the island boundaries, i.e. the MSD levels at $\langle \delta^2 \rangle \sim \xi(f)^2$.

1.3.5 Interpretation of Crowding-induced Subdiffusion

Viscoelasticity

For subdiffusion in experiments we discussed the close relationship to viscoelasticity. Indeed, in the framework of the generalized Langevin equation (GLE), viscoelastic

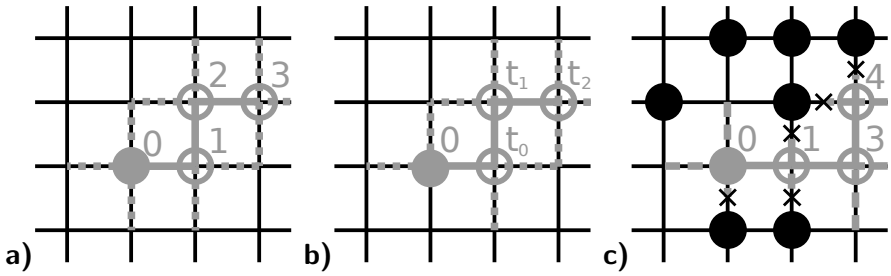

Figure 1.10 Principle of the random walk and derived models for subdiffusion. a) In every instant the next position of the RW is chosen among all nearest neighbor sites with equal probability. For the example shown, the walker starts at the filled circle for $t = 0$ and subsequently follows the path indicated by the solid line. b) A CTRW extends the RW by introducing a waiting time that is drawn randomly from a heavy-tailed distribution at every position. For example, the walker leaves its initial position only after the waiting time t_0 has passed. c) OD resembles another variant of the RW: A subset of lattice sites is occupied by immobile obstacles (black circles). The random walker may not visit these nodes and hence its motion is obstructed.

effects can be accounted for via a generic memory kernel [73]:

$$m\frac{d^2x}{dt^2} = -\overline{\gamma}\int_0^t \eta(t-t')\frac{dx}{dt'}dt' + \xi(t)\,. \tag{1.34}$$

$\eta(t-t')$ gives rise to temporally correlated motion and together with the random force $\xi(t)$ obeys a fluctuation-dissipation relation in Fourier space

$$\langle \xi(\omega)\xi(\omega')\rangle = \frac{k_\mathrm{B}T}{\pi} m\eta(\omega)\delta(\omega+\omega')\,, \tag{1.35}$$

where $\xi(\omega)$ and $\eta(\omega)$ denote the Fourier transforms of $\xi(t)$ and $\eta(t)$ respectively. As described above, for FBM a fractional Langevin equation is given by the choice $\eta(t-t') = (t-t')^{-\alpha}$. This corresponds to the *Gemant model* of viscoelasticity [65, 74]. In this setting, persistent subdiffusion occurs and the particle is effectively coupled to a bath of oscillators with a frequency spectrum $1/f^{1-\alpha}$ ("fracton thermal bath"). For an experimental situation, the frequency spectrum is truncated and subdiffusion occurs on a limited time scale.

So, FBM arises as a special case of diffusion according to a GLE. Because viscoelasticity is a macroscopic material property, this description resembles a kind of "mean-field" theory. The above mentioned coupling of the particle to a fracton thermal bath can be interpreted as an effective picture of viscoelastic forces in a real complex medium derived from first principles [65]. However, the question arises how this effective behavior can ultimately emerge from particle-particle interactions, i.e. from a "bottom-up" design of a complex fluid.

Coarse-grained molecular dynamics simulations are a promising method to assess this issue: Frequently encountered manifestations of a complex fluid are *gels*. They consist of a wide network of interconnected polymer chains immersed in a solvent. Typically, the *gelation transition* takes place at low concentration of polymers, hence the gel consists largely of solvent. In *physical gels* the interconnections are weak and transient, like van der Waals or ionic bonds. As a result, the structure of physical gels is highly dynamic. On the other side *chemical gels* base on more stable chemical interactions, hence these structures are static. Hurtado *et al.* [75] proposed a model for reversible gelation and studied the diffusion within the transient structure. Hard spherical particles carry a certain number of valences that may form elastic, transient links to other particles in their vicinity. Consequently, a dynamic gel evolved showing viscoelasticity. On intermediate scales elasticity dominates which also shows up as subdiffusion in the course of the MSD. The reversibility leads to normal diffusion in the end. That is, the shape of the MSD curve essentially resembles that of a tracer in a viscoelastic medium, cf. Figure 1.9. In a conceptually different approach Stauffer *et al.* [76] found transient anomalous diffusion of tracers in the presence of slowly moving barriers. In this case, the observed phenomena comprise sub- and superdiffusion in crowded environments.

Identifying the Mechanism behind crowding-induced Subdiffusion

Three models for anomalous have been presented above, namely CTRW, OD, and FBM. Although all of them give rise to some $\alpha < 1$ they exhibit quite different features in other aspects. For example, weak ergodicity breaking implies that time and ensemble average are not equal for the CTRW – in contrast to FBM and OD. It is hence a central question, which model is the best to describe anomalous diffusion in a particular situation. In turn, an adequate model can then be used, to simulate trajectories in the computer and to study the impact on diffusion-dependent processes like chemical reactions.

In recent years, much effort has been dedicated to the determination of the mechanism behind experimentally observed subdiffusion, especially in the biological context. Subdiffusion in the cell nucleus is typically attributed to a fractal environment formed by the chromatin fiber, hence OD is the preferred model in this context [38, 39].

The presence of static obstacles may also play a role on membranes [71], but a resident anomaly has been reported, even if all obstacles are mobile or removed from the membrane [28, 48, 49]. This indicates an additional component that may originate in viscoelastic features of the membrane [50]. Malchus and Weiss [48] showed that interactions with the cell's quality control mechanism led to a stronger subdiffusion of a dysfunctional protein as compared to its active form. Hence, cellular processes may exploit the compactness of subdiffusive trajectories.

For the cytoplasm, a conclusive answer cannot be given, yet. Earlier studies have interpreted experimental data in favor of a CTRW [57, 58], but just recently this hypothesis has been rejected by Magdziarz *et al.* [77] for the data of Golding and

Cox [36] using the p variation method, see also Section 3.1. Tejedor *et al.* [78] found that the motion of lipid granules in living yeast cells is compatible with FBM. But a subsequent study by Jeon *et al.* [79] on the same system actually revealed that this applies for longer times only. Indeed, short time diffusion showed signatures of weak ergodicity breaking and is better described by a CTRW with a finite cutoff in the waiting-time distribution.

Szymanski and Weiss [24] excluded the CTRW from being responsible for subdiffuion in artificial dextran solutions by analyzing the distribution of measured anomalies. First-passage observables have been proposed as another criterion to discriminate between the OD and CTRW scenarios [80]. On the other hand, the distinction whether experimental trajectories are better described by OD or FBM is difficult. In summary, elucidating the mechanism behind crowding-induced subdiffusion requires a sophisticated analysis that combines various approaches [81].

Along this line, we propose a simple method to distinguish FBM, CTRW, and OD in one step. It relies on the different shape of subdiffusive trajectories, as simulations show that FBM trajectories are more spherical in shape than OD trajectories. We applied this method to SPT data of tracers in dextran solutions and found evidence for FBM as the underlying mechanism. This analysis combined with high quality SPT data may prove as a powerful means to distinguish between the three models for subdiffusion in complex fluids.

1.4 Diffusion-controlled Kinetics

Any second or higher order chemical reaction ultimately relies on the encounter of the participating agents. Actually, the rate (velocity) of a reaction is a combination of two factors: Firstly, the *encounter rate* determined by the reactant diffusion process and, secondly, the *reaction rate* that depends on the activation energy necessary to form the product. Consequently, there are two types of reactions, namely diffusion-limited and reaction-limited where either of the two processes dominates the overall reaction rate.

In the context of *classical kinetics*, diffusion is a fast process providing a perfect mixing of reactants at any time. Consequently, reactions can be modeled via a system of ordinary differential equations (ODE) relying on the concentrations of reactants. Hence, transport phenomena and discreteness of reactants are neglected. Within the mean-field description in terms of concentrations, spatial aspects can be implemented by using partial differential equations (PDEs). This approach still relies on locally well-stirred conditions: Any volume element has to contain a sufficient number of particles so that the description in terms of concentrations is valid.

1.4.1 Classical Kinetics – Smoluchowski Theory

The impact of diffusion on chemical reaction rates was first discussed by Marian Smoluchowski in 1917 in the context of colloid coagulation [82] (see also, for example, [83, 84, 85]). His rationals provide the interpretation of fast, i.e. diffusion-limited,

reactions in the *classical* sense. For a basic bulk reaction like A + B $\xrightarrow{k}$ with a *rate coefficient* k products the principal ideas are as follows: The approach focuses on the concentration of B, $\rho_B(r;t)$, in a radial distance r around a central A when B is present in large excess. Furthermore the simple diffusion equation, i.e. Fick's law (cf. above), is assumed to describe the mutual diffusion of A and B. Hence the average stationary spatial distribution of B is obtained by solving the diffusion equation with a sink boundary condition at A and assuming a bulk concentration $\overline{\rho}_B$ far remote from A, formally

$$\frac{\partial \rho_B}{\partial t} = D_{\mathrm{AB}} \nabla^2 \rho_B \,, \tag{1.36}$$

with the boundary conditions $\rho_B(R,t) = 0$ and $\rho_B(\infty,t) = \overline{\rho}_B$ and the mutual diffusion coefficient $D_{\mathrm{AB}} = D_{\mathrm{A}} + D_{\mathrm{B}}$. R denotes the reaction radius that resembles the radial distance of closest approach before A and B react. In *steady state*, when A is constantly added to the system to keep its concentration fixed, the solution reads

$$\rho_B^{ss}(r) = \overline{\rho}_B \left(1 - \frac{R}{r}\right) . \tag{1.37}$$

The diffusion flux at R is proportional to the reaction rate, hence

$$4\pi R^2 D_{\mathrm{AB}} \left(\frac{d\rho_B^{ss}}{dr}\right)_R = k\overline{\rho}_B \,, \tag{1.38}$$

and

$$k = 4\pi D_{\mathrm{AB}} R \,. \tag{1.39}$$

Because the diffusion coefficient D_{AB} does not depend on time the same is true for the observed rate coefficient k.

The conceptually simple theory of Smoluchowski agrees qualitatively with classical reaction kinetics, where the rate coefficient k is a constant. On the other hand, this approach suffers from severe limitations. For example, reactions in two dimensions, e.g. on biological membranes, cannot be described. In this case, it is impossible to satisfy the boundary conditions as the solution to Laplace's equation exhibits a logarithmic divergence. Furthermore, the assumptions of large excess of B and steady state with respect to A imply a permanently well-stirred system, where every A is always surrounded by numerous Bs. So, in situations where stirring is imperfect or for reactions in less than three dimensions deviations from Smoluchowski's theory are anticipated.

1.4.2 Anomalous Kinetics

In a more general description of diffusion-limited kinetics, the Smoluchowski theory turns out to be exact in the limit of immobile A ($D_{\mathrm{A}} \to 0$) and vanishing interaction among the B particles. Hence, it describes many-particle diffusion dynamics correctly only under particular conditions [85]. Numerous improvements of the classical theory have been developed that apply to more general situations (e.g. [84, 85]). Any deviations from classical behavior are denoted as *anomalous kinetics*. Here, we use this term to refer to a non-constant rate coefficient, $k(t)$.

Generalized Transport Process

P. G. de Gennes [86] theoretically analyzed diffusion-limited reactions with non-classical reactant transport, i.e. anomalous diffusion. In other words, the assumption that the concentration of B follows Equation (1.36) is abandoned. For the discussion above, we analyzed the concentration ρ_B around some central A particle. Now we will use the *pair distribution function* $\psi(r_A, r_B)$ that measures the probability to find A and B at the positions r_A and r_B, respectively. This means, all A particles are considered at the same time. The formulas derived above change correspondingly if written with ψ instead of ρ_B. The particles shall react with a constant rate Q when they approach closer than the reactive distance R (in the discussion of Smoluchowski's theory $Q = \infty$, cf. above), i.e.

$$\left.\frac{\partial \psi}{\partial t}\right|_{\text{reaction}} = -Q\psi \quad \text{if} \quad |r_A - r_B| < R\,. \tag{1.40}$$

For a large reaction volume a self-consistency equation for $\psi(r, r; t) \equiv \psi(t)$ is obtained

$$\psi(t) = \rho_A\,\rho_B - Q\frac{4\pi}{3}R^d \int_0^t dt'\psi(t')S(t-t')\,, \tag{1.41}$$

where d gives the dimension of the embedding space and $S(t)$ resembles a *memory function*

$$S(t) = \int dr\Gamma_t(r_0, r_0|r, r)\,. \tag{1.42}$$

$S(t)$ contains the two-particle propagator $\Gamma_t(r_0, r_0|r, r)$. The probability to find A and B in the volume elements dr_A and dr_B given that they were at r_A^0 and r_B^0 for $t = 0$ is $\Gamma_t(r_A^0, r_B^0|r_A, r_B)dr_A dr_B$.

The compact form of Equation (1.41) masks the high complexity of the problem. First, we will study the structure of the memory function $S(t)$. Since the positions of the A and B particles are assumed to be uncorrelated – leaving aside the effects of the reaction – the two-particle propagator factorizes into the single-particle propagators for A and B. For simplicity, these propagators shall be identical and called G_t. De Gennes proposes a rather generic scaling assumption for the form of G_t, namely

$$G_t(r^0|r^1) = \frac{1}{\sigma(t)^d}G\left[\frac{|r^0 - r^1|}{\sigma(t)}\right]\,, \tag{1.43}$$

where $\sigma(t)$ is the root of the MSD, i.e. the average distance traveled by one particle until time t, and the prefactor assures normalization. For the special case of normal diffusion, the function G is a Gaussian. A general law for the memory function can now be derived:

$$S(t) = \kappa\sigma^{-d}(t)\,, \tag{1.44}$$

where the coefficient κ depends on the details of the diffusion process. The scaling with $\sigma(t)$ indicates that S is actually a measure for the exploration volume, i.e. the

volume that encloses all possible trajectories of the particle until time t. Like for the work at hand, the impact of anomalous diffusion is of special interest in the discussion of de Gennes: In this case, a scaling of the form $\sigma^2(t) \sim t^\alpha$ applies leading to a power law memory function

$$S(t) = \kappa' t^{-d\,\alpha/2}\,. \tag{1.45}$$

In terms of a random walk, let $j(t)$ denote the number of steps the walker performed until time t. Then $j(t) \propto t$ and the number of distinct sites visited $n(t) \leq j(t)$. Two regimes can be distinguished:

1. $S(t)$ decreases more rapidly than t^{-1} $(2/\alpha < d)$: Then $\sigma^d(t) > j(t) \geq n(t)$. Consequently, the number of explored sites is smaller than the number of sites actually contained within the exploration volume σ^d. This behavior is called *non-compact exploration*.

2. $S(t)$ decreases more slowly than t^{-1} $(2/\alpha > d)$: Then $\sigma^d(t) < j(t)$. The number of explored sites is larger than the number of sites actually contained within σ^d. Hence, most of the enclosed sites are visited or even oversampled. This behavior is called *compact exploration*.

Now, the solution of Equation (1.41), and in particular the resulting rate coefficient k, can be computed for the two regimes:

1. Non-compact exploration:

$$k^{-1} = \int_0^\infty S(t)dt\,, \tag{1.46}$$

   i.e. in this case k does not depend on time and resembles truly a *rate constant*.

2. Compact exploration:

$$k(t) = \frac{\sigma^d(t)}{t}\frac{\sin(\pi\,\alpha/2\,d)}{\kappa\pi} \sim t^{\alpha/2\,d-1}\,. \tag{1.47}$$

   So $k(t)$ depends on time and decays like a power law with exponent $-h \equiv \alpha/2\,d - 1$.

In particular, the following scaling relations hold for the unrestricted random walk on a simple cubic lattice [87]:

$$n(t) \sim (8j(t)/\pi)^{1/2} \text{ for } d = 1 \tag{1.48}$$

$$n(t) \sim \pi j(t)/\log j(t) \text{ for } d = 2 \tag{1.49}$$

$$n(t) \sim j(t)/1.5164 \text{ for } d = 3\,. \tag{1.50}$$

Thus in one dimension $n(t)$ grows slower than $j(t)$ indicating compact exploration. For $d = 3$ $n(t)$ scales like $j(t)$ meaning that the walker visits a new site in almost every step. This corresponds to non-compact exploration. Consequently this regime contains the classical scenario of bulk reactions under Brownian motion $(2/\alpha = 2 < d = 3)$. The two-dimensional walk resembles a marginal scenario, where logarithmic corrections apply to the scaling $n(t) \sim j(t)$.

Fractal-like Kinetics

When recalling the discussion of random walks through fractal environments in Section 1.3.4 one realizes that $\alpha/2$ is identical to the fractal dimension d_W of the random walk. From this perspective, de Gennes considered reactants that diffuse anomalously, i.e. with $d_W > 2$ ($\alpha < 1$) on a homogeneous substrate with $d_f = d$. On the other hand, one may also vary d_f, to obtain anomalous kinetics for intrinsically normal diffusive reactants. This notion underlies the field of *fractal-like reaction kinetics* that has been promoted especially by R. Kopelman and his coworkers [88]. The main aspect of fractal-like kinetics is a rate coefficient decaying like a power-law for long times:

$$k(t) = k_0 t^{-h} \quad 0 \leq h \leq 1 \quad (t \geq 0)\,. \tag{1.51}$$

The *heterogeneity exponent* h ranges between zero and unity where $h = 0$ corresponds to the classical limit. The term "fractal-like" implies that this kind of kinetics is frequently observed on fractals, like a percolating cluster, but not limited to these. Moreover, it also prevails on low-dimensional homogeneous substrates like channels for which $d_f = 1$, cf. above.

Since classical kinetics relies on homogeneous densities of reactants, initial density fluctuations that naturally arise for a stochastic, multi-particle system are neglected. Ovchinnikov and Zeldovich [89] predicted for the reaction A + B $\rightarrow \emptyset$ that these density fluctuations evolve to a macroscopic segregation into A- and B-rich. This segregation is called the *Zeldovich effect* and can indeed be observed in computer simulations [90]. The Zeldovich regime is characterized by a non-classical decay of the average concentration, namely $\sim t^{-d/4}$ ($d < 4$) instead of t^{-1}. Actually, three scaling regimes arise for equal initial densities, i.e. $\rho_A^0 = \rho_B^0$ [91]: For very short times, the reactants are well mixed and consequently classical behavior is observed. For intermediate times, depletion zones arise and

$$\langle \rho_B(\mathbf{r}, t) \rangle \sim \begin{cases} t^{-d/2}, & d \leq 2\,, \\ t^{-1}, & d > 2\,. \end{cases} \tag{1.52}$$

For longer times, macroscopic segregation emerges leading to the $t^{d/4}$ scaling of the Zeldovich regime. The heterogeneity exponent h in the rate coefficient reads $h = 1 - d/2$ before the onset of Zeldovich segregation and $h = 1 - d/4$ afterwards. Especially in three dimensions, this asymptotic depends sensibly on the boundary conditions. The Zeldovich effect has been reported for simulations with reflecting boundaries, while periodic boundary conditions effectively introduce convection currents that oppose reactant segregation [92]. Moreover finite size effects can overlay the described asymptotic [91].

Bramson and Lebowitz [93] generalized the analysis to $\rho_A^0 < \rho_B^0$ and found a rather different behavior for the minority species

$$\rho_A(t) \sim \begin{cases} \exp(-\lambda_1 \sqrt{t}) & d = 1 \\ \exp(-\lambda_2 t / \ln t) & d = 2 \\ \exp(-\lambda_d t) & d \geq 3\,. \end{cases} \tag{1.53}$$

That is $d = 2$ marks the transition between two kinetic regimes.

These discussions are valid for *batch conditions*, where the reactants are randomly distributed in the system and subsequently the reaction takes place without adding new reactants. For *steady-state* conditions reactants replenish with a fixed rate and hence the reaction proceeds constantly. Intriguingly, also in this scenario a macroscopic segregation of reactants may occur [94]. The critical dimension is then $d = 2$, meaning that for $d \geq 3$ classical kinetics prevails.

Subdiffusion-Limited Reactions

As detailed in Section 1.3.4 a random walk in a fractal environment like a percolating cluster exhibits subdiffusion. From the discussion in the preceding paragraphs one may anticipate a link between anomalous, fractal-like kinetics and subdiffusion. This leads to the notion of *subdiffusion-limited reactions*. So far, we have described the case of OD as the underlying mechanism, but there are also studies that rely on CTRW-type subdiffusion, see the article by Yuste *et al.* [95, chap. 13] for a comprehensive review.

Some results follow via the so called *subordination trick*, i.e. by performing the simple substitution $t \to t^\alpha$. For example, the concentrations for $\mathrm{A} + \mathrm{B} \to \emptyset$ with $\rho_A^0 = \rho_B^0$ are asymptotically governed by

$$\rho_B(t) \sim \begin{cases} t^{-\alpha d/4} & d < 4 \\ t^{-\alpha} & d > 4\,, \end{cases} \tag{1.54}$$

This simple subordination procedure bases on the argument that the number of steps $j(t)$ during a time interval t grows sub-linear with time, i.e. $j(t) \sim t^\alpha$. Consequently, all properties whose time dependence arises only through the number of steps follow the laws derived for normal diffusion with t^α instead of t.

This argument is closely related to the spectral dimension d_S that describes how the number of distinct sites visited by the random walk scales with time, Equation (1.33). In the Zeldovich regime $h = 1 - d_S/4$ [91, 92] with $d_S = 2d_f/d_W = \alpha \times d_f$. Hence, subdiffusive reactants with a diffusion anomaly α on a homogeneous substrate with $d_f = d$ yield $h = 1 - \alpha d/4$.

Geometry-controlled Kinetics

Another perspective on diffusion-limited reactions is the *first passage time* (FPT) T that measures how long a random walker, starting at a point S, needs to reach some target site X. This quantity used to be tractable for quasi-one dimensional and unconfined systems only, but in recent years, first the mean of T (MFPT) [96] and finally the full distribution of T [97] have been calculated for confined domains containing N sites. Two regimes emerge that coincide with the compact and non-compact exploration scenarios introduced by de Gennes, cf. above. For non-compact exploration ($d_W < d_f$) the quantity $\overline{\langle T \rangle}_X$ giving the MFPT to reach X averaged

over all starting points, scales linear with the domain size N. The same scaling arises for the MFPT $\langle T \rangle$ and is independent of the dimensions d_W and d_f.

For the compact exploration scenario, in contrast, $\overline{\langle T \rangle}_X \sim N^{d_W/d_f}$ while still $\langle T \rangle \sim N$. This implies, that several time scales are involved, beyond the MFPT. It turns out, that now the FPT depends strongly on the initial separation r between the points S and X. Bénichou *et al.* [97] hence denote the kinetics in the compact exploration regime as *geometry-controlled*. This notion incorporates all scenarios of anomalous diffusion, like fractal-like kinetics of reactants on a low-dimensional support. It hence provides a general theoretical framework for reactions in complex environments where reactant transport is anomalous.

As discussed above, classical kinetics is associated with non-compact exploration. Hence the initial conditions play no role in this case. In contrast, for geometry-controlled kinetics diffusive mixing works ineffectively and hence the behavior of the system depends on the time of the measurement, cf. [88]

1.4.3 Simulations of Reaction and Diffusion in Crowded Media

In addition to the macroscopic treatment of crowding effects by thermodynamics, cf. Section 1.2.4, full-stochastic, particle-based approaches promise new insights into reactions that occur within complex fluids. Especially the impact of non-trivial reactant transport can be studied. To this end, the large number of particles and possible interactions demands the use of computer simulations. The computational models of crowded fluids differ in their aims and degree of complexity. A large body of work deals with lattice models of biological membranes [71, 98, 99, 100]: In this approach the crowders are considered as an inert species, that moves with varying mobility compared to the reactants. If the crowders are immobile they form a fractal environment that leads to OD of reactants as described in Section 1.3.4.

This type of system shows fractal-like kinetics as found for elementary reactions like A + B $\rightarrow \emptyset$, see e.g. [88, 101, 102]. Addressing the relevance of anomalous kinetics in the cell, Berry [99] showed that biochemical reactions of Michaelis-Menten type, cf. Equation (1.1), also develop reactant segregation and non-classical kinetics on a crowded model membrane. Grima and Schnell [100] systematically analyzed the elementary reaction A + B $\rightarrow$ C under various conditions and found that the asymptotic behavior is always fractal-like kinetics. The transient towards this regime depends on the reaction probability on encounter P and the initial densities of the reactants: For small P and $[A_0] \ll [B_0]$ the kinetics is indeed classical. This implies that in experiments anomalous kinetics may not be important depending on the prevailing rates and concentrations.

Another type of model describes reactions in the cytosol or in artificial crowded solutions. The reactants and crowders are modeled as spherical moving and interacting according to a molecular dynamics or Brownian dynamics approach. A recent review by Adrian Elcock [103] discusses, among others, this type of models and their relation to *in vitro* experiments. In their study, Kim and Yethiraj [104] reproduced the results of thermodynamic calculations, that is association rates may

be accelerated or decelerated in the presence of a inert species depending on whether the reaction is diffusion- or reaction-limited, cf. Section 1.3.4. Crowder and reactants only differed by the ability to undergo a reaction and hence this scenario rather corresponded to an artificial setting of a *monodisperse* system.

Ridgway *et al.* [105] investigated a dimerization reaction in a coarse-grained model of the bacterial cytoplasm. This means that the crowder species covered a certain, experimentally grounded range of sizes and masses (*polydisperse system*). Qualitatively, the effects are the same as for a single crowder size. Additionally the authors note, that the kinetics were not only decelerated but significantly deviated from classical predictions.

Recently Grima *et al.* [106] published a study on reactions in nanoscale porous media. Their approach extents the planar lattice simulations discussed above to three dimensional, continuous space. The crowders are now immobile, randomly distributed spheres, i.e. this setup corresponds to the three dimensional *swiss cheese model* or *Lorenz gas model* (the percolation problem in three dimensions and continuous space). In such an environment, reactants show trajectories that deviate strongly from free diffusion. In particular, the anisotropy of the material gives rise to more elongated trajectory shapes. In consequence, apparent diffusion-limited association rates can be dramatically reduced as compared to the bulk scenario.

Experimental *in vitro* models for crowding effects typically rely on Dextran or Ficoll as crowders [103]. These molecules are presumed to be truly inert and consequently only provide excluded volume. From this perspective there is good qualitative agreement between simulations and experiments, but the modeling of Dextran, for example, requires particular geometric parameters depending on the system under consideration. Moreover, Dextran in solution can induce anomalous subdiffusion of tracers [24, 25, 40] a phenomenon that is usually not included in particle based simulations of bulk reactions.

1.5 Scope

The preceding introductory sections gave an overview on anomalous reactant transport and reaction kinetics in a biological context. The crowded character of the cytoplasm qualitatively alters the diffusion of particles into anomalous subdiffusion, that is the average area covered by the particles (the MSD) grows sub-linearly with time:

$$\langle \delta^2 \rangle_{\mathrm{E}} \sim t^{\alpha} \quad \text{with} \quad 0 < \alpha < 1\,. \tag{1.55}$$

Three distinct models, the CTRW, FBM, and OD, were presented that give rise to this kind of scaling. It is still debated which of these models provides the most accurate description of subdiffusion in the cytoplasm although numerous studies addressed this question recently [24, 77, 78, 79, 107].

The recent developments of single particle monitoring techniques yield sample trajectories of unprecedented accuracy. Most of the approaches to identify the mechanism behind crowding-induced subdiffusion hence exploit the information

contained in these data. Along this line the work at hand contributes a simulation study that compares different estimates of α in dependence on the diffusion process, see Section 3.1. Furthermore the impact of measurement uncertainties is discussed. Section 3.2 thoroughly analyzes the average shape of subdiffusive trajectories. It turns out that the three models CTRW, FBM, and OD, show a quite different behavior in this respect. Hence the average shape may prove as a powerful means to distinguish the different modes of motion. To test the applicability of this criterion we compare experimental data obtained by a novel SPT device with our simulations. Finally, Section 3.3 presents a proposal for a particle-based model of the cytoplasm. It accounts for the size distribution of proteins and the influence of weak, non-specific attraction between them.

So far, the computational modeling of biochemical networks bases mainly on "classical" assumptions like the perfect mixing of reactants. These assumptions may be violated in complex fluids, see e.g. [3, 4]. On the other hand, existing theoretical work on non-classical, subdiffusion-limited reaction kinetics mainly relies on OD or CTRW as model processes. Given the growing evidence that the viscoelasticity of a crowded medium evokes subdiffusion, we consider FBM as the underlying mechanism for full-stochastic reaction-subdiffusion simulations. Section 4.1 presents the results for the prototypic reaction A + B $\rightarrow$ C in two dimensions. As a more complex scenario the impact of anomalous diffusion on a double phosphorylation cycle (e.g. MAPK) is studied in Section 4.2. It turns out that spatio-temporal effects as described in [108] are more pronounced when reactants move subdiffusively.

Chapter 2

Methods

2.1 Simulation of Diffusion

2.1.1 Lattice Gas Model

The close relationship between Brownian motion and a random walk feeds a conceptually simple and widely used method to simulate diffusing particles, namely the *lattice gas model* or *lattice gas automaton* (LGA). The particles occupy the nodes of a regular lattice and in every instant of time they travel along an edge to a neighboring site with some probability p_m that is gauged according to the desired diffusion constant D:

$$p_\mathrm{m} = 2dD\frac{\Delta t}{\Delta x^2} \,, \tag{2.1}$$

where d is the spatial dimension, Δx the distance between two lattice nodes, i.e. the discretization length, and Δt the time increment. In its simplest form with $p_\mathrm{m} = 1$ the LGA resembles a straight-forward Monte Carlo algorithm [109, 110]. In every time step, a random number from the range $[0, 1, \ldots, 2d]$ determines in which direction the walker moves next. Emulation of a particular diffusion coefficient D leads to $p_\mathrm{m} < 1$. This means, that a walker resides at its current position until another generated, uniformly distributed random number $\omega \in [0, 1)$ fulfills $\omega < p_\mathrm{m}$. Excluded volume can readily be implemented into the LGA by prohibiting multiple occupation of lattice sites. The walker behaves as a "blind ant" in the sense that it stays at its current position if the proposed move ends in an already occupied site [111]. In other words, before the move is proposed the walker has no information about forbidden sites in its vicinity.

2.1.2 Brownian Dynamics

The *Brownian dynamics* (BD) simulation technique exploits the description of Brownian motion by the Langevin equation

$$m\frac{d^2\mathbf{x}}{dt^2} = -m\zeta\frac{d\mathbf{x}}{dt} + \mathbf{F}(\mathbf{x}, t) + \xi(t)\,. \tag{2.2}$$

As extension to Equation (1.13) an additional force $\mathbf{F}$ is introduced that arises from inter-particle potentials, i.e. repulsion and attraction. In the context of this work

the *overdamped limit* is considered:

$$\frac{m}{\zeta}\frac{d^2\mathbf{x}}{dt^2} \ll \frac{d\mathbf{x}}{dt} \quad \Rightarrow \quad \frac{d\mathbf{x}}{dt} \approx \xi(t) + \mathbf{F}\,. \tag{2.3}$$

This assumption corresponds to the regime of small Reynolds number, i.e. for systems that are dominated by viscosity rather than by inertia, cf. Section 1.3.4. This especially applies to the small length scales of intracellular processes. The simulation algorithm transfers each bead from its position $\mathbf{x}(t)$ at time t to a new position $\mathbf{x}(t+\Delta t)$ according to the equation

$$\mathbf{x}(t+\Delta t) = \mathbf{x}(t) + \mathbf{R}_c(\Delta t) + \frac{D_0}{k_\mathrm{B}T}\cdot\mathbf{F}(t)\cdot\Delta t\,, \tag{2.4}$$

where Δt denotes the time interval over which the equations of motions are integrated. It corresponds to one "time step", i.e. the temporal resolution of the simulations. Equation (2.4) contains two contributions to the total displacement of the particle:

1. *random displacement* $\mathbf{R}_c$ given by white noise

$$\langle\mathbf{R}_c\rangle = 0 \qquad \langle\mathbf{R}_c^2\rangle = 6D_0\Delta t\,, \tag{2.5}$$

2. *displacement due to forces* acting on the bead

$$\mathbf{R}_f(\Delta t) = D_0/k_BT\cdot\mathbf{F}(t)\Delta t\,. \tag{2.6}$$

D_0 denotes the diffusion coefficient of the particle in bulk water. In summary, BD is more realistic than the LGA method as it does not incorporate a discretization of space. This gain in accuracy comes at the price of higher computational effort, especially for a system of many interacting particles.

Excluded Volume Interaction

One possibility to account for the volume of the particles is to use a Monte Carlo-style *move rejection* in close analogy to the blind ant variant of the LGA: If a proposed move would produce an overlap between two particles the algorithm rejects it and the respective particle stays at its current position. This approach ensures hard sphere exclusion at all times. Note that not all center-to-center distances need to be calculated to detect an overlap between any two beads owing to the short-range character of volume exclusion. The Verlet-table algorithm keeps a list for every bead that contains all possible interaction partners within some cut-off distance. Only these are relevant for collision in the next few simulation steps [109]. A further speed up can be gained when the tables are assigned to regions of space rather than individual particles. This method divides the simulation volume into equally sized cells that are small compared to the whole volume but larger than the interaction radius, in case of excluded volume, for example, $2R$. Collisions may only occur with particles that reside in the same cell or one of its neighbors.

The so-called *soft core potential* provides another way to implement excluded volume interactions. In this case, the repulsion between colliding beads is explicitly realized as a force. Again the short-range character of the interaction allows the use of Verlet-tables and cell structure for more efficient computing. The effective distance between the particles is calculated by

$$d' = d - R_i - R_j \,, \tag{2.7}$$

where $R_{i,j}$ denotes the radii of the beads and d the distance between their centers. The two particles i and j may overlap ($d' < 0$) but are then driven apart by a constant force with amplitude

$$A = 6\pi\eta \cdot 10^3 \ \mu\text{m}^2/\text{s}; \quad \eta = \eta_{water} = 10^{-3} \ \text{Pa s} \ . \tag{2.8}$$

As their effective distance increases ($d' > 0$) the force drops linearly to zero over a scale of $R_d = 2$ nm:

$$F = A \cdot \left(1 - \frac{d}{R_d}\right) \tag{2.9}$$

Figure 2.1 shows schematically the course of the force experienced by two particles of size R as a function of the distance d between their centers. Since soft beads can overlap the distinct definition of the particle size is difficult. Here, the "core" of radius R, i.e. the extension of the force plateau, defines the bead size. In fact, due to the gradually decreasing force regime between $d = 2R$ and $d = 2R + R_d/2$, the apparent particle size is larger. One can obtain an empirical correction factor by comparison of soft and hard bead simulations. Since the soft repulsive potential does not contain a divergence at $d = 2R$ in contrast to hard sphere repulsion, the algorithm can exploit larger integration times Δt to reach longer time scales.

Attractive Interaction

Besides the excluded volume effect, the change of diffusion due to nonspecific attractive forces between beads is studied. The attractive force is implemented analogously to the excluded volume interaction. Starting from an effective distance $d = R_d$ the force drops linearly to a minimum of

$$B = -b \cdot k_B T/\ \text{nm} \quad \text{with}\, b = 1.0 \ldots 3.0 \ . \tag{2.10}$$

Afterwards the force increases linearly to the long distance limit $F_\infty = 0$. The attractive force acts over a range of 2 nm in total. The complete course of the force between two particles with identical radii R is shown as a function of their center-to-center distance in Figure 2.1.

2.2 Simulation of Subdiffusion

2.2.1 Continuous Time Random Walk (CTRW)

The simulation of a CTRW process relies on the LGA with one important modification: After every step a waiting time τ is drawn from a heavy-tailed distribution, i.e.

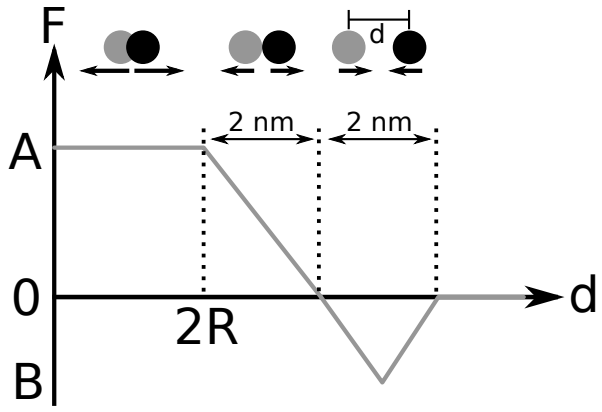

Figure 2.1 Course of the force F between two soft beads of size R as a function of their center-to-center distance d. If the beads overlap they are repelled from each other by a constant force with amplitude A. As d increases above $2R$ the force drops linearly to zero over a length of $R_d = 2\,\mathrm{nm}$. In a model for non-specific attraction, it drops further, becoming negative until $F = B$, and increases again with the same absolute slope to zero.

$P(\tau) \sim 1/\tau^{1+\alpha}$. Only after waiting for τ time steps, the walker may proceed to its next position. The parameter α coincides with the desired (ensemble-averaged) diffusion anomaly of the process.

2.2.2 Obstructed Diffusion (OD)

The simulation of an OD scenario involves two stages: First, the environment (also: support) is generated and, second, a "blind ant" random walk is performed on the remaining lattice sites. The diffusion process works exactly as described before, but now obstacles occupy a substantial subset of the lattice sites and thereby obstruct the motion of the random walker. The way in which the obstacles are placed on the lattice depends on the desired shape of the support. Here, we are interested in a type of a random fractal, namely a percolation system. A straight-forward Monte Carlo algorithm generates realizations of such a fractal as follows: It picks a lattice site by random. If it is vacant, an obstacle is placed there, otherwise another lattice site is drawn. The algorithm repeats this procedure for a predefined number of obstacles.

2.2.3 Fractional Brownian Motion (FBM)

The simulation of fractional Brownian motion (FBM) and its incremental process, fractional Gaussian noise (FGN), requires more sophisticated methods than those discussed above. Due to the correlated increments it constitutes a strictly *non-Markovian* process, i.e. a diffusive step depends not only on its predecessor but on the complete history of the process. Typical Monte Carlo methods cannot be

used as they are by construction Markovian. By now, various methods have been described that allow for the simulation of processes with memory. Especially the case of FBM/FGN has attracted much interest due to its wide applicability. An exhaustive review on various simulation techniques including a discussion of their accuracy and impairments can, for example, be found in the Master's thesis of A. B. Dieker [112]. For the thesis at hand essentially two methods were used, the exact *circulant method* and the approximative *Weierstrass-Mandelbrot function method*.

Circulant Method

The circulant method is an *in principle* exact simulation technique to generate random samples of an arbitrary Gaussian process. The term "in principle" refers to the theoretical case of infinite numerical accuracy and the use of truly independent random numbers – conditions that cannot be fulfilled in computer simulations since they rely on pseudo-random numbers and the finite accuracy of binary number representation. In the following we adopt the notation and arguments of Wood and Chan [113] who generalized an algorithm firstly presented by Davies and Harte [114].

Let X be a zero mean stationary Gaussian process $X = \{X(t) : t \in \mathbb{R}\}$ with a given covariance function γ. The aim of a simulation is now to generate a random vector with n elements, $\hat{X} = (X(0), X(1/n), \ldots, X((n-1)/n))^T$, that complies with this covariance structure and, of course, possesses all other properties of X, that is $\hat{X}$ $\mathcal{N}_n(0, G)$ with

$$G = \begin{pmatrix} \gamma(0) & \gamma\left(\frac{1}{n}\right) & \ldots & \gamma\left(\frac{n-1}{n}\right) \\ \gamma\left(\frac{1}{n}\right) & \gamma(0) & \ldots & \gamma\left(\frac{n-2}{n}\right) \\ \vdots & \vdots & & \vdots \\ \gamma\left(\frac{n-1}{n}\right) & \gamma\left(\frac{n-2}{n}\right) & \ldots & \gamma(0) \end{pmatrix} . \tag{2.11}$$

G is a *Toeplitz matrix*, that means the elements along each descending diagonal from left to right are equal. In general, any Toeplitz matrix can be embedded into a circulant matrix (which is a special form of a Toeplitz matrix) of size m $C(m \times m)$:

$$C = \begin{pmatrix} c_0 & c_1 & \ldots & c_{m-1} \\ c_{m-1} & c_0 & \ldots & c_{m-2} \\ \vdots & \vdots & & \vdots \\ c_1 & c_2 & \ldots & c_0 \end{pmatrix} . \tag{2.12}$$

In a circulant matrix the elements of each row are shifted one place to the right relative to the preceding one. The importance of circulant matrices for numerical analysis arises from their property to be diagonalized by the discrete Fourier transform (DFT). Here, $G(n \times n)$ becomes part of $C(m \times m)$ with $m = 2^g$ for some integer g

and $m \leq 2(n-1)$ by setting

$$c_j = \gamma\left(\frac{j}{n}\right) \qquad \text{if} \quad 0 \leq j \leq \frac{m}{2} \tag{2.13}$$

$$= \gamma\left(\frac{m-j}{n}\right) \qquad \text{if} \quad \frac{m}{2} \leq j \leq m-1\,. \tag{2.14}$$

So by construction C is symmetric and G comprises its upper left $n \times n$ submatrix. For a general random process with covariance function γ C is not necessarily positive definite, and hence may not represent a covariance matrix. There are strategies to deal with such situations described in [113]. C is positive-definite in the case of FGN, where $\gamma(\tau) = ((\tau-1)^{2H} - 2\tau^{2H} + (\tau+1)^{2H})/2$ (Equation (1.26)), and thus for the purpose of this work, the described embedding procedure can be applied without restriction.

Now, a random vector $Y = (Y_0, Y_1, \ldots, Y_{n-1})^T \sim \mathcal{N}_m(0, C)$ can be generated, that by virtue of the described construction of C contains a subvector $(Y_0, \ldots, Y_{n-1})^T \sim \mathcal{N}_n(0, G)$ with the desired properties of $\hat{X}$. The computation of Y starts from the representation of C in its eigenbasis

$$C = Q\Lambda Q^* \quad \text{where} \quad \Lambda = \operatorname{diag} \lambda_0, \ldots, \lambda_{m-1}\,. \tag{2.15}$$

λ_i are the eigenvalues of C, and the unitary matrix Q reads

$$q_{jk} = m^{-1/2} \exp\left(-\frac{2\pi i j k}{m}\right)\,, 0 \leq j,k \leq m-1\,. \tag{2.16}$$

Note that the DFT of the sequence $\{c_0, c_1, \ldots, c_{m-1}\}$ determines the eigenvalues of C:

$$\lambda_k = \sum_{j=0}^{m-1} c_j \exp\left(-\frac{2\pi i j k}{m}\right),\ k = 0, 1, \ldots, n-1 \tag{2.17}$$

The sampling procedure now shall generate a random vector $Y = C^{1/2}Z = Q\Lambda^{1/2}Q^*Z$ with $\Lambda^{1/2} = \operatorname{diag} \lambda_0^{1/2}, \ldots, \lambda_{m-1}^{1/2}$ and $Z = (Z_0, Z_1, \ldots, Z_{m-1})^T$ a vector of independent $\mathcal{N}(0,1)$ random variables. Under these preliminaries $Y \sim N_m(0, C)$ since Q is unitary. In the first step, the vector $Q^*Z = S + iT$ is simulated, by generating two independent $\mathcal{N}_m(0,1)$ random vectors, one for the real and one for the imaginary part (see [113] for a proof that S and T are independent). From this, one can compute the vector $W = \Lambda^1/2Q^*Z$. The desired sample $\hat{X} = (X(0), X(1/n), \ldots, X((n-1)/n))^T$ results from

$$X\left(\frac{k}{n}\right) = \sum_{j=0}^{m-1} (W_j/m^{1/2}) \left(-\frac{2\pi i j k}{m}\right)\,, k = 0, 1, \ldots, n-1\,. \tag{2.18}$$

The essence of the circulant method is the efficient calculation of Equation (2.17) and Equation (2.18) with the fast Fourier transform algorithm (FFT). For a sample size of m, the best case runtime thus becomes $\mathcal{O}(m \log m)$ when $m = 2^g$. In practice, the power m is chosen to be $2n$. We note that the circulant method always generates a full time of length n and cannot be used to compute correlated increments on demand.

Weierstrass-Mandelbrot Function

The Weierstrass-Mandelbrot function extends the peculiar Weierstrass function (1872) that is continuous but nowhere differentiable. The graph of this function has a Hausdorff dimension exceeding unity and is scale free. Thus it is well suited to model fractal phenomena. In the following we will stick to the thorough discussion in [115]. The complex valued function reads

$$W(t) \equiv \sum_{n=-\infty}^{\infty} \frac{(1 - \mathrm{e}^{\mathrm{i}\gamma^n} t)\mathrm{e}^{\mathrm{i}\phi_n}}{\gamma^{\alpha/2n}} , \tag{2.19}$$

where $0 < \alpha < 2$ imposes self similarity, $\gamma > 1$ is a parameter, and the ϕ_n are arbitrary phases from $[0, 2\pi)$. The values γ^n can be interpreted as frequencies that span from zero to infinity in geometric progression, and hence constitute a "Weierstrass spectrum". If the phases ϕ_n are chosen randomly one obtains a stochastic function. As a sum of infinitely many random contributions, $W(t)$ is even a Gaussian random function. An analysis of the increments $W(t + \tau) - W(t)$ reveals zero mean and an auto-covariance that only depends on τ. Consequently, the series of increments of $W(t)$ is stationary. Interestingly, the autocovariance function itself resembles a Weierstrass-Mandelbrot function, with a self-similarity parameter $\alpha' = 2\alpha$. The power spectrum of W can be approximated by a continuous form: $\overline{S}(\omega) \approx 1/(\ln(\gamma)\omega^{1+\alpha})$. Furthermore the fractal dimension of the path of W complies with $2 - \alpha/2$. Notably, the derivation of this result contains an argument that strictly applies for irrational γ only (see [115] for details). In all, the process defined by $W(t)$ shares important characteristics with FBM and thus may be used to generate FBM samples.

For the purpose of simulation the real part of Equation (2.19) is slightly rewritten:

$$w(t) = \sum_{n=-\infty}^{\infty} \frac{\cos(\phi_n) - \cos(\gamma^n t^* + \phi_n)}{\gamma^{n\alpha/2}} . \tag{2.20}$$

As stated above, irrational γ are favorable, so in our simulations we set $\gamma = \sqrt{\pi}$. In $w(t)$ time is measured in units of 2π, i.e. a complete simulation run with T time steps corresponds to a full period. Thus, in order to simulate arbitrarily long time series, t has to be transformed according to $t^* = 2\pi t/T$. $w(t)$ contains an infinite sum that requires a truncation in practice. The limits $n_{\min}$ and $n_{\max}$ have to be chosen empirically [115]. We use $n_{\min} = -8$, $n_{\max} = 48$ that proved as a good trade-off between accuracy and fast computations in earlier studies [116, 117]. From the truncated version of Equation (2.20) a FBM sample is obtained in a straight-forward fashion, as $w(t)$ directly corresponds to the position of the FBM process at time t where $w(0) = 0$. Furthermore, the incremental process $dw(t)$, i.e. FGN, can be obtained by calculating the differences $dw(t) = w(t + \Delta t) - w(t)$.

The bottleneck of this method is the calculation of 57 cosine values twice in every simulation step. For a sample of 10^6 data points the reference computer needs 14 seconds. The calculations can be accelerated when the values $\cos(\phi_n)$ are computed once and stored for further use. For the study at hand, therefore the cosine of 10^5

equally spaced angles in $[0; 2\pi]$ were precalculated and stored in a random-access data structure. The error due to the angle discretization is negligible. By these actions the computations are accelerated by almost a factor of five. As the operations are identical in every step, the complexity of the Weierstrass-Mandelbrot method is of the order $\mathcal{O}(T)$ when T is the total number of steps. It is thus faster than the circulant method, i.e. the fastest exact method available. A further advantage is the possibility to calculate the next step on demand, which can save many computations in the simulation of reacting particles, as will be described below.

2.3 Simulation of Reaction-Diffusion Processes

2.3.1 Full-stochastic Simulations

Over the last decades, the interest in modelling biochemical reactions and reaction networks within the living cell has grown tremendously [6]. The possible approaches are manifold in the assumptions they make [12, 13, 118]: Deterministic methods assume high abundance of reactants and consequently use a continuous description in terms of reactant concentrations. The system is then described by a set of coupled differential equations. Stochastic approaches, in contrast, work on the level of – eventually small – reactant numbers. The chemical master equation is solved by using approximative methods like the chemical Langevin equation [12, 119, 120]. Both classes of approaches have in common that they rely on well-stirred conditions, i.e. on (locally) homogeneous concentrations. The work at hand abandons this assumption in that the motion of reactants is non-trivially modified to anomalous subdiffusion. To this end, a full-stochastic, i.e. particle based, simulation method is applied.

For reactants undergoing Brownian motion, several efficient stochastic simulation algorithms have been developed, e.g. *Green's function reaction dynamics (GFRD)* [121] and *first-passage Monte Carlo* algorithms [122, 123]. To our knowledge, nothing equivalent exists for subdiffusive reactants. Consequently, we rely on the explicit simulation of the individual particles that eventually react on an encounter [118, 124]. The trajectories are generated via the Brownian dynamics and FBM approaches as described above. The particles are realized as phantom spheres with an interaction radius radius R. Each belongs to one of the involved chemical species, e.g. A, B, or C in the case of a A + B $\rightarrow$ C reaction.

In the particle based picture, reaction rates are represented by probabilities. For the example A + B $\leftrightharpoons$ C the decay part is determined by p_2, that is the probability for each C in the system to become an A-B pair during one time step Δt. Then the corresponding rate reads $\nu_2 = k_2\rho_A = p_2/\Delta t\,\rho_A$. On the other hand, the complex formation is a diffusion-influenced second order reaction: When two reaction partners overlap with their reaction radii, a random number ω is drawn. For $\omega < p_1$ a reaction takes place and the two particles merge to form a C. The relation between p_1 and the respective rate coefficient k_1 is not as straight-forward as for a first order reaction. In principle, an adequate tuning of R and p_1 allows to emulate a particular bimolecular

reaction rate [124]. Here, the focus is on generic effects and we use the relation $k_1 = c_1 p_1/\Delta t$ with an empiric factor c_1 to compare our simulations with theoretical predictions, cf. [99, 118].

Throughout our simulations we apply *batch conditions* [88]: The system is set up by randomly distributing the reactants in the simulation box. Then the reaction-diffusion process runs without providing new substance and the system tends towards an equilibrium state which in general differs from the initial configuration.

2.3.2 Limitations and Impairments

The described approach does not cover the effects of excluded volume between the reactants. Rejecting or cutting trial moves, as it is typically performed in particle based reaction-diffusion simulations (see above), distorts the correlation structure of subdiffusive increments and thus may lead to unforeseen side effects. The problem actually originates in the violation of the fluctuation-dissipation theorem as we treat the FGN as an *external* stochastic force [81]. Implementation of interparticle forces (attraction/repulsion) would hence require a more rigorous approach via a generalized Langevin equation to fulfill a fluctuation-dissipation relation between noise and friction.

We neglected the effects of particle interactions for computational reasons because phantom spheres allow for larger systems and longer simulation times. Moreover, the (long term) observations described in this work are independent of the excluded volume in the case of ordinary Brownian motion. Although the quantitative results may differ, the qualitative observations, i.e. anomalous kinetics, reactant segregation, etc., are present even if the excluded volume of the reactants is neglected. Section 4.1.3 discusses this issue in detail for the prototypic A + B $\rightarrow$ C reaction.

We mentioned that our method for simulating subdiffusion does not fulfill a fluctuation-dissipation theorem. Furthermore, the subdiffusion process is determined by the correlation between the increments, hence arbitrary removal or modification of increments in the time series will distort the autocorrelation structure of the process, at least locally. In particular, this applies for reversible reactions like A + B $\leftrightharpoons$ C : If A becomes part of a complex at time t_1 and this complex decays again at t_2, the trajectory of A lacks the increments in $(t_1 \dots t_2)$ that would influence all following steps. For subdiffusive FBM and not too fast reactions this distortion can be neglected since for $H < 0.5$ FBM resembles a short memory process, cf. Section 1.3.4.

Figure 2.2 (a) shows the empirical autocorrelation function (acf) for simulated FGN time series with $H = 0.3$ and $H = 0.4$. For comparison the circulant and Weierstrass-Mandelbrot function (WMF) method have been used for simulation. At very short lag-times τ the increments of the time series exhibit anti-correlation that grows as H is lowered, indicating anti-persistent motion. With increasing τ the acf drops quickly beneath the 5%-significance limit and the increments become practically independent after 3-4 steps. This is especially seen in the curve generated by the circulant method. The WMF method leads to a more complex acf that itself

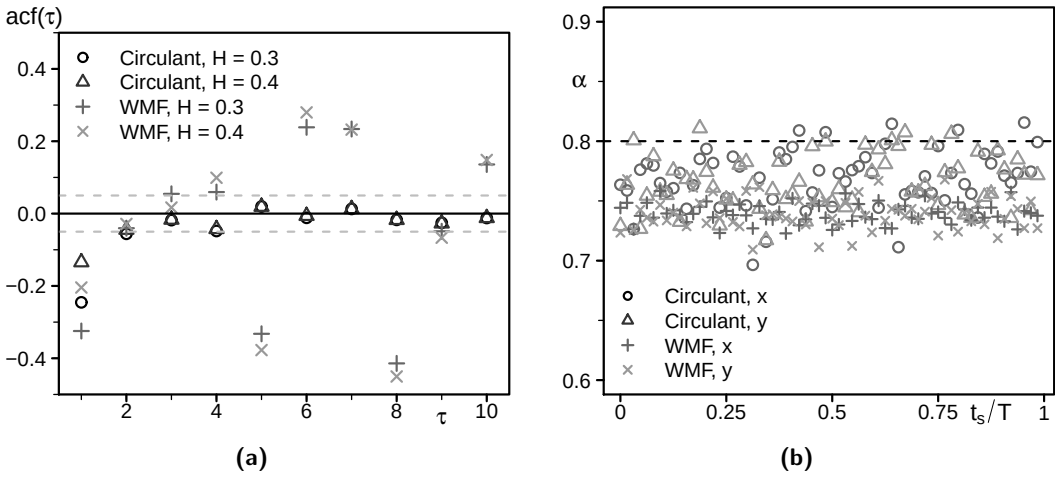

Figure 2.2 (a) The autocorrelation functions (acf) of FGN samples with $H = 0.3$ and $H = 0.4$ generated by the WMF and circulant method. The acf indicates anti-correlation for short lag-times τ that quickly decays beneath the 5% significance level. The WMF method produces a more complicated acf that itself resembles a WMF. (b) Measured diffusion anomaly of subsets of a FGN sample with $T = 8192$ steps. t_s gives the starting point of each subset with a size of 128. The systematic deviation from the imposed anomaly ($\alpha = 0.8$, broken line) originates in the limited accuracy of the FGN fitting procedure.

resembles a WMF (see above). Still the generated time series has only short memory. To check whether subsets of a FGN series possess the desired features of the full sample we fitted FGN to pieces of 128 steps using the method proposed by McLeod *et al.* [125]. The results in Figure 2.2 (b) show that the measured diffusion anomaly α spreads homogeneously around a mean value that is somewhat lower than the imposed one ($\alpha = 0.8$, broken line). This systematic deviation probably originates in the limited accuracy of the fitting procedure for small sample sizes since both simulation techniques yield the same behavior. All subtrajectories are characterized by the same average diffusion anomaly indicating that any (not too small) subset of a FGN sample shares the features of the full series.

In summary, our approach to the simulation of reaction-subdiffusion using FBM trajectories is conceptually simple and fast given the non-Markovian nature of this process. Future improvements could implement excluded volume interactions. So far these are included in a kind of mean-field that bears the FBM-type subdiffusion of the reactants. Hence, the particles are considered as phantoms and reactive collisions cannot simulated explicitly. Consequently the mapping of the simulation parameters to realistic reaction rates is complicated. Nevertheless, the generic observations are in excellent agreement with existing studies on anomalous reaction kinetics, see Section 4.1.3 for details.

Chapter 3

Crowding-induced Subdiffusion

3.1 Challenges in Determining Anomalous Diffusion in Crowded Fluids

The results presented in this section have been accepted for publication in *Journal of Physics: Condensed Matter*[1].

3.1.1 Introduction

Despite the frequent observation of subdiffusion in crowded fluids, the origin of the anomaly, i.e. the microscopic mechanics of crowding-induced subdiffusion, has remained controversial. The most prominent theoretical models that are commonly employed are (i) a continuous time random walk (CTRW) [20], (ii) fractional Brownian motion (FBM) [60], and (iii) obstructed diffusion in a disordered environment (OD) [68], cf. Section 1.3.4.

The above models have been introduced to rationalize the observation of subdiffusion in crowded media. However, an unambiguous identification of the stochastic process underlying crowding-induced subdiffusion has not yet been possible, see Section 1.3.5. In recent times, various analysis protocols have been proposed to address this question. For example, Szymanski and Weiss [24] compared the histograms of diffusion anomalies measured via FCS with simulations of the three models for subdiffusion. Tejedor *et al.* [78] computed the statistics of the maximum excursion of SPT trajectories and combined this with a growing sphere analysis. In general, the growing body of high quality SPT data allows sophisticated methods to be applied that eventually can identify whether a given model describes the studied system or not. Along this line, the approach of Magdziarz *et al.* [77] shall be further examined in the following. It is based on the p variations of the particle displacements, a concept that we describe below.

Here, we have investigated the applicability of the p variation for experimentally realistic data and compared the results to other common approaches, e.g. direct fitting of the MSD. As a result, we have found that SPT data and FCS curves yield the same distributions of the diffusion anomaly, α, for FBM and OD irrespective

[1] M. Hellmann, J. Klafter, D. W. Heermann, and M. Weiss, Challenges in determining anomalous diffusion in crowded fluids, *Journal of Physics: Condensed Matter*, *accepted* (2010)

of the evaluation method. Furthermore the influence of experimental uncertainties of the particle positions in a SPT setup was studied by superimposing a Gaussian blur to the trajectories in each frame. In accord with [27] we find that analyzing a blurred trajectory leads to a systematic underestimation of α, regardless of the underlying mechanism and the evaluation method. This discrepancy between the inherent anomaly of the process and the measured one becomes increasingly relevant when the uncertainty reaches the scale of the typical positional increment between two successive frames. For ergodic scenarios like OD and FBM, time- and ensemble-averaged MSD provide values for α that are equally affected by the blurring. This is in contrast to a CTRW, where the anomaly obtained from the time-averaged MSD ($\alpha \approx 1$) is much more sensitive than the result from the ensemble-averaged MSD ($\alpha < 1$). This phenomenon may hamper the detection of ergodicity breaking in experiments as the same scaling of time- and ensemble-averaged MSD is measured when the positional uncertainty is of the order of the average increment between two successive frames.

3.1.2 Parameters, Setup, and Analysis

The CTRW and OD trajectories – including the marginal case of Brownian motion – were generated by the corresponding modifications of the LGA algorithm, cf. Section 2.2.1 and Section 2.2.2. For the simulation of FBM the Weierstrass-Mandelbrot function was applied, see Section 2.2.3. Table 3.1 summarizes the important paremeters. We analyzed the simulated trajectories with various methods that are discussed in the following.

Fluorescence Correlation Spectroscopy simulations

The FCS method has been described in Section 1.3.2. For the simulation of FCS we assumed a Gaussian confocal volume of width $r_0 = 250$ nm around the center of the system. The cumulative fluorescence signal of all tracers within the confocal volume was calculated at every time step and autocorrelated after 10^7 time steps. Thus the analysis covered the time scales $5\ \mu\text{s} \cdots 50$ s. The resulting curve was fitted with the theoretical autocorrelation function (equivalent to Equation (1.7) with $q = 0$, cf. [25]):

$$C(\tau) = \frac{1/N}{1 + (\tau/\tau_D)^{\alpha_{\text{FCS}}}} \ . \tag{3.1}$$

to extract the diffusion anomaly α_{FCS} and the mean residence time τ_D within the confocal volume.

For each parameter set, $N_r = 50$ runs were performed to build histograms of the measured anomalies. In each run, $K = 300$ fluorescent tracers were simulated so that the average number of tracers in the confocal volume, N, was of the order of ten.

Single Particle Tracking simulations

Simulating a SPT experiment required storing the particle positions at particular time points. For this study the time interval between two measurements was $\Delta t_{\mathrm{SPT}} = 100 \times \Delta t$, i.e. 0.5 ms. This interval is somewhat faster than typical experimental systems that currently allow for frame rates of about 100 s^{-1}. To relate to this experimental situation, we increased Δt_{SPT} tenfold for part of the analysis, i.e. we only considered every 10th point of the time series. The total simulation time T was $10^6 \Delta t$ (=5 s) and a single tracer was tracked in $N_r = 500$ independent runs per parameter set.

The diffusion anomaly of a SPT experiment is recovered from the slope of the (ensemble-averaged) MSD as

$$\alpha = \frac{d \log \langle \delta^2 \rangle_{\mathrm{E}}}{d \log t} \ . \tag{3.2}$$

The anomaly α may also be obtained from the time-averaged MSD which is defined as [Equation (1.18)]

$$\langle \delta^2 \rangle_{\mathrm{T}} = \frac{1}{T-t} \int_0^{T-t} \sum_{i=1}^{2} \left[x_i(\tau + t) - x_i(\tau) \right]^2 d\tau \ . \tag{3.3}$$

Here, τ denotes the lag time that takes the role of t in Equation (3.2), cf. Section 1.3.4. We note already at this point that single-particle trajectories naturally suffer from measurement errors that can be as big as 100 nm (depending on the camera frame rate).

Parameter	FCS simulations	SPT simulations
Δt	5×10^{-6} s	=
Δt_{SPT}	-	5×10^{-4} s
T	50 s	5 s
Δx	10 nm	=
L	350 nm	=
r_0	25 nm	-
K	300	1
N_r	50	500
D	1.6 $\mu\mathrm{m}^2/\mathrm{s}$	=

Table 3.1 The parameters of the FCS and SPT simulations.

p variation analysis

To go beyond a mere determination of the anomaly, i.e. to elucidate which stochastic process is actually observed, the p variation method has been introduced recently

[77]. Formally, it is defined as the limit

$$V^{(p)}(t) = \lim_{n\to\infty} V_n^{(p)}(t), \tag{3.4}$$

where the partial sum of increments of the stochastic process $X(t)$ is given as

$$V_n^p(t) = \sum_{j=0}^{2^n-1} \left| X\left(\frac{(j+1)T}{2^n} \wedge t\right) - X\left(\frac{jT}{2^n} \wedge t\right)\right|^p \tag{3.5}$$

with $a \wedge b = \min(a, b)$. Experimental trajectories can only yield an approximation of the p variation via $V_n^p(t)$ where n is limited by the trajectory length.

For a FBM process with Hurst parameter H the p variation is as follows: The approximated p variation of order n is linear in time. For $p > 1/H$, $V^{(p)}(t) = \infty$, i.e. the slope of $V_n^{(p)}(t)$ increases with n. The opposite situation is encountered for $p < 1/H$, where $V^{(p)}(t) = 0$, i.e. the slope of $V_n^{(p)}(t)$ decreases with growing n. In the special case $p = 1/H$ the curves of $V_n^{(p)}(t)$ collapse for increasing n onto a single master curve that, for normalized FBM, is given by $V^{(p)}(t) = t\left\langle |B_H(1)|^{1/H}\right\rangle$. Here, $B_H(1)$ is a one-step FBM process with Hurst parameter H, while $\langle\cdot\rangle$ denotes the expectation value. The special case of Brownian motion ($H = 1/2$) is included in this discussion: The 'total variation' ($p = 1$) is infinite while the 'quadratic variation' ($p = 2$) is proportional to time.

For diffusion on a fractal the p variation behaves similarly. It is finite only for $p = d_W$, where d_W denotes the fractal dimension of the walk. Calculations supporting this notion exist for a Sierpinski gasket embedded in two dimensions [77]. In the case of diffusion on a percolation cluster $d_W = 2/\alpha$, i.e. the p variation should be finite for $p = 2/\alpha$ in accordance with the result for FBM.

We used a simple approach to quantify the deviation between $V_n^{(p)}(t)$ among different orders n: First a mean variation $\langle V_n^{(p)}(t)\rangle_n$ is calculated at time t. Then the cumulative quadratic difference

$$\omega^2(p) = \sum_{\forall n,t} \left(V_n^{(p)}(t) - \left\langle V_n^{(p)}(t)\right\rangle\right)^2 . \tag{3.6}$$

provides a single number for every p. By varying p over a plausible range in steps of 0.005, a minimum of $\omega^2(p)$ can be found at $p_{\min}$ from which one can estimate the anomaly as $\alpha_{\mathrm{P}} = 2/p_{\min}$. In this way, for each SPT trajectory an estimated diffusion anomaly is obtained.

To render the simulations comparable to real SPT experiments we analyzed trajectories with a length of 2^9 positions and a time increment $\Delta t_p = 5$ ms. Hence, the resolutions $n = 7, 8, 9$ were considered in the summation of Equation (3.6).

3.1.3 Results and Discussion

Determining diffusion anomalies: FCS vs. SPT

Since quantifying the diffusion anomaly has been done by FCS and SPT in the literature (see Section 1.3.3), we first investigated whether the two methods indeed

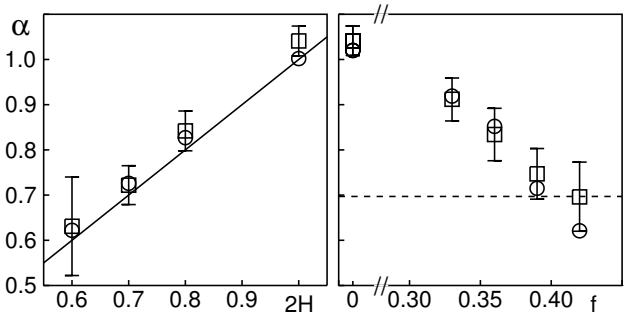

Figure 3.1 The diffusion anomaly α as obtained by FCS and SPT (open squares and circles, respectively) shows only minor differences. For FBM (left), the imposed anomaly $2H$ with the Hurst parameter H is plotted on the abscissa. The full line indicates the expected values $\alpha = 2H$. For OD (right) the abscissa shows the occupied volume fraction f. For $f > 0.4$ the anomaly converges towards the limiting value at the percolation threshold (indicated by dashed line). In both cases, error bars for SPT data are smaller than the symbol size.

yield the same results for α. For FCS simulations (FBM and OD) we fitted the anomalous diffusion model Equation (3.1) to the autocorrelation curve and obtained from that α_{FCS}. For the analogous SPT simulations, three methods were applied to determine the anomaly:

1. fitting of $\langle\delta^2\rangle_{\mathrm{E}}$ [Equation (3.2)] $\Rightarrow \alpha_{\mathrm{E}}$,

2. fitting of $\langle\delta^2\rangle_{\mathrm{T}}$ [Equation (3.3)] $\Rightarrow \alpha_{\mathrm{T}}$,

3. using the p variation $\Rightarrow \alpha_{\mathrm{P}}$.

Unlike the first approach, the latter two yield an anomaly for each trajectory, hence allowing one to inspect the distribution of anomalies.

As expected for ergodic processes like FBM and OD, $\langle\delta^2\rangle_{\mathrm{E}}$ and $\langle\delta^2\rangle_{\mathrm{T}}$ yielded the same anomaly values. Comparing these results with α_{FCS} obtained for the same scenario revealed no significant difference between the two experimental methods (Figure 3.1). Besides a larger standard deviation due to the lower amount of FCS curves, the mean anomaly did not show any method-specific shift. For the OD scenario, a crossover between subdiffusion and normal diffusion may occur during the simulation period for low values of f since an asymptotic subdiffusion characteristics can only be expected at the percolation threshold [71]. As a consequence, the estimates of FCS and SPT were compatible only when the respective fits were performed in the same time intervals ($10^{-4} \ldots 2 \times 10^{-1}$ s).

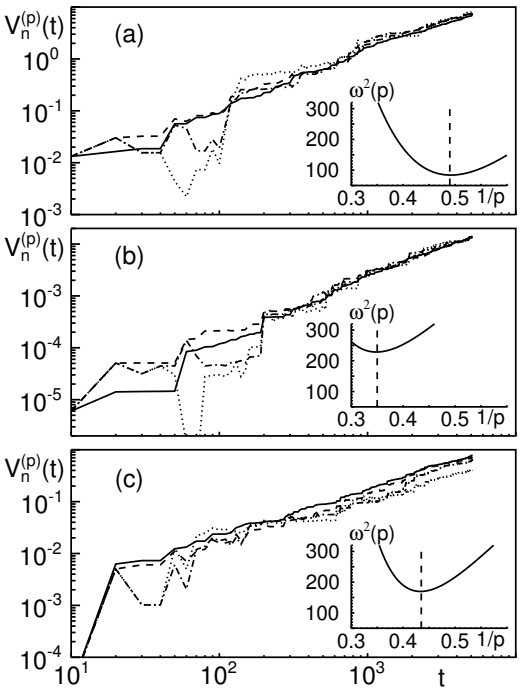

Figure 3.2 Representative course of $V_n^{(p)}(t)$ at $p_{\min}$ ($n = 6 \cdots 9$, shown as dotted, dash-dotted, dashed, and full lines, respectively) for (a) normal diffusion, (b) FBM ($H = 0.35$), and (c) OD ($f = 0.39$). A good collapse of the curves with increasing n is visible in all cases. Insets: The corresponding values for ω^2 as a function of $1/p$ show a clear minimum from which the anomaly $\alpha_{\mathrm{P}} = 2/p_{\min}$ can be determined.

Diffusion anomaly from p variation

We next asked whether the recently introduced p variation method also can be used to reliably extract α. So far, applying the p variation has relied on using an estimate for α from another source (e.g. from a MSD fit). On this basis, it has been judged whether different orders of $V_n^{(p)}(t)$ converge or diverge. This approach allows one to distinguish random walks with stationary increments from those with non-stationary increments [77]. Here, in contrast, p variation alone shall provide α by scanning for the particular value $p_{\min}$ for which the $V_n^{(p)}(t)$ converge to a single master curve (cf. Section 3.1.2). Furthermore, we extend here the use of this method from FBM to OD.

In Equation (3.6) we defined a measure ω^2 for the deviation between different orders of $V_n^{(p)}(t)$. Examples of the p variation for normal diffusion and subdiffusion (FBM and OD) at $p = p_{\min}$ are shown in Figure 3.2. While the lower orders $n = 5, 6$ typically suffer from discretization artifacts (stepwise increase of $V_n^{(p)}(t)$), higher orders ($n = 7, 8, 9$) yield a smooth curve of $V_n^{(p)}(t)$. Owing to this observation, the analysis was restricted to $n \geq 7$ unless stated otherwise.

As can be seen from Figure 3.2, ω^2 is indeed a useful measure to determine the diffusion anomaly without prior knowledge: Clear minima in ω^2 emerged for all three examples, from which α could be determined reliably. The collapse of $V_n^{(p)}(t)$ to a single master curve confirms the goodness of the estimate for the anomaly.

Having confirmed that p variation is a good means to extract the diffusion anomaly

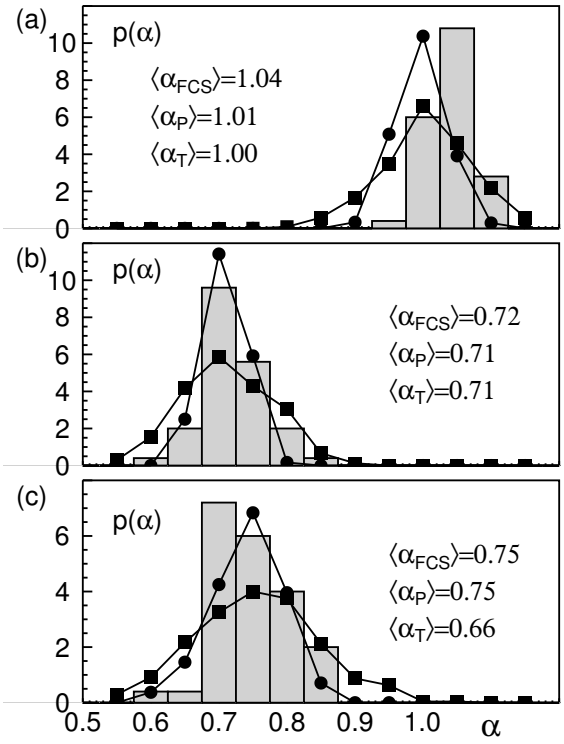

Figure 3.3 Distributions $p(\alpha)$ obtained via FCS ($n = 50$, grey-shaded histogram), $\langle \delta^2 \rangle_{\mathrm{T}}$ ($n = 500$, filled circles), and p variation ($n = 500$, filled squares). The mean anomalies coincide for (a) normal diffusion, (b) FBM ($H = 0.35$), and (c) OD ($f = 0.39$), and also the width of the distributions does not significantly depend on the method or the type of random walk.

even for fairly short trajectories, we next compared the different approaches by which α can be determined from SPT data. To this end, we monitored the distribution of anomalies, $p(\alpha)$, which had previously been used to distinguish CTRW from FBM and OD [24]. In particular, we compared the distributions of anomalies $p(\alpha_{\mathrm{T}})$ and $p(\alpha_{\mathrm{P}})$ and $p(\alpha_{\mathrm{FCS}})$ for FBM and OD.

As a result, we observed that the mean of all distributions and the ensemble-averaged mean α_{E} did not differ significantly (Figure 3.3). Also the width of the distributions did neither show systematic dependencies on the method nor on the type of random walk. Hence, unlike for the case of CTRW, $p(\alpha)$ is not a good means to distinguish the different types of random walks with stationary increments. Also the p variation does not allow for a more detailed discrimination in this respect.

The influence of experimental uncertainties in SPT data

Next, we investigated how experimental uncertainties influence the above described methods. Since uncertainties in FCS experiments have been discussed already extensively elsewhere [23, 47], we restrict ourselves here to SPT.

We have used a moderate yet realistic range of uniformly distributed random shifts, i.e. $s = 0.001 \ldots 0.040$ µm, but also investigated situations with $s = 0.1 \ldots 0.4$ µm, which may be a realistic scenario in SPT experiments with a very high frame rate. For the subsequent considerations we exploited the maximum resolution of our simulated trajectories, i.e. 10^4 steps and $\Delta t = 0.5$ ms. It is convenient to express the blur s

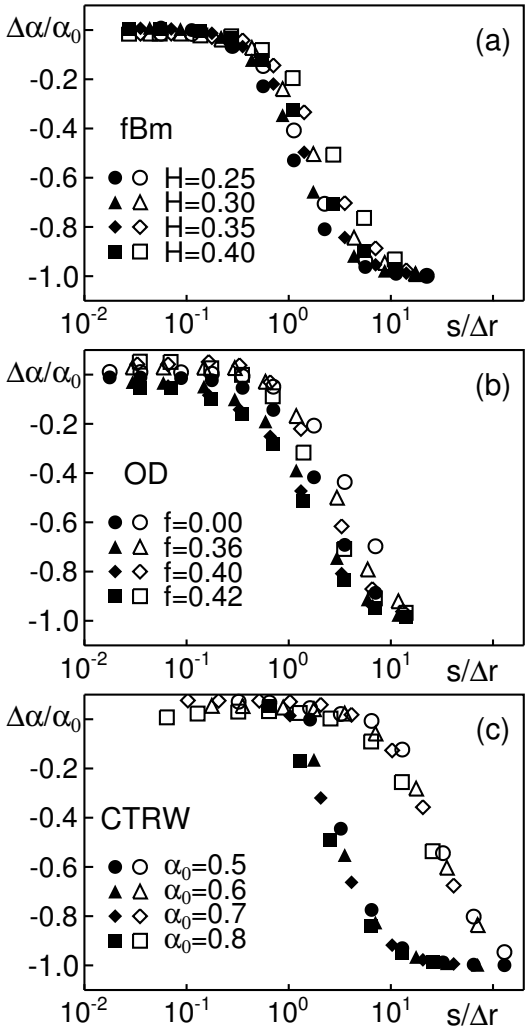

Figure 3.4 Change of the apparent anomaly α for (a) FBM, (b) OD, and (c) CTRW when a positional uncertainty s is added to SPT data. Data from the ensemble- and time-averaged MSDs, i.e. α_E and α_T, are shown with open and full symbols, respectively. For a consistent comparison of all data, the positional uncertainty is expressed in units of the diffusive increment between successive positions, Δr. For an increasing blur of the position, the anomaly decreases with respect to the unperturbed anomaly α_0. For $s/\Delta r \approx 1$ the blurring masks the diffusive motion and the trajectory assumes the form of a Gaussian cloud and hence $\alpha \to 0$.

in units of the (empirically determined) average increment between two successive, non-identical positions, Δr. By this approach, a fair comparison between the different scenarios of subdiffusion is achieved. We quantify the deviation of the measured anomaly in the presence of blur from α_0 for the case $s = 0$ via $\Delta\alpha/\alpha_0 = \alpha/\alpha_0 - 1$. Negative values hence indicate a decreased value of α with respect to α_0.

As a result, we have found that α_E (obtained from the ensemble-averaged MSD) decreases for all scenarios and parameter sets when the positional uncertainty s is increased, Figure 3.4. A major change in α_E is observed when the blur and the typical increment become comparable, i.e. $s/\Delta r \approx 1$. Beyond this point, the appearance of the trajectory is dominated by the blurring which masks the diffusive motion, i.e. the positions look like a Gaussian cloud. In this limiting case, $\alpha \to 0$ as the sequence of particle coordinates becomes completely random and looses the correlation of subsequent time steps inherent to a diffusion process.

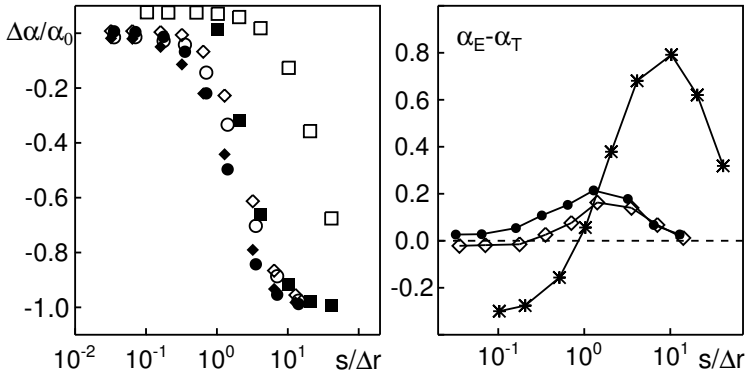

Figure 3.5 (a) Comparison of ensemble- and time-averaged anomalies α_E and α_T (open and filled symbols, respectively) when $\alpha_E \approx 0.7$. Data for FBM ($H = 0.35$, circles), OD ($f = 0.39$, diamonds), and CTRW ($\alpha_0 = 0.7$, squares) are shown. (b)Absolute difference between ensemble- and time-averaged anomaly, $\alpha_E - \alpha_T$, $\alpha_E \approx 0.7$, for FBM ($H = 0.35$; open diamonds), OD ($f = 0.39$; filled circles), and CTRW ($\alpha_0 = 0.70$; asterisks).

For FBM, OD, and CTRW with different α_0 a good but not perfect collapse of the anomaly data for α_E is observed. The same observation holds true for α_T albeit the data for α_E and α_T differ slightly (see also below). While this difference is fairly small for FBM and OD , the difference is very strong for CTRW data. Indeed, due to the previously reported weak ergodicity breaking [57, 58] such a difference in the behavior of α_E and α_T is anticipated. The time-averaged MSD exhibits normal scaling $\alpha_T = 1$, while the ensemble average indicates subdiffusion with $\alpha_E < 1$. Hence, our results suggest that the detection of the anomalous scaling behavior of the ensemble average is less affected by positional uncertainties than measurement of the normal scaling of the time average. Adding an increasing artificial noise to experimentally obtained SPT data therefore can be used as a straightforward test to distinguish CTRW from FBM and OD.

It is worth noting at this point that the p variation method failed already for moderate blurring. No reasonable minimum for ω^2 could be obtained for most of the trajectories. Due to this limitation and the high effort needed to calculate α_P we therefore neglected the p variation method in the further analysis.

When comparing FBM, OD, and CTRW with a similar diffusion anomaly, i.e. $\alpha_E \approx 0.7$, we observed a good collapse of the data for OD and FBM and the time-averaged data for CTRW. The ensemble-averaged anomaly α_E for CTRW however deviated considerably and was much less sensitive to blurring as compared to its time-averaged analogue α_T (Figure 3.5 [a]). Indeed, the difference between time and ensemble average, i.e. $\alpha_E - \alpha_T$ is moderate for all blurs for FBM and OD, but it deviates strongly from zero for CTRW (Figure 3.5 [b]). Especially, when the

uncertainty s is of the size of a typical increment, Δr, the different scaling of the time and ensemble average displacements can no longer be detected since $\alpha_E = \alpha_T$. So, in this case the distinction between CTRW and OD/FBM scenarios by means of measuring ergodicity breaking fails.

At this point, it is instructive to discuss the non-zero values of $\alpha_E - \alpha_T$ for FBM and OD. Usually the ensemble- and time-averaged MSDs are calculated and fitted in different time intervals, as for the time average the one or two upper decades in time have to be omitted due to poor statistics. Hence, the time-averaged MSD relies on smaller displacements than the ensemble-averaged MSD and hence both are differentially affected by the blurring. For the data presented in Figure 3.5, for example, the fitting range $\tau = 5 \times 10^{-4} \ldots 5 \times 10^{-2}$ s was used for the time average and $t = 5 \times 10^{-4} \ldots 5 \times 10^{-1}$ s for the ensemble average. Still, the deviation of both anomalies is moderate and well separable from the strong effect found for CTRW by using the same fitting ranges.

3.1.4 Summary and Conclusions

In summary, we find that blurring of particle positions generally leads to an underestimation of the anomaly coefficient α, i.e. the diffusion appears more anomalous. For moderate blurs s, one can still determine a reasonable anomaly which is, however, smaller than the actual value of the diffusion process. Hence, when determining α in SPT experiments, an adequate trade-off has to be found: On the one hand the increments between subsequent measurements should be larger than the anticipated uncertainty of the particle position. On the other hand the subdiffusion process under investigation may be transient, so the recording frame rate should be fast enough to cover the relevant time scale. Our simulations show that, if the uncertainty is of the order of the average increment, α drops by almost 40%. Moreover, if CTRW is the underlying process, a different scaling of time and ensemble average MSD that indicates ergodicity breaking may no longer be detected in this case.

We have also shown that the p variation method can be used to extract the diffusion anomaly. Unfortunately, it reacts quite sensebly to the blurring of trajectories. Already at moderate uncertainties it becomes difficult to estimate the anomaly and draw reliable conclusions about the underlying mechanism. Furthermore it does not provide a means to distinguish between the two ergodic processes OD and FBM. Still it resembles a valuable analysis tool for (high-quality) SPT data if a distinction between processes with stationary and those with non-stationary increments has to be made.

3.2 The Shape of Subdiffusive Trajectories

3.2.1 Introduction

Subdiffusion of tracers in crowded media is a frequently observed phenomenon, cf. Section 1.3.3. Despite large efforts in recent years, the mechanism that under-

lies crowding-induced subdiffusion has remained widely elusive so far. The most prominent models for subdiffusion are continuous time random walks (CTRW) [20], fractional Brownian motion (FBM) [60], and diffusion on fractal supports (obstructed diffusion, OD) [68], cf. Section 1.3.4. All of these models give rise to a sublinear scaling of the mean square displacement (MSD) with time $\langle \delta^2 \rangle \propto t^\alpha$ but they rely on quite different concepts.

On the one hand, techniques that allow to judge whether experimental data comply with a CTRW or not are well established. They exploit, e.g. the distribution of anomalies [24], (weak) ergodicity breaking [57, 58], or the p variation of tracer trajectories [77], cf. 3.1. On the other hand, the distinction between OD and FBM is difficult. In this respect, the velocity autocorrelation function has been proposed as a criterion [107]. Furthermore the statistics of the maximum excursion combined with a growing sphere analysis can yield the relevant information [78]. In all, it appears that a conclusive statement about the subdiffusion mechanism requires an involved analysis of high-quality SPT data [81]. Along this line, a recent study reports on subdiffusion of lipid granules through the cytoplasm of yeast cells that complies to a CTRW with a finite cut-off in the waiting time distribution on short time scales and FBM on longer time scales [79].

Here, we propose a conceptually simple criterion to distinguish between different models for subdiffusion that exploits the average shape of tracer trajectories [33]. For simulated trajectories we find that CTRW, FBM, and OD imply different correlations between α and the average trajectory shape as quantified by the *asphericity* (see below). Hence, this approach could in principle allow for a robust determination of the most appropriate model. One possible pitfall arises from the measurement uncertainties inherent to SPT data, cf. Section 1.3.2. In the last section it has been shown that measurement errors on the particle position lead to an underestimated anomaly α. Analogously, blurred trajectories are expected to have a more spherical shape. Hence, we also considered the scenario that we call "apparent subdiffusion" (ASD), where normal diffusive trajectories ($\alpha = 1$) are artificially blurred to mimic measurement uncertainties (cf. Section 3.1).

To verify our method we analyze high-quality SPT trajectories recorded by the group of Prof. Dr. Jürgen Köhler at the University of Bayreuth. As a model system for a tracer immersed in a crowded fluid, diffusion of a 20 nm bead in dense dextran solutions is studied. In the accessible time-regime diffusion is essentially normal and accordingly the average shape and diffusion anomaly of the trajectories show only small deviations from the random walk values.

Quantification of Trajectory Shapes: Asphericity

The *asphericity* provides a simple measure for the shape of fractal objects in general and random walks in particular [126]. Let the object under consideration be defined

by a set of N points with coordinates $\mathbf{x}_1 \dots \mathbf{x}_N$. The *gyration tensor* reads [127]

$$T_{ij} = \frac{1}{N} \sum_{n=1}^{N} (x_{ni} - \langle x_i \rangle)(x_{nj} - \langle x_j \rangle) \,. \tag{3.7}$$

Thus, $\mathbb{T}$ describes the geometrical arrangement with respect to the *center of mass*

$$\langle \mathbf{x} \rangle = \frac{1}{N} \sum_{n=1}^{N} \mathbf{x}_n \,. \tag{3.8}$$

Comprising a symmetric matrix, $\mathbb{T}$ can be transfered to diagonal form. Its eigenvectors resemble the *principal axes of gyration* and the corresponding eigenvalues R_i the *principal components of the radius of gyration*. Then, the asphericity A of a d-dimensional object is

$$A = \frac{\sum_{i>j}^{d} \left\langle (R_i^2 - R_j^2)^2 \right\rangle}{(d-1) \left\langle \left(\sum_{i=1}^{d} R_i^2 \right)^2 \right\rangle} \,. \tag{3.9}$$

A involves averaging over the ensemble of walks as indicated by $\langle \cdot \rangle$. The limiting cases $A = 0$ and $A = 1$ resemble a perfectly spherical and an extended rod-like shape, respectively. For an unbiased random walk an analytic value is available [128, 129]:

$$A = \frac{2(d+2)}{5d+4} \;\Rightarrow A = \frac{4}{7} \quad \text{for} \quad d = 2 \,. \tag{3.10}$$

Thus, the average shape of a two-dimensional random walk differs drastically from a circle and is fairly elongated. As an alternative, the asphericity may also be calculated individually for each trajectory of the ensemble:

$$A_i = \frac{\sum_{i<j}^{d} (R_i^2 - R_j^2)^2}{\left(\sum_{i}^{d} R_i^2 \right)^2} \,. \tag{3.11}$$

In this case, no analytic value for the average $\langle A_i \rangle$ is known [126] and hence it has to be computed from simulated walks. The individual values A_i allow for an extended analysis of the distribution of asphericities.

3.2.2 Parameters, Setup, and Analysis

Calculation of Theory Curves

In the following, we compare the shape of experimental trajectories with theoretical predictions derived from simulated trajectories of FBM and OD in two dimensions (2D). To this end, OD samples were generated by the corresponding variants of the

LGA algorithm, cf. Section 2.2.2. For FBM we applied the circulant method, see Section 2.2.3. For the special case $H = 0.5$ the Brownian dynamics algorithm was chosen, cf. Section 2.1.2. With the data from an independent method the consistency of the simulations was checked.

To obtain solid statistics, a large ensemble of 10^6 trajectories was created for every parameter set. We fixed the trajectory length $N = 2^{13} = 8192$ for FBM. The OD scenario required some additional considerations: Since subdiffusion is transient below the percolation threshold (see [71] and Section 1.3.4) we systematically varied N in a wide range to study the influence on the shape and diffusion anomaly α. Furthermore, for large obstacle densities f, the obstacles may constrain the tracer to a tiny set of lattice sites. We identified and removed such "trapped" trajectories from the analysis. In total, their number was low compared to the number of simulated walks, even for large f (e.g. $f = 0.42$ and $N = 5000$ yielded less than 5% trapped walks). Nevertheless, we generated a set of 1.5×10^6 trajectories per value of f to assure strong statistics. To reduce the repetitive sampling of identical paths we generated a new random environment in every 1000th run. In two dimensions the site percolation threshold for vacant sites is $f_p = 1 - 0.59274 = 0.40726$ [72]. We varied f between 0.33 and 0.42 in order to cover the sub- and supercritical behavior. Owing to the finite system size of 350×350 lattice sites, the threshold was rather situated at $f \approx 0.39$.

3.2.3 Simulations

Fractional Brownian Motion (FBM)

Figure 3.6 presents the calculated asphericity in dependence on the Hurst parameter for two-dimensional trajectories. We extended the analysis beyond subdiffusion ($H < 0.5$) to superdiffusion ($H > 0.5$) because, to our knowledge, there is no comprehensive study on the shape of FBM trajectories, yet. Naively, one would expect, that in the limit $H \to 0$ also $(A|\langle A_i \rangle) \to 0$ as the trajectories shrink effectively to points. The opposite scenario $H \to 1$ corresponds to ballistic motion, i.e. particles follow a linear path and consequently $(A|\langle A_i \rangle) \to 1$. Indeed, our simulations showed for both definitions of the asphericity, Equation (3.9) and Equation (3.11), the same tendency, namely a monotonous increase with H between the two extremes.

We found that for the relevant subdiffusive regime ($0.2 < H < 0.5$) $A(H)$ can be described by a simple linear relationship, see Figure 3.6 (a):

$$(0.2 < H < 0.5) \quad A = (1.25 \pm 0.02)H - (0.049 \pm 0.006)\,. \tag{3.12}$$

Here, the determined slope would result in $A = 1$ already at $H \approx 0.84$. Indeed, in the superdiffusive regime the data revealed slightly different parameters:

$$(H > 0.7) \quad A = (0.80 \pm 0.01)H - (0.210 \pm 0.009)\,. \tag{3.13}$$

As can be judged from the figure, the linear approximations describe the data very accurately in the respective regimes. Moreover, the expected values in the limits

$H \to 0$ and $H \to 1$ were captured with good precision. Even more importantly, the linear interpolation for $H < 0.55$ predicted the analytically known asphericity of the random walk (4/7, cf. [126]) at $H \approx 0.5$. The data point at $H = 0.5$ has been generated with the Brownian dynamics algorithm (cf. Section 3.2.2) and complied well with the FBM data.

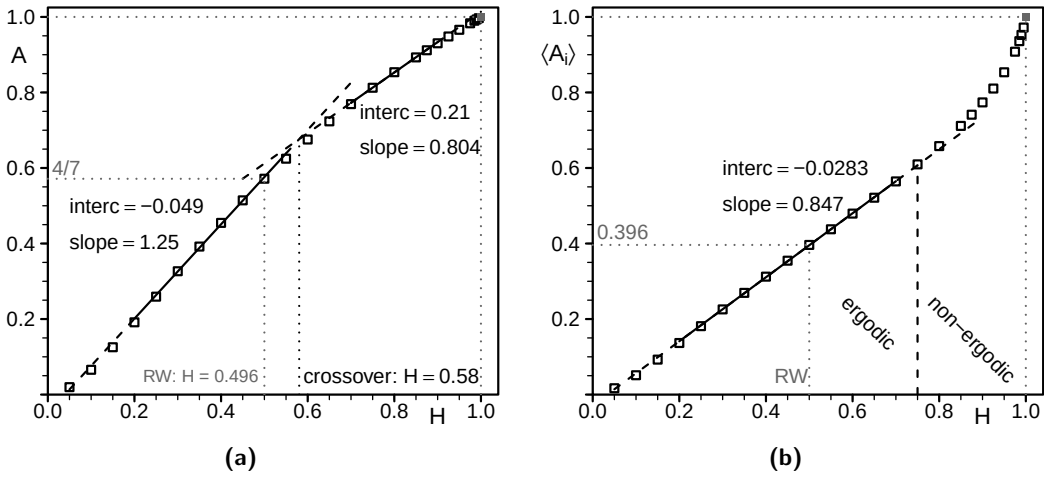

Figure 3.6 (a) Dependence of the asphericity A as calculated via Equation (3.9) in dependence on the Hurst exponent. Two regimes can be distinguished in which $A(H)$ is well approximated by slightly different linear functions (solid lines), cf. Equation (3.12) and Equation (3.13). The extrapolated values for $H \to 0$ and $H \to 1$ coincide with the expectations. Moreover the analytical value for the random walk ($H = 0.5$) is obtained with good precision. (b) Dependence of the alternative asphericity measure $\langle A_i \rangle$, Equation (3.11), on the Hurst exponent. A single linear function describes the data well, even for superdiffusive FBM, cf. Equation (3.14). At approximately $H = 3/4$ where a transition between ergodic and non-ergodic behavior has been localized (cf. [64]) the slope increases strongly.

The alternative measure for the asphericity, $\langle A_i \rangle$, showed a somewhat different behavior. The data were well described by a unique linear relationship for a large interval of H values, cf. Figure 3.6 (b):

$$(0.2 < H < 0.7) \quad \langle A_i \rangle = (0.847 \pm 0.003)H - (-0.028 \pm 0.002)\,. \tag{3.14}$$

If interpolated to the limit $H \to 1$, this would yield $\langle A_i \rangle (H \to 1) \approx 0.819$ rather than unity. Again, a crossover to a different, strongly enhanced slope of the data could be observed. Intriguingly, we localized this crossover close to $H = 3/4$ that has been associated with a transition to ergodicity breaking behavior of FBM [64]. In all, the linear approximation works very well for the subdiffusive case. Since no

analytic value for $\langle A_i \rangle$ exists we extracted it from our Brownian dynamics simulations: $\langle A_i \rangle (H = 0.5) \approx 0.396$ which is well captured by the FBM simulations.

In summary, the shape of FBM trajectories gradually changes with H from the perfectly spherical ($A = 0$) to the fully stretched ($A = 1$) conformation. Partly, the increase can be described by a simple proportionality. For the following discussions we focus on the subdiffusive and diffusive scenarios, i.e. we rely on the linear approximations Equation (3.12) and Equation (3.14) as theoretical predictions.

Obstructed Diffusion (OD)

Below the percolation threshold ($f < f_p$) the shape of OD trajectories should not deviate from that of a random walk on long time scales, when the local fractality of the environment averages out. At f_p the percolating cluster exhibits self-similarity on all scales. Thus, like the diffusion anomaly (cf. Section 1.3.4), the asphericity should be independent of the trajectory length N. Finally, above f_p the vacant sites constitute confined clusters that strongly obstruct the tracers' motion. In this limit, a decreased asphericity may be anticipated. Generally, since for $f < f_p$ there is an upper limit for self-similarity, all observed phenomena have to be tested with respect to N.

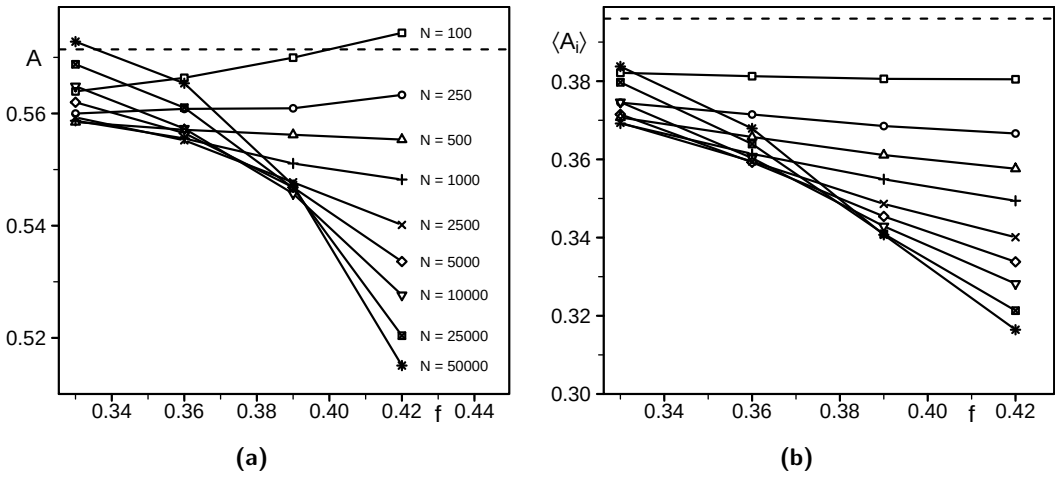

Figure 3.7 (a) Course of the asphericity A as calculated via Equation (3.9) in dependence on the occupied volume fraction f. At the percolation transition the data for moderate trajectory lengths N intersect close to a single point ($f \approx 0.39$,$A \approx 0.548$). (b) The alternative asphericity measure $\langle A_i \rangle$, Equation (3.11), with symbols like in (a). Also the longest trajectories do not reach the calculated value for a random walk at $f = 0.33$ ($\langle A_i \rangle = 0.396$). Furthermore the intersection of different N is not as clear as in case of A.

In Figure 3.7 we present the course of the two asphericity measures A and $\langle A_i \rangle$.

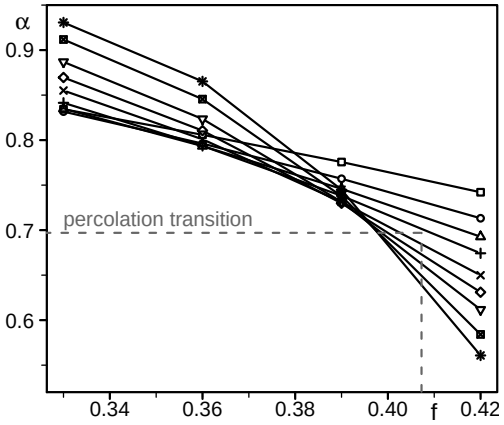

Figure 3.8 Course of the diffusion anomaly α as determined for trajectories of varying length (symbols as in Figure 3.7 [a]). As expected for a finite size analysis at a critical point the data intersect close to a single point that marks the percolation transition. The detected transition point somewhat deviates from the literature value (indicated by the gray, broken lines) due to the finite size of the lattice.

Indeed, we found that the outlined expectations were met. Very short trajectories ($N < 500$) showed a slight increase with f indicating that the trajectories became more extended. This effect most probably resembles a finite-size artifact: The tracers can only make a small number of steps when most of the proposed moves would lead to an overlap with obstacles. In the following we hence focus on $N \geq 500$: For $f = 0.33$ A increased with growing trajectory length and approached the random walk value (4/7) for the largest N studied, see Figure 3.7 (a). Hence, for $N = 2.5 \times 10^4$ the local fractality of the support averaged out completely and the trajectories resembled random walks. At $f \approx 0.39$ the data intersected near to a single point with $A \approx 0.548$. This marks the percolation transition in our finite system. Like the diffusion anomaly, the asphericity A takes a scale-independent value at the threshold. Above f_p, the longer trajectories experienced strong confinement in the finite clusters of vacant sites and their shape became more spherical. Analogously a decreasing α is found in this regime where free subdiffusion crosses over to confined diffusion ($\alpha \to 0$ for $N \to \infty$).

The alternative asphericity measure $\langle A_i \rangle$ yielded a similar but slightly different picture, see Figure 3.7 (b). Again, the short trajectories were omitted from the finite size analysis. For $N \geq 500$, the data intersected but not as clearly as for A. Furthermore, no scenario comes close to the asphericity of a random walk (0.396) even at low occupied volume fraction. Thus, the influence of an initially more spherical shape diminishes not as fast as in case of A. This means, while A captures the large-scale shape of the trajectories, $\langle A_i \rangle$ is still strongly affected by the short-time behavior.

As a complement to the asphericity data the course of the diffusion anomaly α with f is shown in Figure 3.8. The intersection of the data at the percolation threshold is clearly visible. For comparison the literature values (corresponding to an infinite system, $L \to \infty$) are indicated by gray, broken lines. In our finite system we found the transition situated at $\alpha \approx 0.72$ and $f \approx 0.39$.

To compare our simulations to experimental data we eliminated f by merging $\alpha(f)$ and $A(f)$ from the simulations to a pair (α,A) that can also be obtained from

SPT measurements. Figure 3.9 (a) depicts the results for three different trajectory lengths. Analogously to the FBM scenario, we detected an increase of A with α and rationalized this behavior by an approximative linear dependence $A \propto \alpha$. In the plot, the corresponding fit for the representative case $N = 5000$ is given:

$$(0.33 < f < 0.42;\, N = 5000) \quad A = (0.120 \pm 0.006)\alpha - (0.458 \pm 0.004)\,. \qquad (3.15)$$

The linear approximation performed worse than for FBM but still quite accurately. Although, the determined slope increased with growing N, the data for the longest trajectory, $N = 2.5 \times 10^4$, showed that the typical range of A stayed well above the FBM data. We consequently chose $N = 5000$ as a representative example and used Equation (3.15) as theoretical prediction.

In part (b) of Figure 3.9 the pairs $(\alpha,\langle A_i\rangle)$ are plotted for three trajectory lengths. It has been discussed that $\langle A_i\rangle$ is strongly influenced by the shape on short time scales. Hence varying N has a weaker effect than in case of A. Again, a simple linear fit provides a reasonable approximation of the data. For the example $N = 5000$ (solid line in the plot) we found

$$(0.33 < f < 0.42;\, N = 5000) \quad \langle A_i\rangle = (0.157 \pm 0.014)\alpha - (0.233 \pm 0.011)\,. \quad (3.16)$$

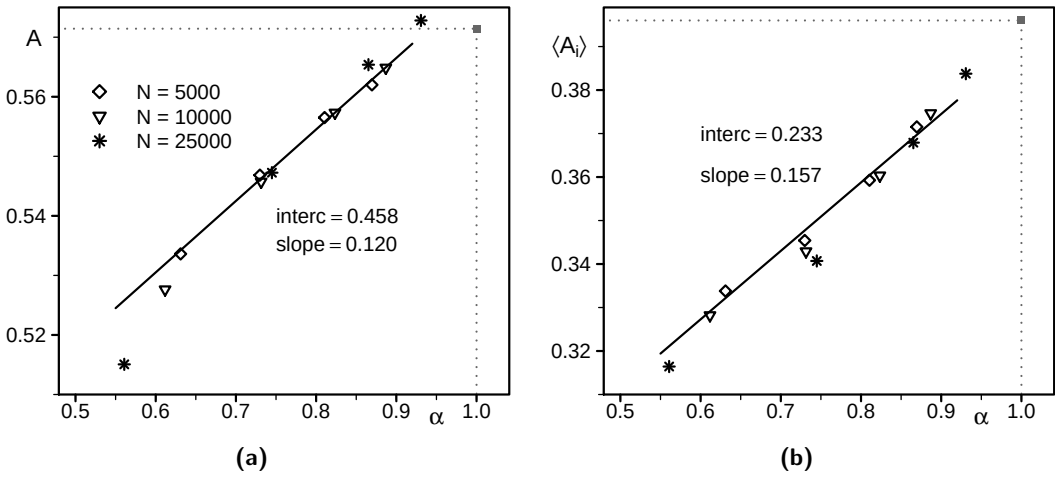

Figure 3.9 (a) The determined pairs (α, A) from OD simulations for three different trajectory lengths. Like for FBM we rationalize the data by approximating $A \propto \alpha$ (fit shown for $N = 5000$, solid line). The approximation performs worse as compared to FBM and the slope varies only slightly with N. (b) The same plot for the alternative asphericity measure $\langle A_i\rangle$. Again a linear fit is shown as an approximation for $N = 5000$. Since $\langle A_i\rangle$ has a stronger memory with respect to short time scales, varying N has a much weaker effect than in case of A.

Continuous Time Random Walk (CTRW)

The CTRW scenario does not require additional considerations as it resembles a random walk with stochastic sojourn times. Hence the geometrical appearance of CTRW trajectories is that of a regular random walk and thus $A = 4/7$ and $\langle A_i \rangle = 0.396$. To obtain these results, however, all "apparent stops" have to be removed from the sample trajectories. That is, the full walk has to be reduced to the series of successively distinct coordinates. For simulations it is straight-forward to check whether $\mathbf{x}(t) = \mathbf{x}(t + \Delta t)$ but for experimental data this criterion has to be adjusted, since the position of the tracer is only known within the limits given by the measurement uncertainties.

The Impact of Position Uncertainties

In the analysis of SPT experiments one faces unavoidable measurement errors that may provoke wrong interpretations of the data, cf. [26, 27] and Section 3.1. Hence, we studied the impact of Gaussian blur on the apparent shape of normal diffusive trajectories by applying the method described in Section 3.1. The standard deviations of the blur $\mathbf{s} = (s_x, s_y)$ were varied in the range $0.5 \ldots 50\,\Delta r$, where Δr denotes the mean increment between two successive measurements. As discussed in Section 3.1, a substantial blur of the particle position leads to an underestimation of α obtained by fitting to the MSD. As s increases well above the size of a typical positional increment, $\alpha \to 0$. Accordingly, one anticipates $(A|\langle A_i \rangle) \to 0$, since the resulting "Gaussian cloud" of coordinates resembles an isotropic, spherical object.

Figure 3.10 shows the courses of $A(\alpha)$ and $\langle A_i \rangle(\alpha)$ for blurred trajectories with varying length N. The apparent diffusion anomaly α was determined from a fit to the (ensemble-averaged) MSD in the range $t = 30 \ldots N\,\Delta t$. The limits of an undisturbed trajectory and a Gaussian cloud were clearly visible. The transient increase in between depended on N: For longer trajectories the transition set in already at small anomalies indicting that the blurring averaged out. Close to $(A = 4/7; \alpha = 1)$ the course of $A(\alpha)$ is evocative of the curve for FBM, cf. Figure 3.6. Hence, wrongly interpreting a blurred, normal diffusive trajectory as being subdiffusive FBM is a probable pitfall when relying on the pair (A, α) to determine the diffusion mechanism. Consequently, an additional scenario of "apparent subdiffusion" (ASD) caused by measurement errors should be added to any comparison between experimental data and theory. In cases where positional blur and FBM can explain the data, further criteria have to be checked to discriminate between them. For example, the increments of a FBM time series show anti-correlation whereas they are mutually independent for a sequence of blurred points.

3.2.4 Comparison to Experiments

In collaboration with the group of Prof. Dr. Jürgen Köhler, Chair for Experimental Physics IV, University of Bayreuth, we applied our analysis method to high-resolution SPT data recorded in an advanced circulating focus setup, cf. Section 1.3.2. The

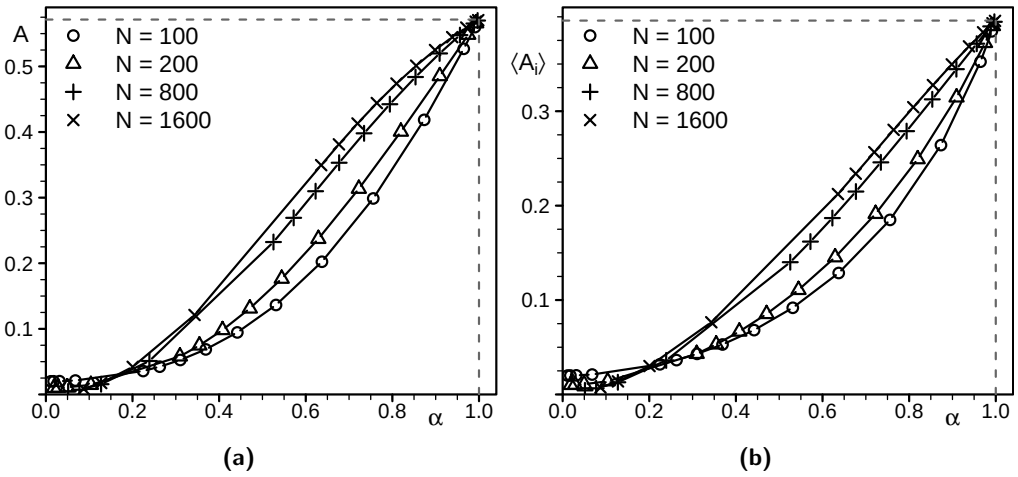

Figure 3.10 The two asphericity measures A (a) and $\langle A_i \rangle$ (b) in dependence on the apparent diffusion anomaly measured for blurred trajectories. The standard deviation of the Gaussian blur was varied in the range $0.5 \ldots 50\,\Delta r$ where Δr corresponds to the average positional increment between two snapshots. The transition between an undisturbed trajectory ($A = 4/7; \alpha = 1$) and a Gaussian cloud ($A = 0; \alpha = 0$) depends on the trajectory length N.

experiments were prepared and conducted by Dominique Ernst. A solution of 500 kDa dextran at a concentration of 30% per weight served as a prototypic crowded bulk fluid. Nano-particles of 20 nm diameter were tracked in two dimensions for up to 10^3 s at a temporal resolution of 4 ms. In the following, the term "experiment" refers to the full path of a single tracked particle. To increase the statistical basis we split each experiment into pieces of $3000\,\Delta t$ (12 s) that we call "trajectories".

For each experiment, we computed the ensemble average MSD $\langle \delta^2 \rangle_\mathrm{E}$ over its trajectories to obtain α_E. For the trajectories the principal axes of gyration, R_1 and R_2, were computed by diagonalizing the corresponding gyration tensor. From that A_i ($\langle A_i \rangle$) and A followed via Equation (3.9) and Equation (3.11). Analytic values for the standard errors of α_E and A are difficult to obtain since they arise from non-trivial calculations on the ensemble average. To approximate the standard errors we hence applied the bootstrap method (see, e.g. [130]): The sample $\Theta = \{\theta_1, \theta_2, \ldots, \theta_n\}$ consists of n trajectories that have been extracted from one or more experiments. From that a *bootstrap sample* $\Theta_B = \{b_1, b_2, \ldots, b_n\}$ is generated, where the $b_i \in \Theta$ have been chosen by randomly sampling among the trajectories in Θ with replacement. We calculated A and $\langle \delta^2 \rangle_\mathrm{E}$ for 200 bootstrap samples Θ_B to obtain distributions of values. The standard deviations of α_E and A provided estimates for the respective standard errors.

According to the considerations in [27] and Section 3.1 the inherent uncertainties of SPT measurements lead to an underestimation of the diffusion anomaly. Hence,

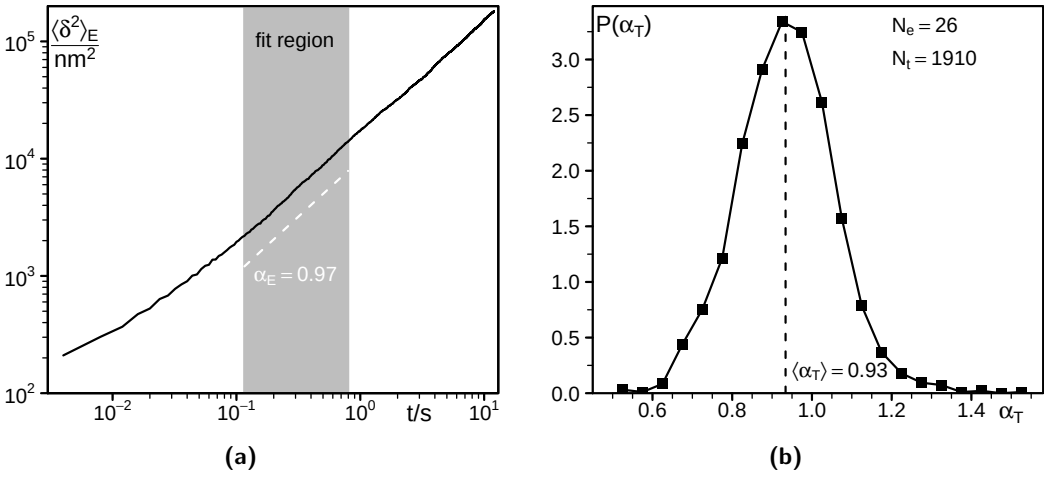

Figure 3.11 (a) The ensemble-averaged MSD of a 20 nm-bead in a dense dextran solution (500 kDa-dextran at 30% per weight). Due to inherent measurement uncertainties, the short time behavior does not yield reliable estimates for α. The used fit region as indicated by the gray area yielded an anomaly close to unity. (b) The distribution of time-averaged anomalies from all 1910 trajectories.

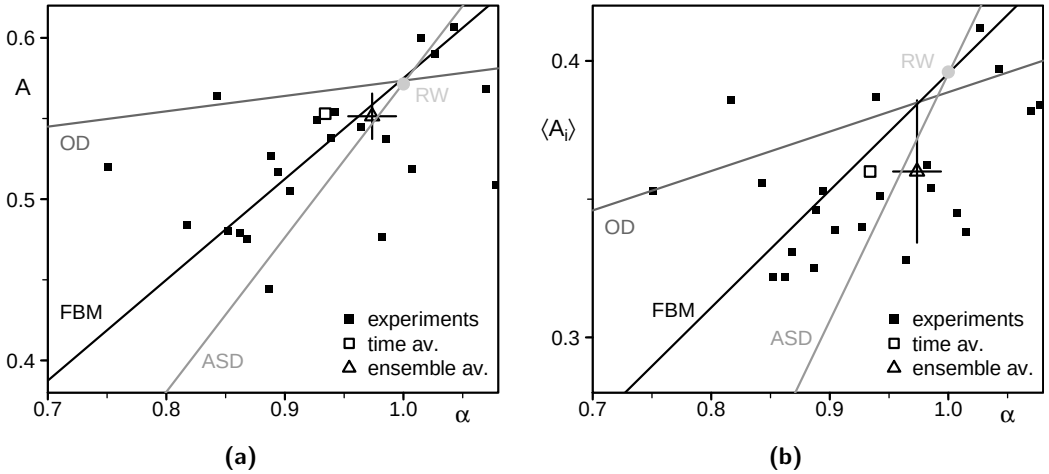

Figure 3.12 The experimentally obtained pairs (A,α) (a) and $(\langle A_i\rangle,\alpha)$ (b) in comparison to theoretical predictions. The ensemble average α_{E} (triangle) is taken over all $N_t = 1910$ trajectories of all experiments. In (a) the error bars give the standard errors on α and A as obtained by bootstrapping (see text for details); The open square symbols indicate the time-averaged diffusion anomaly α_{T}. Furthermore, to illustrate the scatter of the data, the filled squares mark the positions of the $(A|\langle A_i\rangle, \alpha_{\mathrm{E}})$ pairs for each of the $N_e = 26$ experiments.

a lower limit $t_{\min}$ for reliable fits to the MSD has been determined. Here, the microscopy setup called for $t_{\min} \approx 100$ ms and the fit region was consequently set to $120 \ldots 800$ ms, cf. Figure 3.11 (a). For this regime we detected a diffusion anomaly close to unity ($\alpha_{\mathrm{E}} = 0.97$). The broad distribution of time-averaged anomalies α_{T} in Figure 3.11 (b) revealed a slightly lower value ($\langle \alpha_{\mathrm{T}} \rangle = 0.93$). In contrast, dense solutions of heavy dextrans have been reported to bear tracer subdiffusion with $\alpha \approx 0.82$ on the time scales of FCS ($0.1 \ldots 200$ ms) [24]. Apparently, the crossover to normal diffusion happens on the ms-scale where the SPT data are still impaired by errors on the particles' positions.

Figure 3.12 compares the measured pairs (A, α) and $(\langle A_i \rangle, \alpha)$ with the theoretical expectations that have been calculated above. To give an impression of the scatter not only the full ensemble average but also the individual values for all 26 experiments are shown. In accordance with a diffusion anomaly close to unity the average shape is only slightly more spherical than that of a random walk. Indeed the pair of values complied to a random walk within the interval of two standard errors. Since the theoretical curves meet in the point ($A = 4/7$,$\alpha = 1$) for a random walk no clear distinction between the different subdiffusion models was possible.

3.2.5 Summary and Conclusions

In this section we analyzed the shape of trajectories that were generated according to different subdiffusion models. In all cases a correlation between the diffusion anomaly α and the asphericitiy measures A and $\langle A_i \rangle$ were identified. Since the slope depends on the model one can compare the experimentally obtained pairs $(A|\langle A_i \rangle,\alpha)$ with theory to identify the underlying mechanism of subdiffusion.

We applied this method to high-quality SPT trajectories of tracers in dense dextran solutions. Due to the limited measurement accuracy only the long term normal diffusive behavior could be covered. Indeed the results differed weakly from a random walk indicating that the method provides reasonable pairs of anomaly and asphericities. It will be interesting to test the presented approach on a system where subdiffusion prevails up to the second-scale, e.g. concentrated lysozyme solutions [44]. Moreover, as SPT technologies get constantly improved, tracking of small particles in the cytoplasm of a living cell can become tractable, soon. Then the proposed method could help to elucidate the random process behind subdiffusion in biological environments.

3.3 Polydisperse Brownian Dynamics

3.3.1 Introduction

Subdiffusion of tracers in crowded fluids is a frequent observation, cf. Section 1.3.3. The experimental literature mentions manifold situations ranging from colloidal tracers in dense polymer solutions to labeled proteins in the cytoplasm. So far, these varying observations could not be rationalized by a generic model. The difficulties

originate from the variety of tracer-crowder combinations and the different time scales that are accessible by the respective measurement technique.

In this context, computational models may serve as well defined and easy controlable reference systems. Here, we extend an earlier particle-based model of a crowded cytoplasm [25]: Spherical Brownian particles with a realistic size distribution resemble the proteins. They interact as soft spheres with an unspecific inter-particle attraction at intermediate separations as described in Section 2.1.2. In contrast to the widely used hard sphere model with strict volume exclusion (cf. Section 2.1.2) soft spheres allow for much longer integration and overall simulation times. The pronounced polydispersity is a prominent feature of the cytoplasm, where a large number of different proteins sustains the various life-relevant biochemical processes. Finally, the unspecific attractive interaction accounts for the impact of transient binding, e.g. by "solvation forces" [44], without the detailed knowledge about the particular bond configuration between any two proteins. In all, the model is based on realistic particle sizes and time scales to investigate diffusion on time scales that are accessible by FCS and SPT. On the other hand, the approach is rather generic, in that it identifies the minimum requirements for a complex fluid to bear subdiffusion.

As a result, we find that purely repulsive spheres do not yield anomalous subdiffusion but slowed Brownian motion on experimental time scales ($1 \ldots 10$ ms and above). This is in accord with the literature and especially complies to hard-sphere simulations, see e.g. [104, 105, 131]. The effects of polydispersity are marginal – at least for the studied range of bead radii. Also a weak, attractive interaction did not change the overall behavior. As the attractive interaction becomes stronger, particles start to condense into a cluster phase. Consequently, they behave like a system with an increased concentration, i.e. they diffuse normally but are strongly slowed down. Anomalous diffusion arises on experimentally accessible time scales when the system starts from a well-mixed configuration and evolves towards a cluster phase. In a rather different scenario, a substantial fraction of particles is turned to immobile obstacles that consequently leave a random, porous medium for the remaining tracers. The result is subdiffusion on experimental time scales as expected for an OD setting, cf. Section 1.3.4.

3.3.2 Parameters and Setup

From earlier studies [25] we take the finding that the masses m of proteins contained in *HeLa* cells approximately follow a Poissonian (exponential) distribution

$$p(m) = \frac{1}{\langle m \rangle} \exp\left(\frac{-m}{\langle m \rangle}\right). \tag{3.17}$$

For the mean mass $\langle m \rangle = 350$ kDa is a reasonable choice. When setting up the simulation box, masses were drawn according to the distribution Equation (3.17). From that, the bead radii R_i were calculated by the empiric formula

$$R_i = \left(\frac{8 m_i}{50}\right)^{\frac{1}{3}}, \tag{3.18}$$

Parameter	Simulation units	Conversion
D	$0.02\ \mathrm{nm}^2/\mathrm{ns}$	$20\ \mu\mathrm{m}^2/\mathrm{s}$
m	$1.66054 \times 10^{-27}\ \mathrm{kg}$	1 kDa
η	$10^{-21}\ \mathrm{kg\,nm^{-1}\,ns^{-1}}$	1 mPa s
ρ	$1.38 \times 10^{-24}\ \mathrm{kg/nm}^3$	$1.38\ \mathrm{kg/dm}^3$
A	$6\pi\eta \times 10^3\ \mu\mathrm{m}^2/\mathrm{s}$	18.85 pN
B	$k_\mathrm{B}T\ \ \mathrm{nm}^{-1} = 4.28 \times 10^{-21}\ \mathrm{J/nm}$	4.28 pN
E	$k_\mathrm{B}T = 1.38 \times 10^{-23}\ \mathrm{J/K} \times 310\ \mathrm{K}$	0.027 eV

Table 3.2 The important parameters of the BD algorithm. The middle column gives their values in units used in the simulations, the right column shows conversions to more commonly used units.

where m_i is measured in kDa. Cut-offs at $\min(R) = 2$ nm and $\max(R) = 5.5$ nm restricted the radii to a tractable range. To categorize the simulation results with respect to polydispersity the beads were distributed into four size classes with N_k particles of mean radius $\overline{R}_k$, see Figure 3.13. Ensemble-averaged quantities like the MSD were calculated separately for each size. According to the Einstein-Stokes relation the bead radius determines the bulk self-diffusion coefficient [Equation (1.12)]

$$D_0 = \frac{k_\mathrm{B}T}{6\pi\eta R}\,, \tag{3.19}$$

where the viscosity η is that of water (1 cP). Throughout the simulations, lengths are measured in units of 1 nm, and the lowest time scale is defined by the integration time $\Delta t = 1$ ns. Thermal energy $k_\mathrm{B}T$ at the physiological temperature (310 K) gives the unit of energy. The values of the simulation parameters are summarized in Table 3.2.

Initial positions of the beads in the simulation box were chosen randomly, hence substantial overlaps could occur especially for high concentrations. Such a configuration does, in general, not correspond to thermal equilibrium with respect to the implemented interactions. Consequently, at the beginning of every simulation run, the particles were moved for T_{eq} time steps without recording any data. For increasing $B > 0$ longer equilibration times were needed. We thus chose $T_{eq} = 10^6\,\Delta t$ which worked for all studied systems with $B > 0$.

The degree of crowding is quantified by the occupied volume fraction f

$$f = \frac{\sum_i^N 4/3\,\pi R_i^3}{L^3}\,, \tag{3.20}$$

where L denotes the lateral size of the simulation box and N the number of particles. We fixed $N = 5000$ for all simulations and varied L in order to tune f between 0.01 and 0.41. Due to the linearily decaying soft-core repulsion, the *apparent* radius of

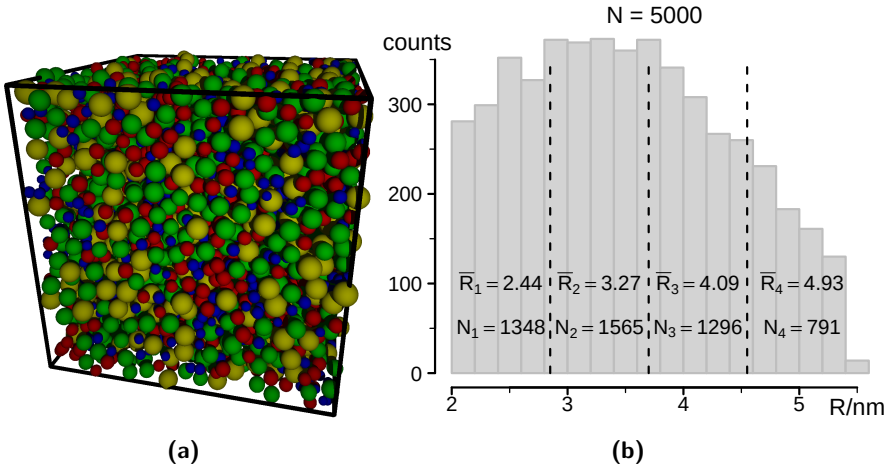

Figure 3.13 (a) A sample configuration of 5000 Brownian particles with sizes varying in the range $2 \ldots 5.5$ nm. The box has a lateral extension of 150 nm and the total occupied volume fraction amounts to $f = 0.33246$ (empirically corrected: $f = 0.46544$). (b) Size distribution of the simulated Brownian particles. The sizes are calculated from an exponential mass distribution, Equation (3.17), using the empiric formula Equation (3.18). The four size classes with mean protein radii $\overline{R}_k$ are given with the number of associated particles, N_k.

each particle is larger than R that is assigned to the extension of the repelling force plateau, cf. Section 2.1.2. To estimate the apparent occupied volume fraction, the measured diffusion coefficient as a function of f can be compared to simulations with hard-core repulsion, see Figure 3.14. Here, we used published simulation data by Cichocki and Hinsen [131] and furthermore related our data to the predictions of the Enskog theory for hard-sphere fluids [104]

$$\frac{D}{D_0} = \frac{(1-f)^3}{1-\frac{f}{2}}\,. \tag{3.21}$$

The soft-sphere system showed qualitatively the expected behavior, namely a monotonous decay of $D(f)/D_0$. The slope was steeper than for hard spheres implying that the apparent occupied volume fraction was indeed larger than f as calculated from R. We found that for our settings, f has to be corrected by $+40\%$, see Figure 3.14. The residual deviations from Enskog theory originate from the underlying approximations of this theory.

3.3.3 Results and Discussion

In a first scenario, the influence of (soft) excluded volume interactions between beads of varying size was studied. To this end, the long-time diffusion coefficient D was

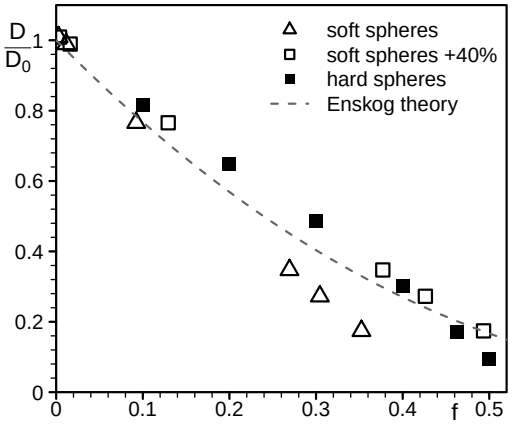

Figure 3.14 Relative diffusion coefficient D/D_0 as a function of the occupied volume fraction f for a monodisperse system ($R = 4.1$ nm). The soft-sphere simulations are compared to hard-sphere data from [131], and the Enskog theory, Equation (3.21). For the soft-sphere system the estimated excluded volume has to be corrected by plus 40% to agree with the hard-sphere system.

extracted from the computed MSD for $t > 100$ µs. Figure 3.15 shows the course of the reduced diffusion coefficient D/D_0 where D_0 corresponds to the free diffusion coefficient [Equation (3.19)]. In all, the effect of polydispersity was rather weak: Larger particles reacted a bit more sensitively and a comparison to a monodisperse scenario revealed that the beads in size class $\overline{R} = 4.10$ nm experienced practically the same reduction in diffusivity as tracers in a system with only one bead size ($R = 4.1$ nm). Hence, for the crowding-induced deceleration of diffusion, the detailed size distribution of particles does not play a role. Nevertheless, polydispersity could still be necessary to induce subdiffusion in a system of attractive beads.

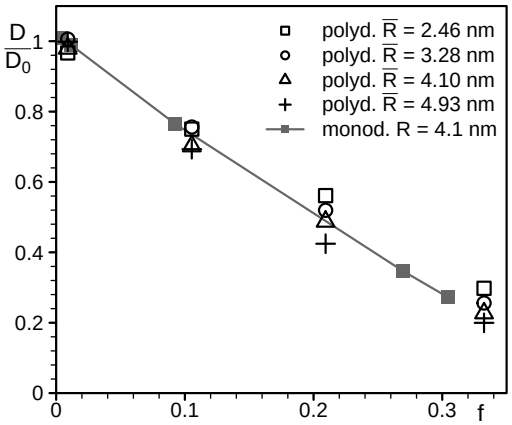

Figure 3.15 Relative diffusion coefficient D/D_0 as a function of the occupied volume fraction f for a polydisperse system. There is a slight tendency that larger particles are more affected by crowding. Comparison to a monodisperse system ($R = 4.1$ nm, gray points and line) shows that the effect of polydispersity is weak: The course of $D/D_0(f)$ for $\overline{R} = 4.1$ nm practically coincides with the monodisperse scenario.

Hence, the model was extended to incorporate an attractive force of amplitude B between two particles at intermediate surface-to-surface separation ($2 \ldots 4$ nm), cf. Figure 2.1. First, we considered a monodisperse system with $R = 4.1$ nm after 10^6 equilibration steps and again calculated the relative long-time diffusion coefficient D/D_0 as a function of f and B, cf. Figure 3.16. For $B < 2\ \mathrm{k_B T/nm}$ the data closely resembled the purely repulsive case. There was only a slight gain in slope implying that an increasing attractive force additionally slowed down particle diffusion. In contrast, for $B = 2\ \mathrm{k_B T/nm}$ a dramatic change was observed: The

diffusion coefficient dropped steeply already for intermediate f and changed only weakly for larger values. This indicates a condensation transition above a critical density. The particles form clusters with an increased local density and their diffusion is slowed down accordingly. In this regime, increasing the overall concentration of particles leads only to minor changes in D/D_0, because the density of the cluster phase is the determining factor.

The same observations were made for polydisperse systems. In the following discussions we focus on the scenario $f = 0.33$ and beads from the size class $\overline{R} = 4.1$ nm. Figure 3.17 (a) depicts the measured MSD curve and Figure 3.17 (b) the diffusion anomaly α on three different time scales. For small values of B the slope was unity on time scales above 10^3 ns indicating that normal diffusion prevailed. For $t = 10^2 \ldots 10^3$ ns the slope was smaller, i.e. $\alpha < 1$. This short transient subdiffusion arises from "cages" and is also present for purely repulsive beads [132]. The data in Figure 3.17 (b) show that α decreased with B in this regime. In other words, the caging effect gets stronger for weakly attractive particles because the additional force promotes localization.

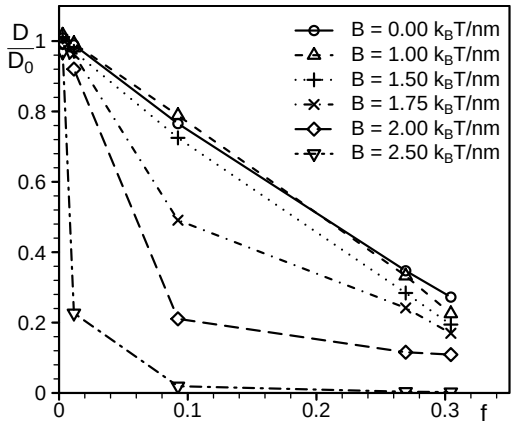

Figure 3.16 The effect of an attractive interaction of amplitude B for a monodisperse system ($R = 4.1$ nm). The behavior of $D/D_0(f)$ sensitively depends on B. For $B = 2\,\mathrm{k_BT/nm}$ the diffusion coefficient drops quickly already at small concentrations. In this scenario, the particles condense into a cluster phase that is characterized by a strongly increased local density.

In the polydisperse case, the clustering transition was slightly shifted as compared to the monodisperse scenario: We encountered a strong effect at $B = 2.5\,\mathrm{k_BT/nm}$. Figure 3.17 (a) depicts two MSDs for this interaction strength. The first belongs to a system that was equilibrated with respect to soft core repulsion but not with respect to attraction (denoted "not eq."). The other system performed $T_{eq} = 10^6\,\Delta t$ steps with all interactions turned on before data were recorded. The former case showed persistent subdiffusion with $\alpha \approx 0.8$ for $t > 10^3$ ns, while the latter exhibited an extended caging regime and normal diffusion for $t > 10^4$ ns. This indicates the above described clustering phase with an effectively increased value of f and a concomitantly decreased D. Starting from a random initial configuration that has been equilibrated with respect to the excluded volume interaction, the diffusion coefficient changes with time and the motion of particles is therefore anomalous until the equilibrium with respect to the attractive interaction (i.e. the cluster phase) is reached.

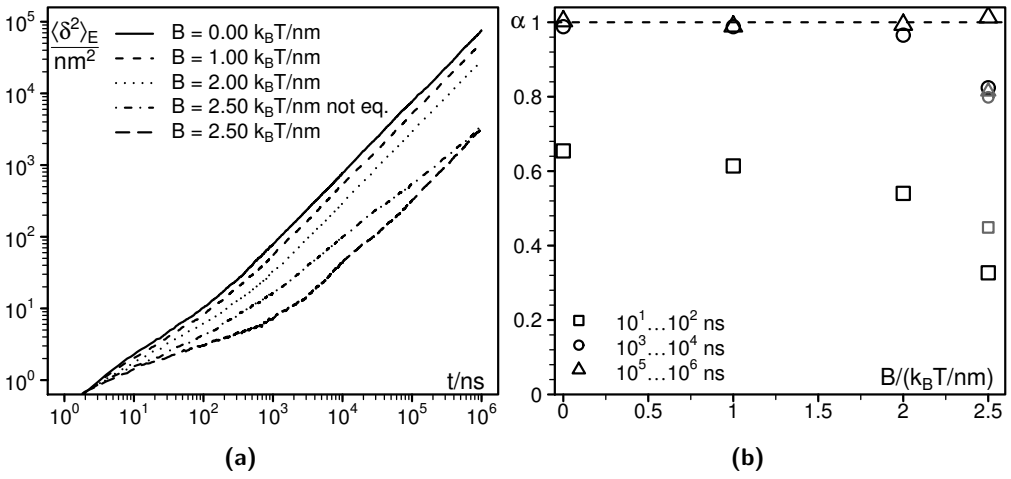

Figure 3.17 (a) The MSD in a polydisperse system of attractive Brownian particles. For the attractive force amplitude $B = 2.5\,\mathrm{k_BT/nm}$ two scenarios are shown. One went through an equilibration w.r.t. excluded volume only (denoted "not eq."), while the other one was thoroughly equilibrated with active attraction. (b) The measured anomalies for different time scales. The gray symbols indicate the "not eq." setting for $B = 2.5\,\mathrm{k_BT/nm}$. This system exhibits a strong anomaly on all experimental scales that vanishes after full equilibration. On intermediate time scales subdiffusion was robust w.r.t. to longer equilibration.

The diffusion anomalies in Figure 3.17 show that subdiffusion in the caging regime, i.e. on intermediate scales ($t = 10^3 \ldots 10^4$ ns), was robust with respect to longer equilibration. The same observations have been made in detailed molecular dynamics simulations of attractive colloids by Zaccarelli *et al.* [132]. Indeed, the transition between bulk behavior and clustering originates in the interplay between attractive and repulsive forces. If the two contributions balance, subdiffusion can persist over several decades in time.

As described in Section 1.3.4 there are different models for crowding-induced subdiffusion. So far, the proposed model assumed that all particles are mobile and move through an isotropic space. In a conceptually different scenario, mobile tracers move through a porous medium. This setting represents an OD model described in Section 1.3.4 and hence is anticipated to bear subdiffusion. We immobilized a fraction p of the particles after equilibration with respect to excluded volume that consequently formed a random environment for the remaining ones. Figure 3.18 shows the resulting MSD curves (a) and computed anomalies (b) in dependence on p. At $p = 0.5$ the transient subdiffusion extended to the experimentally accessible regime on the 100 µs-scale. This effect was robust with respect to an longer equilibration as indicated in Figure 3.18. The measured anomalies dropped with increasing p on all scales.

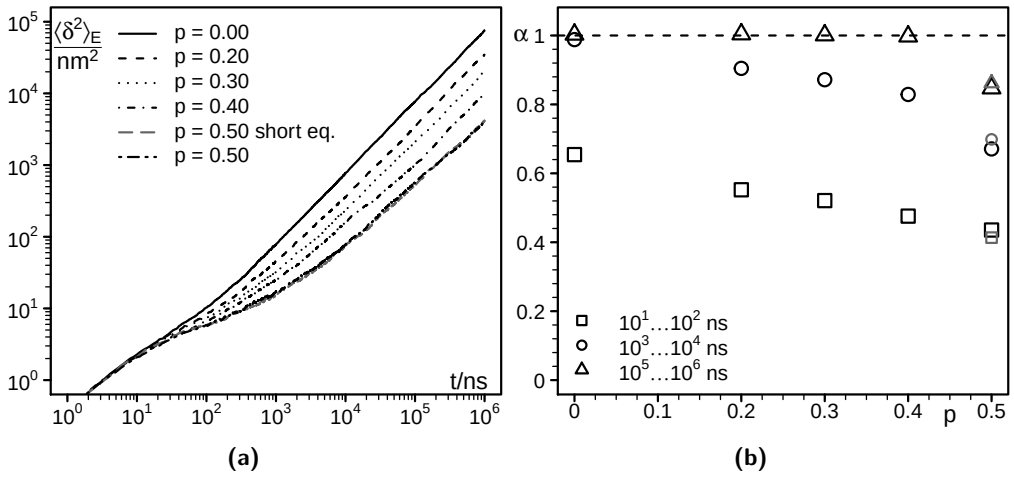

Figure 3.18 (a) MSD when a fraction p of particles is immobilized at random positions. The remaining mobile tracers move trough a static, random environment. As a result subdiffusion is observed to an extent that depends on p. (b) the computed diffusion anomalies on different time scales. The gray points indicate the typical equilibration time for $p = 0.5$ while the black symbols stand for simulations with a longer equilibration time.

3.3.4 Summary and Conclusions

Here, we proposed a mesoscopic model for a complex fluid inspired by the crowded cytoplasm. It incorporates (soft) excluded volume of proteins, a realistic size distribution, and unspecific attractive interaction between particles at intermediate distances. Realistic parameter values were chosen in order to judge whether the observed diffusion effects translate to experimental time scales. For bulk diffusion in a crowded environment the model reproduces the behavior of hard spheres indicating that the soft repulsion resembles a valid approximation. The vaguely defined bead radii do not have qualitative impact on the diffusive behavior. This also holds for tracers in a static, random environment showing anomalous subdiffusion as expected for an OD scenario, cf. Section 1.3.4.

In summary, the data suggest that subdiffusion requires a kind of attractive interaction between the particles to emerge. We have introduced a diffuse, unspecific attraction that induces a transient, weak association without explicitly accounting for particular bonds. This yielded transient subdiffusion starting approximately at an interaction strength of $B \approx 2\,\mathrm{k_BT/nm}$ but this effect does not translate to experimental time scales. Apparently, the proposed model is too simplistic to describe subdiffusion observed by FCS or SPT.

The explicit modeling of individual bonds resembles a possible further extension – a kind of approach that has already been applied successfully in studies on clustering

[133] and gelation [75]. Such an algorithm requires a much higher computational effort, especially if geometrical aspects like bond angles are incorporated. Thus, a parallelized implementation may be necessary in order to reach the desired time scales. It is a promising observation, that the shape of the particle MSD in such a model (e.g. [133]) is reminiscent of the MSD measured in a viscoelastic fluid, cf. Section 1.3.3. Hence, it may be anticipated that subdiffusion in the model fluid exhibits features of FBM, cf. Section 1.3.4. This would add to the growing evidence that crowding-induced subdiffusion is well described by FBM, cf. Section 1.3.5. The parameters that determine the inter-particle bonding up to the desired level of detail could be interpreted as the approximative, microscopic architecture of the complex fluid under consideration. In the end, such an architecture could imply a stable gelation that results in a porous medium through which the remaining particles diffuse. This setting naturally bears subdiffusion as has been shown above where the porous topology of space was imposed by turning some particles immobile.

Chapter 4

Anomalous Reaction Kinetics

4.1 Anomalous Reaction Kinetics in Crowded Membranes

The results of this section have been presented at the *55th Annual Meeting of the Biophysical Society*[1]. Furthermore, a large part of this section appeared as a paper in *EPL (Europhysics Letters)*[2].

4.1.1 Introduction

So far, particle-based simulations of reaction-diffusion in crowded environments use either a lattice with immobile obstacles covering a substantial fraction of nodes (e.g. [99, 100, 134]) or (coarse-grained) molecular dynamics simulations of hard spheres (e.g. [103, 104, 105]). The former approach considers the reactants embedded into a (sub)percolating environment and thus gives rise to fractal-like kinetics [88] (see Section 1.4.2), i.e.

$$k(t) = k_0 t^{-h} \quad 0 \leq h \leq 1 \quad (t \geq 0)\,. \tag{4.1}$$

Furthermore, due to the topological constraints imposed by the obstacles, the fractal dimension of a random path, d_W, increases and diffusion becomes (transiently) anomalous, cf. Section 1.3.4. The latter method focuses on the impact of the volume occupied by mobile, inert crowders. In this scenario diffusion is slowed down but still normal in character. The excluded volume effect leads to changed association rates [104] which agree with thermodynamic calculations [18].

In general, the kinetics of a diffusion-limited reaction can be classified to be either classical ($h = 0$) or geometry-controlled ($h > 0$) [97], cf. Section 1.4.2. The distinction between these two regimes is given by the sampling behavior of the reactants' diffusion process: If the fractal dimension of the particle trajectories (d_W) is lower than the fractal dimension of the support (d_f), the exploration is non-compact. As a consequence, classical reaction kinetics ($h = 0$) is observed, i.e. reactants are well-stirred by diffusion and the law of mass action is valid. This scenario in particular applies to reactions in bulk solution ($d_f = 3$) as the fractal

[1] M. Hellmann, D. W. Heermann, and M. Weiss, 1376-Pos: Impact of Anomalous Diffusion on Biochemical Kinetics, *Biophysical Journal*, **100** (3), 251a (2011)

[2] M. Hellmann, D. W. Heermann, and M. Weiss, Anomalous reaction kinetics and domain formation on crowded membranes, *EPL* 94(1), 18002 (2011)

dimension of Brownian motion is $d_W = 2$. For $d_W < d_f$, however, diffusion samples the available space in a compact fashion, hence leading to a less effective mixing of reactants. As a consequence, $h > 0$ and even an initially well-mixed setup segregates into A- and B-rich regions due to initial concentration fluctuations ('Zeldovich effect' [89]), cf. Section 1.4.2.

Here we present full-stochastic, i.e. particle based, reaction-diffusion simulations that account for viscoelastic interactions in a two dimensional (2D) complex fluid like the cellular membrane. These interactions can be modeled by subdiffusion in terms of fractional Brownian motion (FBM), see Section 1.3.4. All solvent-solute and crowder-solute interactions are summarized in an external stochastic force characterized by an autocorrelation function that decays with time as t^{-2H}. $H = \alpha/2$ denotes the Hurst exponent and α the resulting diffusion anomaly. Typically, the effect of crowding in reaction-diffusion systems is studied by changing the fractal dimension d_f of the support, e.g. by introducing static obstacles (cf. above). Here, we leave d_f unchanged and rather modify the fractal dimension of the diffusion process $d_W = 2/\alpha$ directly. Moreover, space is isotropic and all regions may in principle be visited by all reactants.

Bearing in mind that protein diffusion on cellular membranes has been reported to often have an anomalous character, the considered reaction scheme may represent, for example, the concomitant dissociation of the peripheral membrane protein Arf-1 (A) and its hydrolysis-stimulating factor ARFGAP1 (B) from Golgi membranes (then: $C = \emptyset$) [135] . In the investigated scenario, we find that both, normal and anomalous diffusion induce a non-classical (fractal) kinetics, i.e. $h > 0$ with a value that depends on the anomaly α of the random walk. Owing to an increased compactness of the random walk, subdiffusion also strongly enhances reactant segregation and hence may promote the formation of functional domains on cellular membranes, e.g. hot spots on Golgi membranes that show an enrichment of Arf-1 and hence have a higher probability to form transport vesicles.

Additionally, we present some preliminary results for reactions in three dimensions (3D). Since FBM allows to continuously adjust the fractal dimension of the reactant trajectories, the transition between classical and geometry-controlled kinetics can be studied. The distinction between the regimes is not sharp due to the limited system size and simulation times. Still, we can identify a different behavior in the course of $h(t)$ indicating that a transition occurs.

4.1.2 Parameters and Setup

We applied the methods described in Section 2.3 with three reactant species A, B, and C and a reaction radius R. For the reaction A + B $\rightarrow$ C without excluded volume, the C species was practically invisible and our reaction scheme reduced, strictly spoken, to A + B $\rightarrow \emptyset$. The initial number of particles was chosen as $N_A = N_B = N/2 = 2500$ (2D) and $N_A = N_B = N/2 = 7500$ (3D), respectively. By periodic boundaries of the simulation box we emulated a subvolume of an infinite system at a global concentration. The system size L was adjusted so that the volume (area) within the

reactive radii $N \times 4/3\pi R^3$ ($N \times \pi R^2$) amounted to 6% of the total volume (the total area). Diffusive trajectories were generated using the Brownian dynamics approach (see Section 2.1.2), while subdiffusive reactants followed a FBM generated by the Weierstrass-Mandelbrot function (see Section 2.2.3). The parameter values for the three and two dimensional simulations are summarized in Table 4.1.

As steering parameters of the system we varied the anomaly exponent α of the FBM process in an experimentally relevant range $\alpha = 0.5 \ldots 1.0$, cf. Section 1.3.3. The probability P that upon an encounter two reactants A and B merge to a C was selected among $0.002 \ldots 1$. A reaction probability below unity may be interpreted as a lowered affinity between the reactants; in fact, most reactions will not occur directly on collision when the geometry of the reactants is taken into account, meaning that A and B have to be aligned in a certain manner for the reaction to take place.

Parameter	simul. units (2D)	simul. units (3D)
R	1	=
L	$500\,R$	$100\,R$
Δt	2×10^{-7}	=
T	2.5×10^{-5}	5×10^{-5}
D	0.5	=
$N_A(0)$	2500	5000
$N_B(0)$	2500	5000
α	$0.5 \ldots 1.0$	=
P	$2 \times 10^{-3} \ldots 10^{0}$	=

Table 4.1 The parameters of the full-stochastic reaction-diffusion simulations in two and three dimensions.

To follow the course of the reaction we recorded the instantaneous particle numbers and corresponding densities $N_A(t)$ (ρ_A), $N_B(t)$ (ρ_B), and $N_C(t)$ (ρ_C) as the average over 1000 independent runs. From this the anomalous reaction exponent h was obtained via [102]

$$\frac{1}{\rho_A(t)} - \frac{1}{\rho_A(0)} \propto t^{1-h} \,. \tag{4.2}$$

The logarithm of the left versus the logarithm of the right hand side gave a (locally) linear increase with slope $1 - h$. We were interested in the course of h with time and thus calculated $h(t)$ by the difference quotient between two successive values of ρ_A. The counts of AA-, BB, and AB-pairs provide additional information on the spatial organization of reactants [136]. We denote these numbers by N_{AA}, N_{BB}, and N_{AB}. In our continuous space simulations, two particles were considered a pair if their center-to-center distance was less than $2.4\,R$. With the numbers of pairs, the

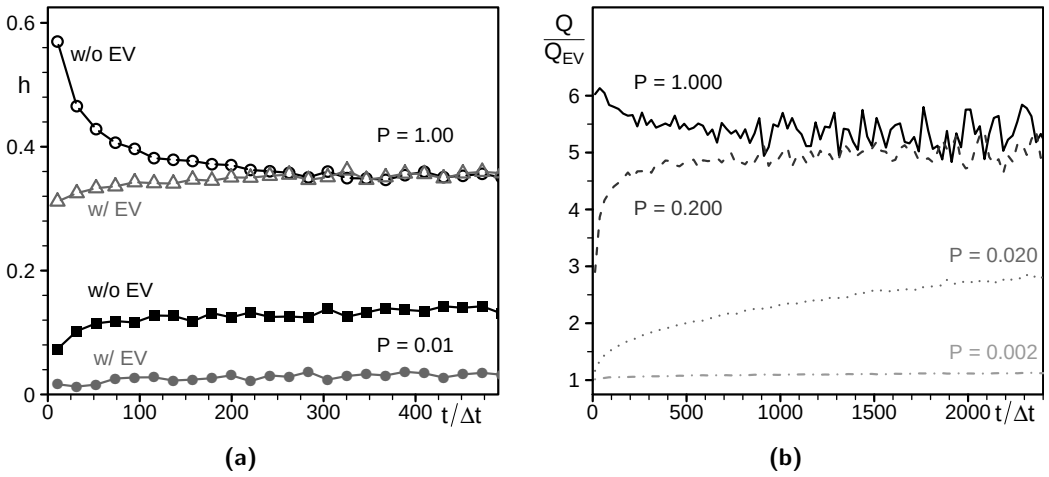

Figure 4.1 (a) Comparison of the time dependent reaction anomaly $h(t)$ between scenarios with and without excluded volume interactions in 2D. (b) Ratio of Q as measured without excluded volume and Q_{EV} obtained in a system with excluded volume.

segregation of reactants could be quantified according to [99]

$$Q = \frac{N_{AA} + N_{BB}}{N_{AB}} \left(\frac{\rho_{\mathrm{A}}^2 + \rho_{\mathrm{B}}^2}{2\rho_{\mathrm{A}}\rho_{\mathrm{B}}} \right)^{-1} . \tag{4.3}$$

4.1.3 Results and Discussion

The Role of Excluded Volume

As stated in Section 2.3 the used simulation algorithm cannot properly account for the finite size of reactants. This leads to artifacts which shall be discussed for reactants undergoing Brownian motion ($H = 0.5$): Figure 4.1 (a) shows the course of the reaction anomaly $h(t)$ for systems with and without excluded volume interaction. For the diffusion-limited scenario ($P = 1$) the data differed strongly in the beginning. While phantom discs provoked a pronounced non-classical behavior for small t, their hard counterparts gave rise to classical kinetics at $t = 0$ (this is not well visible in the figure, since the data have been averaged over intervals of 21 time steps, cf. [100]). After approximately 300 time steps, however, the data reached the same asymptotic h_∞ that is in excellent agreement with earlier publications [100].

For $P < 1$ the values differed significantly over the whole time window shown in Figure 4.1 (a). This phenomenon becomes clearer from Figure 4.1 (b) where the reactant segregations in terms of Q [Equation (4.3)] are compared: The time course of the ratio Q/Q_{EV} exhibited a nearly constant asymptotic for the extremes of diffusion and reaction limitation ($P = 1$ and $P = 2 \times 10^{-3}$, respectively). In the

first case, reactant segregation was approximately five times stronger if excluded volume was neglected. For the latter case, almost no reactions took place and hence there was no significant segregation in either of the scenarios; consequently, the ratio is close to unity. Intermediate probabilities ($P = 2 \times 10^{-2}$) constituted a cross-over behavior between the two extremes where Q/Q_{EV} depended non-trivially on time. This regime corresponds to the differing values of h in Figure 4.1 (a). Without excluded volume a stronger reactant segregation evolves from the well-stirred initial condition and the ratio Q/Q_{EV} grows with time as the reaction proceeds. The slope of the increase was determined by the "velocity" of the reaction, i.e. the value of P.

In summary, our data show that the observations of Zeldovich segregation and anomalous reaction kinetics are robust with respect to excluded volume. The asymptotic values h_∞ and hence the scaling of the reaction coefficient coincide for diffusion-limited reactions. Reactant segregation is stronger for phantom reactants because, on the average, unrestricted overlaps make the A- and B-rich regions more compact and the voids in between larger. As the particle number decreases, this effect of excluded volume becomes less relevant. Quantitative differences arise for intermediate values of the reaction probability when the reaction proceeds slowly. In a system of phantom disks the separation grows faster and hence the reaction anomaly is larger than in case of hard disks. Still, all qualitative conclusions stay untouched in the pre-Zeldovich regime because effectively only the time scale of this transient is shifted.

Fractal-like kinetics

Starting from a well-mixed initial setup in the diffusion-limited regime ($P = 1$), the reaction exponent h tended to a nonzero value h_∞ at large times [Figure 4.2 (a)] for all anomalies α. For normal diffusion we observed $h_\infty \approx 0.36$ in agreement with previous simulations that accounted for the finite volume of reactants [100]. In fact, for this case an asymptotic decay $h \sim 1/\ln t$ is expected [93], i.e. h_∞ should not be a real asymptotic value. Owing to the limited resolution and finite length of our simulations, however, we were unable to detect the asymptotic logarithmic decay. Hence, h_∞ should be considered as a phenomenological description in the accessible time window (cf. also discussion in [99]).

In the case of obstructed diffusion (OD), the reaction anomaly h increases with growing concentration of obstacles [99]. On the other hand, this gives rise to a stronger diffusion anomaly [71]. In close analogy one would expect for reactants driven by FBM to find a higher reaction anomaly for smaller α. Indeed, fractal-like reaction kinetics predicts the relationships $h = 1 - d_S/2$ before the onset of the Zeldovich-segregation regime and $h = 1 - d_S/4$ afterwards [92], where $d_S = 2d_f/d_W$ denotes the spectral dimension of the random walk [68], cf. Section 1.3.4. For FBM trajectories in the plane $d_f = 2$ and $d_W = 2/\alpha = 1/H$. Thus one anticipates respectively $h = 1 - \alpha$ and $h = 1 - \alpha/2$. To obtain a similar picture as for reactions on fractal supports it is convenient to plot h_∞ as a function of $1 - \alpha$. The finiteness of our simulations, the lack of excluded volume interactions, and reaction probabilities

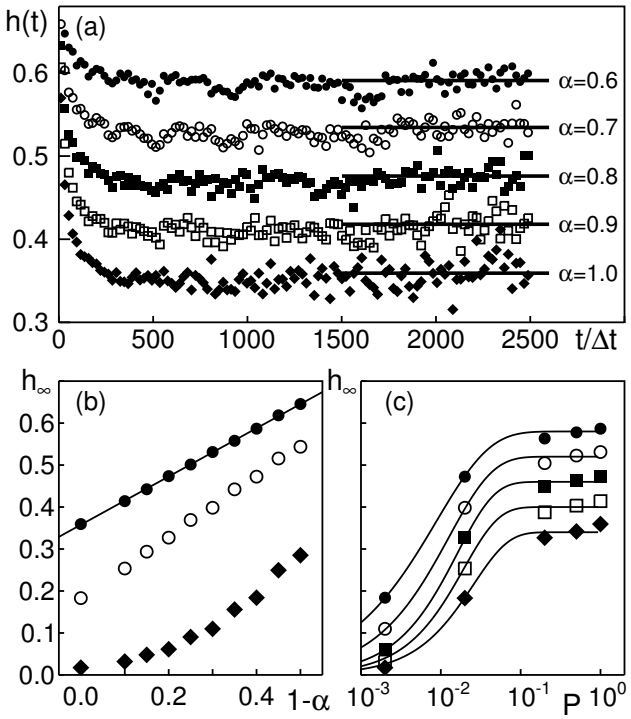

Figure 4.2 (a) Time course of the reaction exponent, $h(t)$, [Equation (4.1)] for various anomalies α in the diffusion-limited regime ($P = 1$). All curves show a plateau $h(t) \to h_\infty > 0$ for long times. To reduce fluctuations, $h(t)$ was averaged here over 21 consecutive time points. (b) Reactant segregation is indicated by a scaling $h_\infty = c_1 - c_2\alpha$ with $c_2 = 1/2$. For the diffusion-limited regime ($P = 1$, filled circles) a strong segregation has emerged already ($c_2 \approx 0.57$) (full line) while it has not yet emerged for lower reaction probabilities $P = 0.02, 0.002$ (open circles and filled diamonds, respectively). (c) The reaction exponent h_∞ increases sublinearly with the reaction probability P (note the log-scale for P). Full lines are stretched exponentials as a guide to the eye; symbols as in (a).

$P \leq 1$ lead to deviations from the theoretical predictions and we rather observed a modified relation between h_∞ and α:

$$h_\infty = c_1 - c_2\alpha \quad \text{with} \quad 1/2 \leq c_2 \leq 1\,. \tag{4.4}$$

In accordance with previous studies [99] we found indeed for large reaction probabilities ($P > 0.1$) a strong indication for segregation, i.e. $c_2 \approx 0.57$ (Figure 4.2 b). When lowering the reaction probability to $P = 0.02$ an intermediate scaling ($c_2 \approx 0.73$) emerged, as the macroscopic segregation has not been established in full during the simulation time. For very small reaction probabilities ($P = 0.002$) only first traces of the Zeldovich regime were visible, i.e. one would need considerably longer simulation runs to observe the segregation for these small reaction probabilities.

Reactant Segregation

To illustrate the segregation of reactants during the simulation, we show the spatial distribution of A and B-rich regions in Figure 4.3. The system was divided into 25×25 square cells for each of which the contained A and B particles were counted. This number minus the expected cell occupation for a homogeneous distribution of

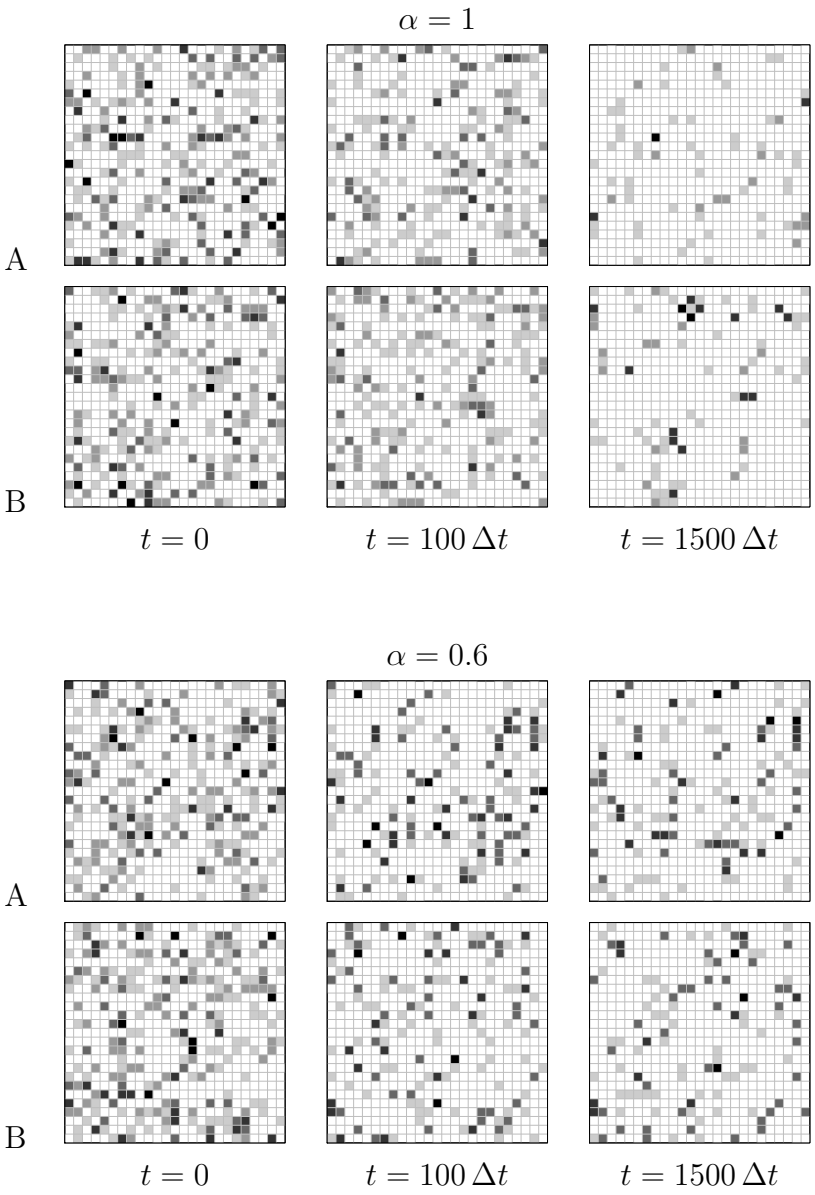

Figure 4.3 The spatial distribution of reactants quantified by the count of excess particles. The system is divided into 25×25 square cells for which the excess of A and B particles is calculated at the indicated time points. The excess is defined as the difference between the actual count of particles in each cell and the expected count for a homogeneous distribution. The legend on the left explains the color coding. Normal and anomalous diffusion give rise to reactant segregation, i.e. well separated A- and B-rich regions emerge from the initial density fluctuations. Subdiffusive reactants enhance segregation due to their more compact trajectories.

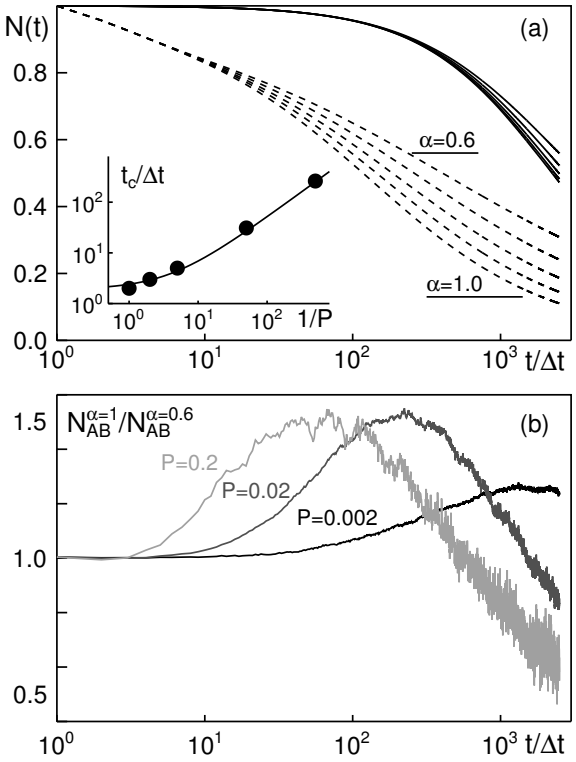

Figure 4.4 (a) Time course of reactants, $N(t)$, for $P = 0.002$ and $P = 0.2$ (full and dashed lines, respectively). Curves in each ensemble are ordered according to increasing α (cf. indication at dashed curves), i.e. normal diffusion yielded a higher amount of products per time than anomalous diffusion. Inset: At a time scale t_c the number of reactants has decreased by 10%, and this time scale increases linearly with the inverse reaction probability, $t_c \approx 2 + 1/(2P)$ (full line), irrespective of the value of α. (b) The ratio of reactive pairs for normal and strongly anomalous diffusion, $N_{AB}(\alpha = 1)/N_{AB}(\alpha = 0.6)$, shows a strong increase beyond t_c, hence highlighting the faster formation of reactive pairs by normal diffusion. Only at large times, subdiffusive reactants that have not yet undergone a reaction but are near to each other lead to an inversion of the ratio. Shown are three reaction probabilities (color-coded) as indicated.

particles yielded the *excess*. It is clearly visible that the random distribution of the reactants in the system induces pronounced spatial density fluctuations.

To get a more detailed picture of reactant segregation in the progress of the reaction, we inspected the number of reactants, $N = N_A + N_B$, and the number of reactive pairs, N_{AB}. For a vanishing reaction probability, $P = 0$, N was strictly conserved, and N_{AB} was constant on average for all α. Thus, FBM and normal diffusion lead to equivalent randomizations of the particle positions. In the reaction-limited scenario ($P \ll 1$) the number of encounters per successful reaction is large. As a consequence, a substantial decrease of reactants only emerged beyond a critical time $t_c \sim 1/P$ that is almost independent of α (Figure 4.4 a). Beyond t_c also more subtle differences between subdiffusion and normal diffusion became clearly visible. When inspecting the ratio of reactive pairs for normal and subdiffusive motion, $N_{AB}(\alpha = 1)/N_{AB}(\alpha = 0.6)$, a strong increase at t_c is visible (Figure 4.4 b). This feature indicates that subdiffusion is significantly less efficient in replenishing the pool of reactive pairs. For large times, when normal diffusive reactants became very rare, their subdiffusive counterparts were still relatively abundant. Hence anomalous

diffusion yielded more AB pairs in this limit.

As a consequence of the slower sampling process, the amount of product C, i.e. $N_C(t) = N(0) - N(t)$, increased slower for subdiffusion. Hence, the reactants stayed on average more separated. This enhanced segregation of reactants is highlighted by the quantity Q [Equation (4.3)]. While the anticipated lack of segregation at $P = 0$ was reflected by $Q = 1 \pm 0.02$ in our simulations, we observed $Q(t) > 1$ even for normal diffusion when the reaction probability was large (Figure 4.5). For subdiffusion the segregation was even stronger the lower α became. Thus, the slower reaction progress for subdiffusion is acompanied by a stronger segregation of reactants.

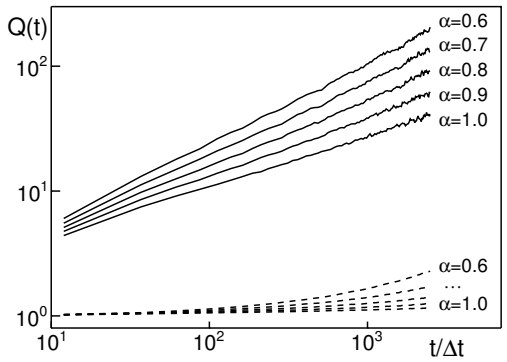

Figure 4.5 The parameter $Q(t) > 1$ [Equation (4.3)] highlights a strong segregation of reactants for $P = 0.2$ (full curves) and $P = 0.002$ (dashed curves). As a consequence of the slow sampling process, subdiffusion shows a strong enhancement of the segregation event.

Extension to 3D space

Since FBM allows one to continuously adjust the diffusion anomaly, it provides a means to study the transition between geometry-controlled and classical kinetics. In the plane, compact exploration and hence geometry-controlled kinetics prevails even for $\alpha = 1$. In three dimensions, however, both scenarios can be investigated. In particular, for $\alpha > 2/3$ classical kinetics and for $\alpha \leq 2/3$ geometry-controlled kinetics are anticipated [97] because the fractal dimension of a FBM trajectory is $d_W = 2/\alpha$, cf. Section 1.3.4. On the other hand, it is known that Zeldovich segregation and hence anomalous kinetics should arise in three dimensions for the conditions that apply here ($N_A = N_B$ and batch conditions), cf. Section 1.4.2. The periodic boundaries of the simulation box, however, impose effective convection currents that contribute to the stirring of the reactants [92]. We thus rather expect classical kinetics.

Figure 4.6 (a) shows the course of the reaction anomaly $h(t)$ for A + B → C in 3D. In the limited time window accessible by the simulations, h did not fully settle to a constant h_∞ for all diffusion anomalies. The long time behavior can be approximated by a linear decrease (solid lines in the respective time interval). At this point, the slope s may be interpreted as an indicator for the final asymptotic: If s is negative, h tends to zero for $t \gg 1$. On the other hand, if $s \approx 0$, h takes a nonzero value h_∞. Indeed, as seen in Figure 4.6 (b) the dependence of s on α exhibits roughly the expected distinction between compact and non-compact exploration: For $\alpha > 2/3$ s

decreased with α, indicating that it took longer for weakly subdiffusing reactants to reach the classical limit than for normally diffusing ones. Beneath $\alpha = 2/3$ s stayed close to zero.

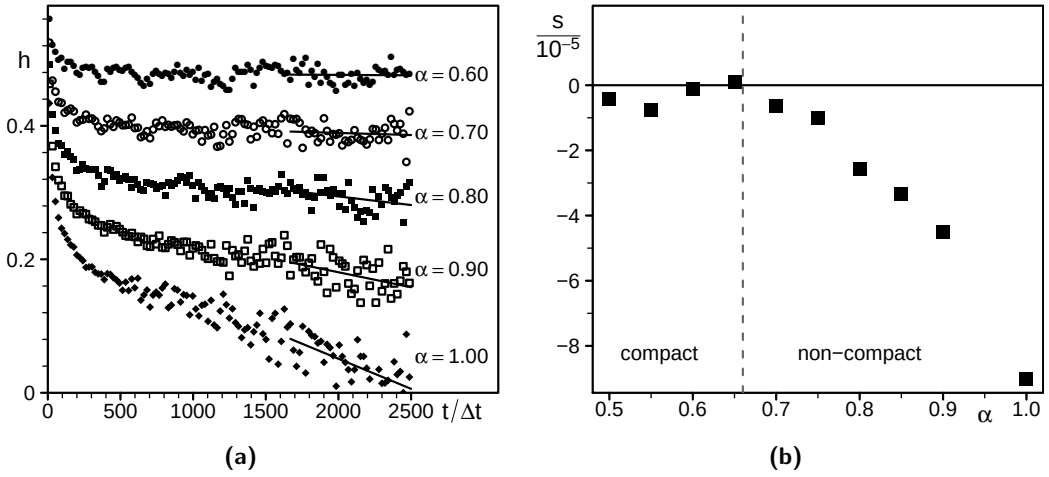

Figure 4.6 (a) The course of $h(t)$ for A + B $\rightarrow$ C in 3D. Within the considered time window not all anomalies lead to a constant h_∞. Anyhow, the asymptotic can be approximated by a linear decrease of h with t. Solid lines show the linear fit in the respective time regime. (b) Slope s of the asymptotic decay of $h(t)$ in dependence on the diffusion anomaly α. In the regime of compact exploration ($\alpha \leq 2/3$) $s \approx 0$, i.e. $h_\infty > 0$ and non-classical kinetics prevails. In contrast, non-compact walks ($\alpha > 2/3$) yield a negative slope that may be interpreted as a transient towards $h_\infty \rightarrow 0$, hence implying classical kinetics.

4.1.4 Summary and Conclusions

The overall picture that emerges from our simulations is that product formation by subdiffusive reactants is slower than for normal diffusion. The subdiffusive reactants' trajectories are oversampling the available two-dimensional space even more than normal diffusion already does. Hence, the same molecules are re-encountered over a long period which supports a strong segregation of reactants.

One may have expected that an enhanced re-encounter rate supports the progress of the reaction scheme at low P since reactants stay near to each other and thus may have several attempts to form a product. Contrary to this assumption, our data show that independently of P the diffusion-limited formation of *new* pairs is the most important factor.

This observation, however, is intimately linked to an enhanced reactant segregation for anomalous diffusion. It is tempting to speculate if and how biological systems may utilize or benefit from this effect. Let us consider as an example the COPI vesicle

machinery at the Golgi apparatus [135]. The small GTPase Arf-1 (a soluble protein when bound to GDP) will firmly associate with Golgi membranes upon nucleotide exchange. Independent of this event, ARFGAP1 will bind to the membrane. Upon encountering each other, ARFGAP1 will trigger the hydrolysis of GTP by Arf-1 which leads to the dissociation of both proteins from the Golgi membrane. Hence, this reaction on the membrane is well described by $A + B \to \emptyset$. Given the above results, regions on the membrane should exist that have higher concentrations of Arf-1. Since Arf-1 is the docking factor for coatomer, a protein that serves in the formation of transport vesicles, this segregation would induce 'hot spots' at which vesicles are produced with higher probability. It will be interesting to test this prediction experimentally, e.g. by electron microscopy.

Beyond the quite robust data for reactions in the plane we also presented some preliminary results for bulk reactions. In this context the transition between compact and non-compact exploration and the respective scenarios, geometry-controlled versus classical kinetics, were considered. Due to the limited simulation time and the strong stochasticity of $h(t)$ our data do not yield a sharp distinction between the two regimes. However, the anticipated tendency is visible. More powerful simulations that allow for larger systems and longer simulation times can lead to further progress in this direction and ultimately link the concept of geometry-controlled kinetics to subdiffusive reactants in the bulk.

4.2 Michaelis-Menten Kinetics in a Viscoelastic Medium

The results of this section have been presented at the *55th Annual Meeting of the Biophysical Society*[3]. Furthermore a major part of this section has been submitted for publication.

4.2.1 Introduction

Enzymatic reactions are ubiquitous events that are of vital importance for living cells [1], see Section 1.2.2. A prototypical enzymatic reaction that lies at the heart of virtually all cellular signaling pathways is the phosphorylation of proteins [6]. Here, a kinase E covalently adds a phosphate to another protein (its substrate) S according to the Michaelis-Menten scheme [cf. Equation (1.1)]:

$$\mathrm{E} + \mathrm{S} \underset{k_2}{\overset{k_1}{\rightleftharpoons}} \mathrm{C} \overset{k_3}{\to} \mathrm{E} + \mathrm{P} \ . \tag{4.5}$$

As a matter of fact, central hubs of signaling cascades may attain even several phosphorylations by the same kinase, and the subsequent response of the pathway may depend on the precise phosphorylation pattern [6, 9, 137].

Kinases are traditionally classified as working in a *distributive* or *processive* fashion, depending on whether they can add only one or multiple phosphates while

[3] M. Hellmann, D. W. Heermann, and M. Weiss, 1376-Pos: Impact of Anomalous Diffusion on Biochemical Kinetics, *Biophysical Journal*, **100** (3), 251a (2011)

being in a complex with the substrate. Reducing the repetitive diffusive search for the substrate, processive kinases are considered more productive, i.e. they yield a higher amount of multi-phosphorylated proteins per time. The simplest case in which a processive kinase may outperform a distributive one is a double phosphorylation event:

$$\mathrm{E} + \mathrm{S} \underset{k_2}{\overset{k_1}{\rightleftharpoons}} \mathrm{C}_1 \overset{k_3}{\rightarrow} \mathrm{E} + \mathrm{P}_1 \underset{k_2'}{\overset{k_1'}{\rightleftharpoons}} \mathrm{C}_2 \overset{k_3'}{\rightarrow} \mathrm{E} + \mathrm{P}_2 \ . \tag{4.6}$$

Prominent examples for double-phosphorylated proteins are the members of the mitogen-activated protein kinase (MAPK) family that become active only after attaining two phosphorylations by the MAPK kinase, cf. Section 1.2.2. Indeed the double phosphorylation is the prerequisite for MAPK to translocate from the cytoplasm to the nucleus in order to regulate gene transcription [8].

Using the law of mass action, Equation (4.5) and Equation (4.6) can be formulated as a set of ordinary differential equations (ODEs) in a straightforward manner. Indeed, this approach is commonly used to model biochemical signaling networks [138, 139]. The use of ODEs tacitely relies on two crucial assumptions: (i) all reactants are so abundant that one may use a mean-field formulation in terms of concentrations, and (ii) diffusive transport of all molecules is so fast that the reactants are always well-stirred. Both assumptions, however, may go wrong in the cellular context. The copy number of proteins of a typical signaling cascade varies between 10^4 and 10^7 per cell [138], i.e. from 30 nM to 30 μM. It is hence questionable at least for the lower bound to which extent (local) concentrations are a valid means to describe intracellular enzymatic reactions. Furthermore, particle based simulations reveal that spatio-temporal correlations have a dramatic impact on the behavior of molecular signaling pathways [108]. They can, for example, destroy the classically anticipated (bi)stability of a biochemical network. As to the second concern, diffusion in the crowded cytoplasm is very slow and often shows even an anomalous behavior, i.e. the proteins' mean square displacement (MSD) has a subdiffusive characteristics, $\langle \delta^2 \rangle \sim t^\alpha$ with $\alpha < 1$, cf. Section 1.3.4. Subdiffusion often emerges as a consequence of the viscoelastic nature of crowded fluids [24, 35, 78] which equips the molecules' random walk with the characteristics of fractional Brownian motion (FBM) [65]. Diffusive mixing of proteins in intracellular fluids therefore resembles a very slow and ineffective process that undermines the assumption of a well-stirred fluid.

Here we show by means of extensive simulations that crowding-induced subdiffusion drastically alters the time course of successive enzymatic reactions in three-dimensional space, e.g. multi-phosphorylation events in the cell's cytoplasm. In particular, we find that a single-step process [Equation (4.5)] is slowed down and reveals non-classical (fractal) kinetics [88] when molecules undergo subdiffusion. In contrast, for a double phosphorylation event [Equation (4.6)], subdiffusion can massively enhance the product yield within a short period. This means the efficiency of a double phosphorylation is enhanced under crowding conditions even if the kinase is non-processive in the first place. So, the more compact trajectories of subdiffusive reactants imply a higher re-encounter probability. As a result, an intrinsically

distributive kinase may be turned into a processive one.

4.2.2 Parameters and Setup

The particle-based simulations of Michealis-Menten reactions extent the algorithm already described in Section 4.1. That is, diffusive and subdiffusive trajectories were generated by Brownian dynamics and the Weierstrass-Mandelbrot function, respectively (cf. Section 2.1.2 a nd Section 2.2.3). Particles were considered as phantom spheres with an interaction radius R. When the distance between enzyme and substrate was less than $2R$ these particles were allowed to react with the respective rate. Performing particle-based simulations, we modeled the reaction rates by the corresponding reaction probabilities, i.e. $k_1 \to p_1$, etc. In order to realize a particular target reaction rate, the probability and reaction radius have to be adjusted accordingly [124]. Here the focus is on generic phenomena and hence we omitted the adaption to precise reaction rates. Moreover, an empirical factor consistently converted between probabilities in the stochastic simulations and reaction rates in the ODE picture.

The initial number of particles was $N_E = 4000$, $N_S = 16000$, and the system size $L = 200R$. Subdiffusive reactants followed a FBM with $\alpha = 0.6$. Varying the reaction probabilities p_2, and p_3 yielded a phase diagram visualizing the interplay between production and intermediate decay. To avoid too fast rebinding of just dissociated proteins we chose a rather small association probability $p_1 = 0.05$. The measured quantities comprise the instantaneous concentrations E, S, $C_{1,2}$, $P_{1,2}$ and ν, the number of E + S reactions that effectively gave rise to complex formation until time t. All important parameters and their values are summarized in Table 4.2.

Parameter	**simul. units (3D)**
R	1
L	$200\,R$
Δt	2×10^{-7}
T	2.5×10^{-5}
D	0.5
$N_E(0)$	4000
$N_S(0)$	16000
α	0.6 and 1.0
p_1	0.05
p_2,p_3	$0.02 \ldots 0.10$

Table 4.2 The parameters for the full-stochastic reaction-diffusion simulations of a (double) Michaelis-Menten scheme in three dimensions.

Classical Kinetics: Ordinary Differential Equations

The classical expectations are given by the solution to the system of kinetic ordinary differential equations (ODE). For the case of a simple Michaelis-Menten scheme, Equation (4.5), they read:

$$dE/dt = -k_1 ES + (k_2 + k_3)C \tag{4.7}$$
$$dS/dt = -k_1 ES + k_2 C \tag{4.8}$$
$$dC/dt = k_1 ES - (k_2 + k_3)C \tag{4.9}$$
$$dP/dt = k_3 C \tag{4.10}$$

And for a two stage reaction, Equation (4.6), one obtains:

$$dE/dt = -k_1 E(S + P_1) + (k_2 + k_3)(C_1 + C_2) \tag{4.11}$$
$$dS/dt = -k_1 ES + k_2 C_1 \tag{4.12}$$
$$dC_1/dt = k_1 ES - (k_2 + k_3)C_1 \tag{4.13}$$
$$dP_1/dt = -k_1 EP_1 + k_3 C_1 + k_2 C_2 \tag{4.14}$$
$$dC_2/dt = -k_1 EP_1 - (k_2 + k_3)C_2 \tag{4.15}$$
$$P_2/dt = k_3 C_2 \tag{4.16}$$

To solve these ODE systems we used the *deSolve* package [140] within the *R Project* [141].

Non-classical or *anomalous* kinetics arises when diffusion does not provide an adequate mixing of reactants to maintain a well-stirred situation. In this case, kinetics becomes geometry controlled and the rate coefficient k_1 depends on time. In particular, fractal reaction theory predicts a power law decay [88], see Section 1.4.2

$$k_1(t) \sim t^{-h} \quad \text{with} \quad \leq h \leq 1\,. \tag{4.17}$$

So, $h = 0$ corresponds to the classical scenario of constant k_1. We determined the anomalous reaction exponent h by using the relationship [99]

$$k_1 = \frac{d\nu/dt}{ES}\,. \tag{4.18}$$

A linear fit (range: 200...400 time steps) according to $\log t = h \log k_1^0$ yielded h. With $k_1(t)$ replacing the constant k_1 in the system of kinetic ODEs one obtains the time course of concentrations as predicted by fractal-like kinetics.

4.2.3 Results and Discussion

In this study we investigated single [Equation (4.5)] and double [Equation (4.6)] Michaelis-Menten reaction schemes under diffusion and subdiffusion. We define the *productivity* as the yield of fully phosphorylated substrate per initial substrate concentration, i.e. P/S_0 and P_2/S_0, respectively.

Simple Michaelis-Menten Scheme

For this part of the analysis we fixed the reaction probabilities to $p_1 = 0.05$, $p_2 = 0.02$, $p_3 = 0.06$. As discussed above, the reaction probability p_1 can be related to a realistic rate coefficient k_1 by a respective adjustment of R, cf. [124]. We avoided the concomitant, complex calculations because we were interested in generic effects and not in a particular target reaction rate. Empirically, one finds that $k_1 = xp_1$, where the proportionality factor x depends on α and p_1, see e.g. [99]. In practice, we manually tuned x to find a good overlap between simulations and classical or fractal-like kinetics. Figure 4.7 shows for the concentrations of complex C (a) and product P (b) that the data are in excellent agreement with classical kinetics for normal diffusive reactants. Only at short times, when the phantom character of the particles led to a slightly enhanced complex formation, some deviations can be seen in (a). On the other hand, subdiffusive reactants with $\alpha = 0.6$ gave rise to fractal-like kinetics with an heterogeneity exponent $h \approx 0.25$. Again, the agreement between simulations and theory is not perfect for short times, but for intermediate and long times the data follow the prediction very closely.

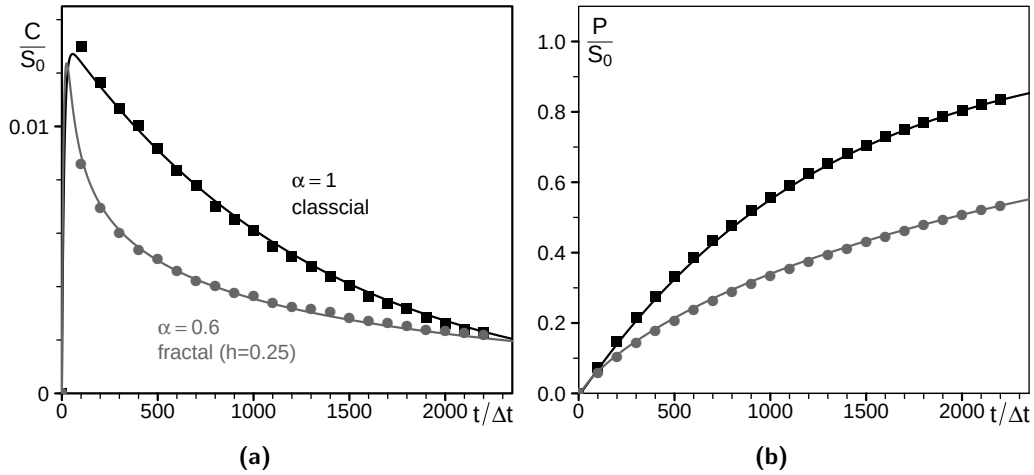

Figure 4.7 The concentrations of complex [C, (a)] and product [P, (b)] for a simple Michaelis-Menten reaction scheme in 3D. The data are compared for normal diffusion and subdiffusion with $\alpha = 0.6$. Normal diffusive reactants give rise to classical kinetics, while the data for subdiffusion correspond to fractal-like kinetics with $h = 0.25$. The amount of output P is always greater for normal diffusive reactants. The reaction probabilities are $p_1 = 0.05$, $p_2 = 0.02$, and $p_3 = 0.06$.

These results strongly support the validity of our approach. By virtue of the simple, empirical relation between p_1 and k_1, our data can be mapped accurately to the mean-field predictions. In particular, for normally diffusing reactants in the bulk, classical kinetics emerged because diffusion is capable of sustaining a

well-stirred system in this case. Subdiffusion, in contrast, implies more compact particle trajectories. This enhanced reactant segregation even in three dimensions and consequently led to anomalous, fractal-like kinetics. In other words, diffusive mixing becomes less effective with lower α.

From Figure 4.7 (b) it is clear that normal diffusion outperforms subdiffusion at all times. This indicates that for the simple Michaelis-Menten scheme the rate of first encounters is the determining factor. Since diffusive mixing works more effectively for $\alpha = 1$ this rate is strongly enhanced as compared to $\alpha = 0.6$.

Double Michaelis-Menten Scheme

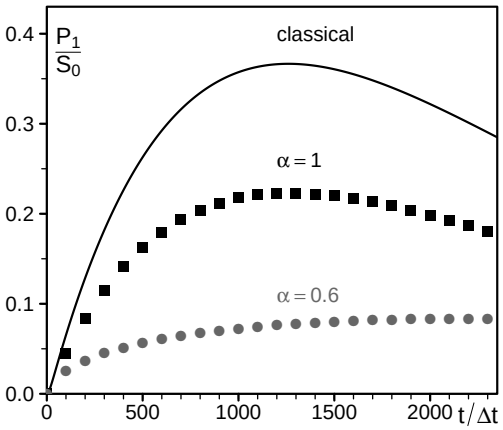

Figure 4.8 The concentration of intermediate product P_1 in a double Michaelis-Menten scheme. With the same reaction probabilities as before (cf. Figure 4.7) strong deviations from the classical behavior occur. Even for normal diffusion the concentration of P_1 is lower due to fast rebinding because P_1 is always produced close to an E. Thus spatio-temporal correlations drastically influence the behavior of a two-stage process.

In the double Michaelis-Menten scheme Equation (4.6) the two stages are concatenated by the irreversible step $C_1 \to P_1 + E$. This implies that the first stage behaves independently of the second. Accordingly we found for C_1 exactly the same course as for C, cf. Figure 4.7. The concentration of P_1, in contrast, deviated strongly from the mean-field results, see Figure 4.8. This highlights the importance of spatio-temporal correlations for multi-stage, diffusion-limited reactions [108]. The classical description neglects these correlations completely and hence is an inaccurate model in this context. In particular, as seen in the figure, the assumption of a constantly well-stirred solution implies a higher concentration of intermediate product P_1 than found in stochastic simulations. This is due to neglecting that P_1 and E are generated close to each other, i.e. their positions are highly correlated in time and space. As a result fast rebinding of E and P_1 is probable and leads to an enhanced decay of P_1 and a faster formation of C_2. For $\alpha = 0.6$ the first stage of the scheme processes more slowly meaning that the concentration of C_1 is lower. Consequently, less P_1 is generated in this case.

From the above discussions it is also clear that the concentrations of C_2 and P_2 showed a drastically changed behavior, see Figure 4.9. Due to the spatio-temporal correlations between E and P_1 their fast rebinding induced an accelerated increase of C_2. For well-mixed reactants the maximum is reached later as the average searching time in the absence of correlations is larger. The compact trajectories of subdiffusive

reactants, in turn, improved the effect of correlations and $C_2(\alpha = 0.6)$ even exceeded the value for normal diffusion at short times.

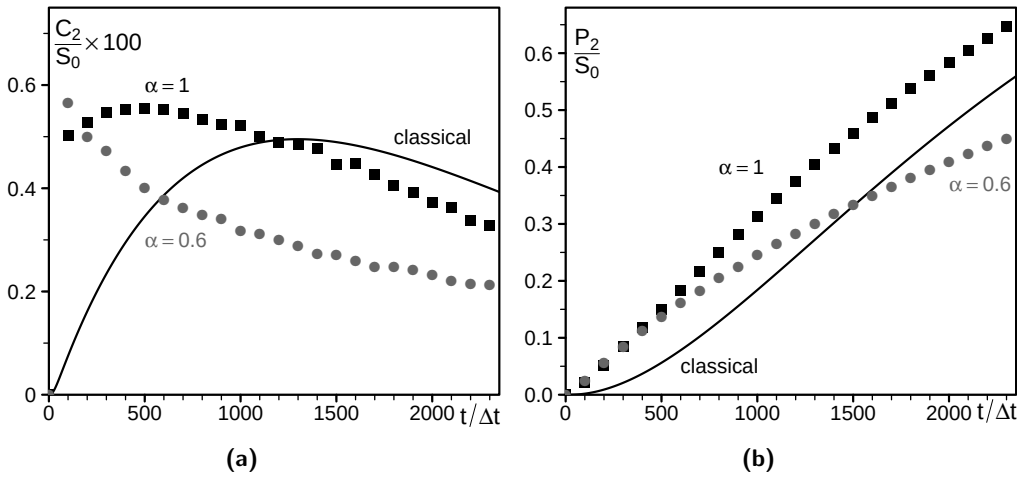

Figure 4.9 The concentrations of the second complex, C_2 (a), and the final product, P_2 (b), of a double Michaelis-Menten reaction scheme in 3D. The reaction probabilities are $p_1 = 0.05$, $p_2 = 0.02$, and $p_3 = 0.10$. As for P_1 also normal diffusive reactants give rise to a pronounced discrepancy between stochastic simulations and the deterministic ODEs. Due the fast rebinding events C_1 reaches its maximum faster. For subdiffusion this effect is further enhanced so that at short times more C_2 is generated as in case of normal diffusion. The concentration of output P_2 shows only small differences between $\alpha = 1$ and $\alpha = 0.6$ for $t < 500$. Consequently, although subdiffusion yields less P_1, the full process works as efficiently as in case of diffusion.

For times $t < 500\,\Delta t$, the amount of P_2 is almost equal for diffusive and subdiffusive reactants. This corresponds to the similar concentrations of C_2 in this regime. Subdiffusion promotes the fast rebinding of reactants so that a smaller number of intermediate product P_1 can still yield an equal or even larger amount of final product P_2. Figure 4.9 (b) shows P_2 for the reaction probabilities $p_1 = 0.05$, $p_2 = 0.02$, $p_3 = 0.10$, i.e. in comparison to production of P_1 the dissociation of C_2 into E and P_1 is less probable. We varied p_2 and p_3 in the range $0.02 \ldots 0.10$ to study the interplay of production and dissociation. As an observable we chose the ratio between the concentrations P_2 for normal diffusion and subdiffusion ($\alpha = 0.6$):

$$\xi(t;\alpha) \equiv \frac{P_2(t;\alpha = 0.6)}{P_2(t;\alpha = 1} \tag{4.19}$$

In Figure 4.10 $\xi(t;\alpha = 0.6)$ is plotted for nine combinations of p_2 and p_3. The example discussed in Figure 4.9 corresponds to the upper right field showing only a short period where subdiffusion yielded more P_2 than normal diffusion as indicated

by the gray shaded area. Decreasing p_2 and/or increasing p_3 in general increased the advantage of subdiffusion. The strongest effect was perceived for $p_2 = 0.10$ and $p_3 = 0.02$ (lower left plot). When C_2 is a rather fragile entity, the repetitive binding of P_1 and E becomes an increasingly important process on the way to P_2. For subdiffusive reactants the probability that just dissociated P_1 and E stay close to each other and again merge to a C_2 is enhanced due to their more compact trajectories. On the other hand, when the conversion from C_2 to P_2 works efficiently (large p_3) the formation of *new* reactive pairs is the limiting step. This is determined by the replenishing of P_1, that is faster for normal diffusive reactants as discussed before. As soon as all close P_1-E pairs have vanished in favor of P_2, the diffusive search process becomes limiting and hence for longer time scales normal diffusion exhibits a greater productivity. In other words, for subdiffusive reactants the pool of reactive pairs is exhausted with high efficiency but only slowly replenished.

The central question is hence for which parameter ranges subdiffusive reactants render the process more efficient, i.e. $\xi > 1$. Consequently, we reduced Equation (4.19) to a single number by taking the average deviation from unity over the interval $10^1 \ldots t_{\mathrm{av}} = 10^3\,\Delta t$ as indicated by the dotted lines in Figure 4.10:

$$\langle \delta\xi \rangle(\alpha) = \frac{1}{t_{\mathrm{av}} - 10} \sum_{10}^{t_{\mathrm{av}}} \left[\xi(t'; \alpha) - 1 \right] dt' \tag{4.20}$$

With this we constructed a phase diagram of the relative productivity in dependence on the reaction probabilities p_2 and p_3 while $p_1 = 0.05$ was fixed, see Figure 4.11. The two regimes where subdiffusion/diffusion performed more efficiently were characterized by positive/negative values of $\langle \delta\xi \rangle$. As discussed above, frequent dissociations of C_2 and slow production of P_2 render subdiffusion the more productive search process. Figure 4.11 is an linearly interpolated heat map based on the nine combinations (p_2, p_3) discussed in Figure 4.10 the transition between the scenarios appeared quite smooth at the given resolution.

4.2.4 Summary and Conclusions

In this study, the impact of viscoelastic subdiffusion on typical enzymatic reactions has been investigated. For the following discussions we consider the single and double phosphorylation of a protein S by a kinase E as a realization of this scenario. For a simple phosphrylation [Equation (4.5)] the lower first encounter rate of subdiffuive reactants led to less production of active P – independently of the particular values of p_2 and p_3. In this scenario, the greater compactness of the subdiffusive trajectories caused a macroscopic segregation of reactants due to initial density fluctuations, i.e. the Zeldovich effect, cf. Section 1.4.2 and Section 4.1.3. Indeed, the behavior is well described by fractal-like kinetics (see Figure 4.7) implying that viscoelastic subdiffusion yields qualitatively the same effects as diffusion on a fractal support that is discussed in [99].

In the context of geometry-controlled kinetics (cf. Section 1.4.2 and [97]) the reaction rate strongly depends on the initial distance between E and S if the diffusion

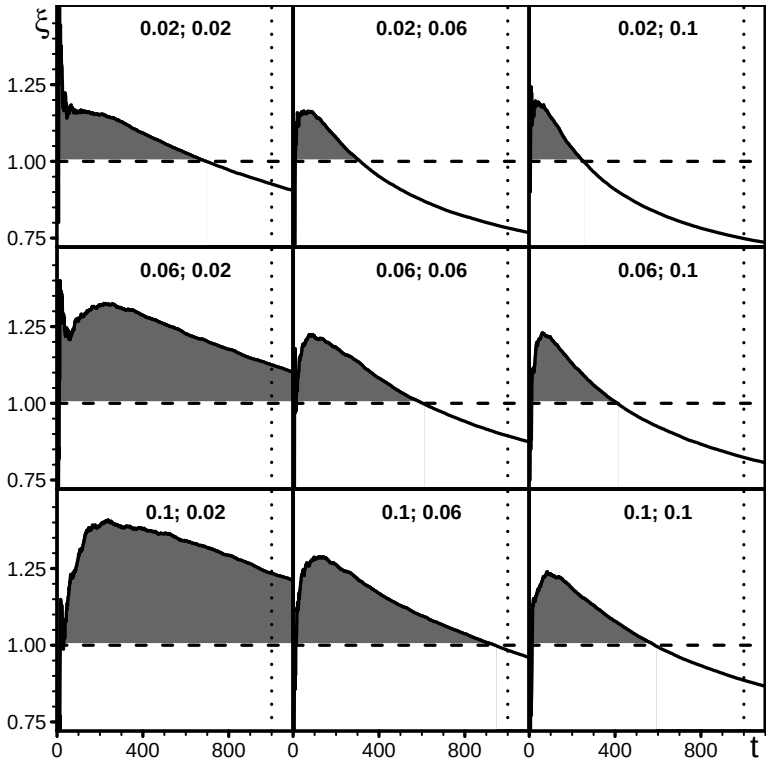

Figure 4.10 Course of the ratio ξ [Equation (4.19)] between the yield of P_2 in the diffusion and subdiffusion scenario. Each of the nine plots corresponds to a particular combination of the dissociation and production probabilities as indicated by the numbers: "p_2; p_3". The gray shaded area visualizes the (transiently) enhanced productivity of subdiffusion ($\xi > 1$) and the dotted line indicates the upper limit for the temporal average $t_{\mathrm{av}} = 10^3\,\Delta t$ in Equation (4.20).

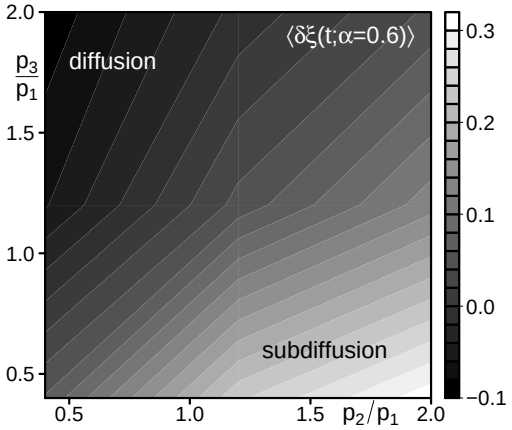

Figure 4.11 Phase diagram of reaction productivity in terms of $\langle \delta\xi \rangle (p_2; p_3)$. The figure resembles an interpolated heat map for the nine scenarios shown in Figure 4.10. The two regimes where either subdiffusion or diffusion dominate are visible as bright and dark hue, respectively.

process samples space in a compact fashion, i.e. $d_W < d_f$. Here we have $d_f = 3$ and our scenarios correspond to the compact ($\alpha = 0.6 \Rightarrow d_W = 3.33$) and non-compact ($\alpha = 1 \Rightarrow d_W = 2$) exploration regime. In the latter case, we found the anticipated classical kinetics with a constant rate coefficient k_1. The former case, in contrast, exhibited rather $k_1(t) \sim t^{-h}$. In the beginning the reaction is fast because the kinases find the abundant substrates after traveling only a short distance. As a substantial amount of substrate is consumed, the average distance between S and E grows since diffusion cannot sustain the initially well-mixed configuration if sampling process is compact. Consequently the rate coefficient decays with time.

The double phosphorylation reaction [Equation (4.6)] showed a more complex behavior and strong deviations from the mean-field description that relies on kinetic ODEs of global concentrations, cf. Figure 4.8 and Figure 4.9. The reason for the altered behavior are the spatio-temporal correlations between the positions of E and P_1 that promote a fast rebinding. These correlations are fully neglected in the framework of kinetic ODEs. Our findings are in qualitative agreement with recent studies which show that the spatio-temporal correlations in full-stochastic reaction-diffusion simulations bear unexpected behavior like the breakdown of bistability in a double phosphorylation cycle [108].

Subdiffusive reactants enhanced the effect of fast rebinding, i.e. spatio-temporal correlations become even more important. In the framework of geometry-controlled kinetics, the reaction is more effective if the separation between E and P_1 is small. Our data show that for a two-stage process subdiffusive reactants may even enhance the overall efficiency compared to the scenario of normal diffusion. Hence, subdiffusion does not necessarily slow down and hamper biochemical processes but can even provide a strategy to effectively exploit spatio-temporal correlations.

Chapter 5

Conclusions and Perspectives

5.1 The Mechanism Behind Crowding-induced Subdiffusion

In the work at hand the underlying dynamics of crowding-induced subdiffusion have been investigated by means of computer simulations. The presented results show that the typically applied methods for obtaining the diffusion anomaly α from experimental data provide consistent estimates. This also includes the recently proposed p variation method [77]. Moreover the results of SPT and FCS experiments agree, independently whether the underlying dynamics corresponds to the FBM or the OD model.

The influence of measurement uncertainties inherent to SPT experiments can lead to wrong interpretations like apparent subdiffusion in a system where tracers diffuse normally [27]. Our results suggest that these problems extend to the determination of the underlying random process by commonly applied methods. In particular, blurring of CTRW trajectories can mask weak ergodicity breaking, i.e. the distinct scaling of time- and ensemble-averaged MSD. In general, positional blur of SPT data leads to a systematic underestimation of α. Since even advanced devices suffer from substantial uncertainties if the tracked particle moves fast, the effects of measurement errors should always be addressed in the analysis of SPT data.

Aiming at a criterion to distinguish between different models for crowding-induced subdiffusion we investigated the average shape of SPT trajectories. Simulations reveal that the frequently proposed models CTRW, FBM, and OD yield quite different correlations between α and the asphericity A of the trajectories. Furthermore, this applies to "apparent subdiffusion" of normal diffusive tracers due to measurement errors. Hence, by measuring the pair of values (A,α) and comparing it to theory (simulations) one can in principle judge which model describes the experimental data best. We applied this method on tracer diffusion in dense dextran solutions. The measurement uncertainties limited the analysis to times $t > 100$ ms where diffusion was normal. Accordingly, shape and anomaly deviated only weakly from a random walk. Future work will consequently focus on other experimental systems like lysozyme solutions that exhibit subdiffusion on longer time scales.

In a complementary bottom-up approach a particle-based model of the cytoplasm was designed to isolate the minimum prerequisites for subdiffusion to occur on time scales accessible by SPT and FCS experiments. Soft-core repulsion and weak

attraction between spherical particles (proteins) was implemented. For this setting we only observed transient subdiffusion on short time scales. Further work on an improved model should probably consider explicit bonds between the proteins. Following a recent model for gelation [75] finite valencies and geometrical aspects can give rise to a MSD that is evocative for a tracer in a viscoelastic medium. Thus, by adequately choosing the parameters, a particle-based system which exhibits FBM-like subdiffusion could emerge. Another possible modification would be to include more details of the proteins' geometry: A recent model of the bacterial cytoplasm that accounts for the precise structure of numerous proteins indeed shows subdiffusion [142].

In summary, our projects complement important aspects to the constantly growing knowledge about crowding-induced subdiffusion. With respect to the underlying mechanism, however, a conclusive answer is still lacking. In this respect a standard protocol for the analysis of SPT experiments is desirable. Standardized experiments on subdiffusion could in turn, inspire coarse-grained models that help to understand the microscopic architecture of crowded fluids in general and the cytoplasm in particular.

5.2 Diffusion-controlled Reactions in Crowded Fluids

The second part of this work focused on the impact of subdiffuion on biochemical kinetics. So far, the analysis of subdiffusion-reaction systems widely relied on the OD and CTRW scenarios. Inspired by the growing evidence that viscoelasticity gives rise to subdiffusion in many crowded fluids, including the cytoplasm, and cellular membranes we applied FBM to generate reactant trajectories. In agreement with the literature on CTRW and OD we found an enhanced segregation of reactants and a concomitant, strongly anomalous kinetics for the prototypic reaction $A + B \rightarrow C$.

Since FBM is introduced as an external, stochastic force that drives the motion of the particles, the fluctuation-dissipation relation does not hold. This reduces the computational efforts but also prohibits the implementation of deterministic interactions like repulsion or attraction between particles. Despite these limitations the observed behavior is consistent with the existing literature on reaction-subdiffusion. Hence in the absence of inter-particle forces our method is a valid and efficient approach for full stochastic simulations of subdiffusive reactants.

In a next step we applied this method to a double Michaelis-Menten reaction scheme that is realized, for example, in the double phosphorylation of MAPK. Due to an intermediate dissociation-association event of the reactants spatio-temporal correlations dramatically change the overall process as compared to classical (mean-field) theories. These findings also hold for normal diffusion (cf. [108]) but subdiffusion enhances the effect as the more compact trajectories facilitate fast rebinding. Ultimately, subdiffusive reactants can even increase the overall productivity of the reaction.

In all, this study extends the picture of subdiffusion-reaction systems: Subdiffusive

proteins do not necessarily impair biochemical processes but may even improve the efficiency when spatio-temporal correlations can be exploited. Since the assumptions of the mean-field description are not fulfilled, (anomalous) transport of reactants has to be considered explicitly to obtain correct predictions in such situations. Future work will address further biologically relevant scenarios like reactions at the interface of membrane and cytoplasm [143] or subdiffusion-limited formation of gradients [144].

Literature

[1] Alberts, B., Johnson, A., Lewis, J., Raff, M., Roberts, K., and Walter, P. (Editors). *Molecular biology of the cell.* Garland, New York, fourth edition (2002).

[2] Ruiz-Mirazo, K., Peretó, J., and Moreno, A. *A Universal Definition of Life: Autonomy and Open-ended Evolution. Origins of Life and Evolution of the Biosphere*, **34**, 323 (2004).

[3] Park, S. and Agmon, N. *Theory and Simulation of Diffusion-Controlled Michaelis-Menten Kinetics for a Static Enzyme in Solution. The Journal of Physical Chemistry B*, **112**, 5977 (2008).

[4] Grima, R. *Noise-Induced Breakdown of the Michaelis-Menten Equation in Steady-State Conditions. Physical Review Letters*, **102**, 218103 (2009).

[5] Hanahan, D. and Weinberg, R. A. *The Hallmarks of Cancer. Cell*, **100**, 57 (2000).

[6] Kholodenko, B. N. *Cell-signalling dynamics in time and space. Nature Reviews Molecular Cell Biology*, **7**, 165 (2006).

[7] Lemmon, M. A. and Schlessinger, J. *Cell Signaling by Receptor Tyrosine Kinases. Cell*, **141**, 1117 (2010).

[8] Chang, L. and Karin, M. *Mammalian MAP kinase signalling cascades. Nature*, **410**, 37 (2001).

[9] Salazar, C. and Höfer, T. *Multisite protein phosphorylation–from molecular mechanisms to kinetic models. The FEBS Journal*, **276**, 3177 (2009).

[10] Ferrell, J. E. and Machleder, E. M. *The Biochemical Basis of an All-or-None Cell Fate Switch in Xenopus Oocytes. Science*, **280**, 895 (1998).

[11] Huang, C. Y. and Ferrell, J. E. *Ultrasensitivity in the mitogen-activated protein kinase cascade. Proceedings of the National Academy of Sciences*, **93**, 10078 (1996).

[12] Higham, D. J. *Modeling and Simulating Chemical Reactions. SIAM Review*, **50**, 347 (2008).

[13] Wilkinson, D. J. *Stochastic modelling for quantitative description of heterogeneous biological systems. Nature Reviews Genetics*, **10**, 122 (2009).

[14] Ellis, J. R. *Macromolecular crowding: obvious but underappreciated. Trends in Biochemical Sciences*, **26**, 597 (2001).

[15] Fulton, A. B. *How Crowded Is The Cytoplasm. Cell*, **30**, 345 (1982).

[16] Ellis, J. R. and Minton, A. P. *Join the crowd. Nature*, **425**, 27 (2003).

[17] Dupuy, A. D. and Engelman, D. M. *Protein area occupancy at the center of the red blood cell membrane. Proceedings of the National Academy of Sciences*, **105**, 2848 (2008).

[18] Zhou, H. X., Rivas, G., and Minton, A. P. *Macromolecular Crowding and Confinement: Biochemical, Biophysical, and Potential Physiological Consequences. Annual Review of Biophysics*, **37**, 375 (2008).

[19] Einstein, A. *Über die von der molekularkinetischen Theorie der Wärme geforderte Bewegung von in ruhenden Flüssigkeiten suspendierten Teilchen. Annalen der Physik*, **322**, 549 (1905).

[20] Metzler, R. and Klafter, J. *The Random Walk's Guide to Anomalous Diffusion: A Fractional Dynamics Approach. Physics Reports*, **339**, 1 (2000).

[21] Weiss, M. and Nilsson, T. *In a mirror dimly: tracing the movements of molecules in living cells. Trends in Cell Biology*, **14**, 267 (2004).

[22] Weiss, M. *Probing the Interior of Living Cells with Fluorescence Correlation Spectroscopy. Annals of the New York Academy of Sciences*, **1130**, 21 (2008).

[23] Malchus, N. and Weiss, M. *Elucidating Anomalous Protein Diffusion in Living Cells with Fluorescence Correlation Spectroscopy – Facts and Pitfalls. Journal of Fluorescence*, **20**, 19 (2010).

[24] Szymanski, J. and Weiss, M. *Elucidating the Origin of Anomalous Diffusion in Crowded Fluids. Physical Review Letters*, **103**, 038102 (2009).

[25] Weiss, M., Elsner, M., Kartberg, F., and Nilsson, T. *Anomalous Subdiffusion Is a Measure for Cytoplasmic Crowding in Living Cells. Biophysical Journal*, **87**, 3518 (2004).

[26] Saxton, M. J. and Jacobson, K. *Single Particle Tracking: Applications to Membrane Dynamics. Annual Review of Biophysics and Biomolecular Structure*, **26**, 373 (1997).

[27] Martin, D. S., Forstner, M. B., and Käs, J. A. *Apparent Subdiffusion Inherent to Single Particle Tracking. Biophysical Journal*, **83**, 2109 (2002).

[28] Schütz, G. J., Schindler, H., and Schmidt, T. *Single-molecule microscopy on model membranes reveals anomalous diffusion. Biophysical Journal*, **73**, 1073 (1997).

[29] Saxton, M. J. *Single-particle tracking: connecting the dots. Nature Methods*, **5**, 671 (2008).

[30] Enderlein, J. *Tracking of fluorescent molecules diffusing within membranes. Applied Physics B: Lasers and Optics*, **71**, 773 (2000).

[31] McHale, K., Berglund, A. J., and Mabuchi, H. *Quantum Dot Photon Statistics Measured by Three-Dimensional Particle Tracking. Nano Letters*, **7**, 3535 (2007).

[32] Qian, H., Sheetz, M. P., and Elson, E. L. *Single particle tracking. Analysis of diffusion and flow in two-dimensional systems. Biophysical Journal*, **60**, 910 (1991).

[33] Saxton, M. J. *Lateral diffusion in an archipelago. Single-particle diffusion. Biophysical Journal*, **64**, 1766 (1993).

[34] Saxton, M. J. *Single-particle tracking: the distribution of diffusion coefficients. Biophysical Journal*, **72**, 1744 (1997).

[35] Guigas, G., Kalla, C., and Weiss, M. *Probing the Nanoscale Viscoelasticity of Intracellular Fluids in Living Cells. Biophysical Journal*, **93**, 316 (2007).

[36] Golding, I. and Cox, E. C. *Physical Nature of Bacterial Cytolasm. Physical Review Letters*, **96**, 098102 (2006).

[37] Tolić-Nørrelykke, I. M., Munteanu, E. L., Thon, G., Oddershede, L., and Sorensen, K. B. *Anomalous Diffusion in Living Yeast Cells. Physical Review Letters*, **93**, 078102 (2004).

[38] Wachsmuth, M., Waldeck, W., and Langowski, J. *Anomalous diffusion of fluorescent probes inside living cell nuclei investigated by spatially-resolved fluorescence correlation spectroscopy. Journal of Molecular Biology*, **298**, 677 (2000).

[39] Bancaud, A., Huet, S., Daigle, N., Mozziconacci, J., Beaudouin, J., and Ellenberg, J. *Molecular crowding affects diffusion and binding of nuclear proteins in heterochromatin and reveals the fractal organization of chromatin. EMBO Journal*, **28**, 3785 (2009).

[40] Banks, D. S. and Fradin, C. *Anomalous Diffusion of Proteins Due to Molecular Crowding. Biophysical Journal*, **89**, 2960 (2005).

[41] Mason, T. G. and Weitz, D. A. *Optical Measurements of Frequency-Dependent Linear Viscoelastic Moduli of Complex Fluids. Physical Review Letters*, **74**, 1250 (1995).

[42] Sprakel, J., van der Gucht, J., Cohen Stuart, M. A., and Besseling, N. A. M. *Rouse Dynamics of Colloids Bound to Polymer Networks. Physical Review Letters*, **99**, 208301 (2007).

[43] Sprakel, J., van der Gucht, J., Cohen Stuart, M. A., and Besseling, N. A. M. *Brownian particles in transient polymer networks. Physical Review E*, **77**, 061502 (2008).

[44] Pan, W., Filobelo, L., Pham, N. D. Q., Galkin, O., Uzunova, V. V., and Vekilov, P. G. *Viscoelasticity in Homogeneous Protein Solutions. Physical Review Letters*, **102**, 058101 (2009).

[45] Goins, A. B., Sanabria, H., and Waxham, M. N. *Macromolecular Crowding and Size Effects on Probe Microviscosity. Biophysical Journal*, **95**, 5362 (2008).

[46] Dix, J. A. and Verkman, A. S. *Crowding Effects on Diffusion in Solutions and Cells. Annual Review of Biophysics*, **37**, 247 (2008).

[47] Weiss, M., Hashimoto, H., and Nilsson, T. *Anomalous Protein Diffusion in Living Cells as Seen by Fluorescence Correlation Spectroscopy. Biophysical Journal*, **84**, 4043 (2003).

[48] Malchus, N. and Weiss, M. *Anomalous Diffusion Reports on the Interaction of Misfolded Proteins with the Quality Control Machinery in the Endoplasmic Reticulum. Biophysical Journal*, **99**, 1321 (2010).

[49] Horton, M. R., Hofling, F., Radler, J. O., and Franosch, T. *Development of anomalous diffusion among crowding proteins. Soft Matter*, **6**, 2648 (2010).

[50] Harland, C. W., Bradley, M. J., and Parthasarathy, R. *Phospholipid bilayers are viscoelastic. Proceedings of the National Academy of Sciences*, **107**, 19146 (2010).

[51] Grimmett, G. R. and Stirzaker, D. R. *Probability and Random Processes.* Oxford University Press, Oxford, New York, third edition (2006).

[52] Falconer, K. *Fractal Geometry – Mathematical Foundations and Applications.* John Wiley & Sons Ltd., Chichester, UK (2003).

[53] Landau, L. D. and Lifshitz, E. M. *Fluid Mechanics*, volume 6 of *Course of Theoretical Physics.* Butterworth-Heinemann, Oxford (UK), Burlington (USA), second edition (2006).

[54] Bouchaud, J. P. *Weak ergodicity breaking and aging in disordered systems. Journal de Physique I France*, **2**, 1705 (1992).

[55] Metzler, R. and Klafter, J. *The restaurant at the end of the random walk: recent developments in the description of anomalous transport by fractional dynamics. Journal of Physics A: Mathematical and General*, **37**, R161 (2004).

[56] Bel, G. and Barkai, E. *Weak Ergodicity Breaking in the Continuous-Time Random Walk. Physical Review Letters*, **94**, 240602 (2005).

[57] He, Y., Burov, S., Metzler, R., and Barkai, E. *Random Time-Scale Invariant Diffusion and Transport Coefficients. Physical Review Letters*, **101**, 058101 (2008).

[58] Lubelski, A., Sokolov, I. M., and Klafter, J. *Nonergodicity Mimics Inhomogenety in Single Particle Tracking. Physical Review Letters*, **100**, 250602 (2008).

[59] Rebenshtok, A. and Barkai, E. *Distribution of Time-Averaged Observables for Weak Ergodicity Breaking. Physical Review Letters*, **99** (2007).

[60] Mandelbrot, B. B. and van Ness, J. W. *Fractional Brownian Motions, Fractional Noises and Applications. SIAM Review*, **10**, 422 (1968).

[61] Sebastian, K. L. *Path integral representation for fractional Brownian motion. Journal of Physics A: Mathematical and General*, **28**, 4305 (1995).

[62] Hipel, K. W. and McLeod, A. I. *Time series Modelling of Water Resources and Environmental Systems.* Elsevier, Amsterdam (1994).

[63] Molz, F. J., Liu, H. H., and Szulga, J. *Fractional Brownian Motion and Fractional Gaussian Noise in Subsurface Hydrology: A Review, Presentation of Fundamental Properties, and Extensions. Water Resources Research*, **33**, 2273 (1997).

[64] Deng, W. and Barkai, E. *Ergodic properties of fractional Brownian-Langevin motion. Physical Review E*, **79**, 011112 (2009).

[65] Goychuk, I. *Viscoelastic subdiffusion: From anomalous to normal. Physical Review E*, **80**, 046125 (2009).

[66] Lutz, E. *Fractional Langevin equation. Physical Review E*, **64**, 051106 (2001).

[67] Burov, S. and Barkai, E. *Fractional Langevin equation: Overdamped, underdamped, and critical behaviors. Physical Review E*, **78**, 031112 (2008).

[68] Havlin, S. and Ben-Avraham, D. *Diffusion in disordered media. Advances in Physics*, **36**, 695 (1987).

[69] Bouchaud, J.-P. and Georges, A. *Anomalous diffusion in disordered media: Statistical mechanisms, models and physical applications. Physics Reports*, **195**, 127 (1990).

[70] Stauffer, D. *Scaling theory of percolation clusters. Physics Reports*, **54**, 1 (1979).

[71] Saxton, M. J. *Anomalous Diffusion Due to Obstacles: A Monte Carlo Study. Biophysical Journal*, **66**, 394 (1994).

[72] Newman, M. E. J. and Ziff, R. M. *Efficient Monte Carlo Algorithm and High-Precision Results for Percolation. Physical Review Letters*, **85**, 4104 (2000).

[73] Kubo, R. *The fluctuation-dissipation theorem. Reports on Progress in Physics*, **29**, 255 (1966).

[74] Gemant, A. *A Method of Analyzing Experimental Results Obtained from Elasto-Viscous Bodies. Physics*, **7**, 311 (1936).

[75] Hurtado, P. I., Berthier, L., and Kob, W. *Heterogeneous Diffusion in a Reversible Gel. Physical Review Letters*, **98**, 135503 (2007).

[76] Stauffer, D., Schulze, C., and Heermann, D. *Superdiffusion in a Model for Diffusion in a Molecularly Crowded Environment. Journal of Biological Physics*, **33**, 305 (2007).

[77] Magdziarz, M., Weron, A., Burnecki, K., and Klafter, J. *Fractional Brownian Motion Versus the Continuous-Time Random Walk: A Simple Test for Subdiffusive Dynamics. Physical Review Letters*, **103**, 180602 (2009).

[78] Tejedor, V., Bénichou, O., Voituriez, R., Jungmann, R., Simmel, F., Selhuber-Unkel, C., Oddershede, L. B., and Metzler, R. *Quantitative Analysis of Single Particle Trajectories: Mean Maximal Excursion Method. Biophysical Journal*, **98**, 1364 (2010).

[79] Jeon, J.-H., Tejedor, V., Burov, S., Barkai, E., Selhuber-Unkel, C., Berg-Sørensen, K., Oddershede, L., and Metzler, R. *In Vivo Anomalous Diffusion and Weak Ergodicity Breaking of Lipid Granules. Physical Review Letters*, **106**, 048103 (2011).

[80] Condamin, S., Tejedor, Voituriez, Bénichou, O., and Klafter, J. *Probing microscopic origins of confined subdiffusion by first-passage observables. Proceedings of the National Academy of Sciences*, **105**, 5675 (2008).

[81] Burov, S., Jeon, J.-H., Metzler, R., and Barkai, E. *Single particle tracking in systems showing anomalous diffusion: the role of weak ergodicity breaking. Phys. Chem. Chem. Phys.*, **13**, 1800 (2011).

[82] von Smoluchowski, M. *Versuch einer mathematischen Theorie der Koagulationskinetik kolloider Lösungen. Zeitung für Physikalische Chemie*, **92**, 129 (1917).

[83] Chandrasekhar, S. *Stochastic Problems in Physics and Astronomy. Rev. Mod. Phys.*, **15**, 1 (1943).

[84] Keizer, J. *Nonequilibrium statistical thermodynamics and the effect of diffusion on chemical reaction rates. The Journal of Physical Chemistry*, **86**, 5052 (1982).

[85] Szabo, A. *Theory of diffusion-influenced fluorescence quenching. The Journal of Physical Chemistry*, **93**, 6929 (1989).

[86] de Gennes, P. G. *Kinetics of diffusion-controlled processes in dense polymer systems. I. Nonentangled regimes. The Journal of Chemical Physics*, **76**, 3316 (1982).

[87] Montroll, E. W. and Weiss, G. H. *Random Walks on Lattices. II. Journal of Mathematical Physics*, **6**, 167 (1965).

[88] Kopelman, R. *Fractal Reaction Kinetics. Science*, **241**, 1620 (1988).

[89] Ovchinnikov, A. and Zeldovich, Y. B. *Role of density fluctuations in bimolecular reaction kinetics. Chemical Physics*, **28**, 215 (1978).

[90] Toussaint, D. and Wilczek, F. *Particle–antiparticle annihilation in diffusive motion. The Journal of Chemical Physics*, **78**, 2642 (1983).

[91] Argyrakis, P., Kopelman, R., and Lindenberg, K. *Diffusion-limited binary reactions: the hierarchy of nonclassical regimes for random initial conditions. Chemical Physics*, **177**, 693 (1993).

[92] Lin, A., Kopelman, R., and Argyrakis, P. *Nonclassical kinetics in three dimensions: Simulations of elementary A+B and A+A reactions. Physical Review E*, **53**, 1502 (1996).

[93] Bramson, M. and Lebowitz, J. L. *Asymptotic Behavior of Densities in Diffusion-Dominated Annihilation Reactions. Physical Review Letters*, **61**, 2397 (1988).

[94] Lindenberg, K., West, B. J., and Kopelman, R. *Steady-state segregation in diffusion-limited reactions. Physical Review Letters*, **60**, 1777 (1988).

[95] Klages, R., Radons, G., and Sokolov, I. M. (Editors). *Anomalous Transport: Foundations and Applications.* Wiley-VCH Verlag GmbH & Co. KGaA, Weinheim (2008).

[96] Condamin, S., Bénichou, O., Tejedor, V., Voituriez, R., and Klafter, J. *First-passage times in complex scale-invariant media. Nature*, **450**, 77 (2007).

[97] Bénichou, O., Chevalier, C., Klafter, J., Meyer, B., and Voituriez, R. *Geometry-controlled kinetics. Nature Chemistry*, **2**, 472 (2010).

[98] Saxton, M. J. *Lateral Diffusion in an Archipelago. The Effect od Mobile Obstacles. Biophysical Journal*, **52**, 989 (1987).

[99] Berry, H. *Monte Carlo Simulations of Enzyme Reactions in Two Dimensions: Fractal Kinetics and Spatial Segregation. Biophysical Journal*, **83**, 1891 (2002).

[100] Grima, R. and Schnell, S. *A systematic investigation of the rate laws valid in intracellular environments. Biophysical Chemistry*, **124**, 1 (2006).

[101] Kopelman, R., Klymko, P. W., Newhouse, J. S., and Anacker, L. W. *Reaction kinetics on fractals: Random-walker simulations and excition experiments. Physical Review B*, **29**, 3747 (1984).

[102] Shi, Z. Y. and Kopelman, R. *Nonclassical kinetics and reaction probability for bimolecular reactions in low-dimensional media. The Journal of Physical Chemistry*, **96**, 6858 (1992).

[103] Elcock, A. H. *Models of macromolecular crowding effects and the need for quantitative comparisons with experiment. Current Opinion in Structural Biology*, **20**, 196 (2010).

[104] Kim, J. S. and Yethiraj, A. *Effect of Macromolecular Crowding on Reaction Rates: A Computational and Theoretical Study. Biophysical Journal*, **96**, 1333 (2009).

[105] Ridgway, D., Broderick, G., Campistrous, A. L., Ru'aini, M., Winter, P., Hamilton, M., Boulanger, P., Kovalenko, A., and Ellison, M. J. *Coarse-Grained Molecular Simulation of Diffusion and Reaction Kinetics in a Crowded Virtual Cytoplasm. Biophysical Journal*, **94**, 3748 (2008).

[106] Grima, R., Yaliraki, S. N., and Barahona, M. *Crowding-Induced Anisotropic Transport Modulates Reaction Kinetics in Nanoscale Porous Media. The Journal of Physical Chemistry B*, **114**, 5380 (2010).

[107] Weber, S. C., Spakowitz, A. J., and Theriot, J. A. *Bacterial Chromosomal Loci Move Subdiffusively through a Viscoelastic Cytoplasm. Physical Review Letters*, **104**, 238102 (2010).

[108] Takahashi, K., Tănase-Nicola, S., and ten Wolde, P. R. *Spatio-temporal correlations can drastically change the response of a MAPK pathway. Proceedings of the National Academy of Sciences*, **107**, 2473 (2010).

[109] Landau, D. P. and Binder, K. *A Guide to Monte Carlo Simulations in Statistical Physics*. Cambridge University Press, Cambridge, UK, second edition (2005).

[110] Binder, K. and Heermann, D. W. *Monte Carlo Simulation in Statistical Physics*. Springer, Heidelberg, Dordrecht, London New York, fifth edition (2010).

[111] Majid, I., Avraham, D. B., Havlin, S., and Stanley, H. E. *Exact-enumeration approach to random walks on percolation clusters in two dimensions. Physical Review B*, **30**, 1626 (1984).

[112] Dieker, A. B. *Simulation of fractional Brownian motion.* Master's thesis, Vrije Universiteit Amsterdam (2002).

[113] Wood, A. T. A. and Chan, G. *Simulation of Stationary Gaussian Processes in $[0,1]_d$. Journal of Computational and Graphical Statistics*, **3**, 409 (1994).

[114] Davies, R. B. and Harte, D. S. *Tests for Hurst effect. Biometrika*, **74**, 95 (1987).

[115] Berry, M. V. and Lewis, Z. V. *On the Weierstrass-Mandelbrot Fractal Function. Proceedings of the Royal Society of London. A. Mathematical and Physical Sciences*, **370**, 459 (1980).

[116] Saxton, M. J. *Anomalous Subdiffusion in Flourescence Photobleaching Recovery: A Monte Carlo Study. Biophysical Journal*, **81**, 2226 (2001).

[117] Guigas, G. and Weiss, M. *Sampling the Cell with Anomalous Diffusion – The Discovery of Slowness. Biophysical Journal*, **94**, 90 (2008).

[118] Turner, T., Schnell, S., and Burrage, K. *Stochastic approaches for modelling in vivo reactions. Computational Biology and Chemistry*, **28**, 165 (2004).

[119] Gillespie, D. T. *Exact stochastic simulation of coupled chemical reactions. The Journal of Physical Chemistry*, **81**, 2340 (1977).

[120] Gillespie, D. T. *The chemical Langevin equation. The Journal of Chemical Physics*, **113**, 297 (2000).

[121] van Zon, J. S. and ten Wolde, P. R. *Green's-function reaction dynamics: A particle-based approach for simulating biochemical networks in time and space. The Journal of Chemical Physics*, **123**, 234910 (2005).

[122] Oppelstrup, T., Bulatov, V. V., Donev, A., Kalos, M. H., Gilmer, G. H., and Sadigh, B. *First-passage kinetic Monte Carlo method. Physical Review E*, **80**, 066701 (2009).

[123] Opplestrup, T., Bulatov, V. V., Gilmer, G. H., Kalos, M. H., and Sadigh, B. *First-Passage Monte Carlo Algorithm: Diffusion without All the Hops. Physical Review Letters*, **97**, 230602 (2006).

[124] Erban, R. and Chapman, S. J. *Stochastic modelling of reaction-diffusion processes: algorithms for bimolecular reactions. Physical biology*, **6**, 046001 (2009).

[125] McLeod, A. I., Yu, H., and Krougly, Z. L. *Algorithms for Linear Time Series Analysis: With R Package. Journal of Statistical Software*, **23**, 1 (2007).

[126] Rudnick, J. and Gaspari, G. *The Shapes of Random Walks. Science*, **237**, 384 (1987).

[127] Šolc, K. *Shape of a Random-Flight Chain. The Journal of Chemical Physics*, **55**, 335 (1971).

[128] Rudnick, J. and Gaspari, G. *The asphericity of random walks. Journal of Physics A: Mathematical and General*, **19**, L191 (1986).

[129] Aronovitz. *Universal features of polymer shapes. Journal de Physique*, **47**, 1445 (1986).

[130] Efron, B. and Tibshirani, R. J. *An introduction to the bootstrap*, volume 57 of *Monographs on statistics and applied probability*. Chapman & Hall, New York (1993).

[131] Cichocki, B. and Hinsen, K. *Dynamic computer simulation of concentrated hard sphere suspensions : I. Simulation technique and mean square displacement data. Physica A: Statistical and Theoretical Physics*, **166**, 473 (1990).

[132] Zaccarelli, E., Foffi, G., Dawson, K. A., Buldyrev, S. V., Sciortino, F., and Tartaglia, P. *Confirmation of anomalous dynamical arrest in attractive colloids: A molecular dynamics study. Physical Review E*, **66**, 041402 (2002).

[133] Babu, S., Gimel, J. C., and Nicolai, T. *Self-diffusion of reversibly aggregating spheres. The Journal of Chemical Physics*, **127** (2007).

[134] Schnell, S. *Reaction kinetics in intracellular environments with macromolecular crowding: simulations and rate laws*1. Progress in Biophysics and Molecular Biology*, **85**, 235 (2004).

[135] Elsner, M., Hashimoto, H., Simpson, J. C., Cassel, D., Nilsson, T., and Weiss, M. *Spatiotemporal dynamics of the COPI vesicle machinery. EMBO Reports*, **4**, 1000 (2003).

[136] Newhouse, J. S. and Kopelman, R. *Steady-state chemical kinetics on surface clusters and islands: segregation of reactants. The Journal of Physical Chemistry*, **92**, 1538 (1988).

[137] Altan-Bonnet, G. and Germain, R. N. *Modeling T Cell Antigen Discrimination Based on Feedback Control of Digital ERK Responses. PLoS Biology*, **3**, e356 (2005).

[138] Schoeberl, B., Eichler-Jonsson, C., Gilles, E. D., and Muller, G. *Computational modeling of the dynamics of the MAP kinase cascade activated by surface and internalized EGF receptors. Nature Biotechnology*, **20**, 370 (2002).

[139] Aldridge, B. B., Burke, J. M., Lauffenburger, D. A., and Sorger, P. K. *Physicochemical modelling of cell signalling pathways. Nature Cell Biology*, **8**, 1195 (2006).

[140] Soetaert, K., Petzoldt, T., and Setzer, R. W. *Solving Differential Equations in R: Package deSolve. Journal of Statistical Software*, **33**, 1 (2010).

[141] R Development Core Team. *R: A Language and Environment for Statistical Computing*. R Foundation for Statistical Computing, Vienna, Austria (2009).

[142] McGuffee, S. R. and Elcock, A. H. *Diffusion, crowding & protein stability in a dynamic molecular model of the bacterial cytoplasm. PLoS Computational Biology*, **6**, e1000694 (2010).

[143] Monine, M. I. and Haugh, J. M. *Reactions on cell membranes: Comparison of continuum theory and Brownian dynamics simulations. The Journal of Chemical Physics*, **123**, 074908 (2005).

[144] Tostevin, F., ten Wolde, P. R., and Howard, M. *Fundamental Limits to Position Determination by Concentration Gradients. PLoS Computational Biology*, **3**, e78 (2007).

Acknowledgments

This work was done at the German Cancer Research Center in Heidelberg between 2007 and 2011. I gratefully acknowledge funding by the Initiative and Networking Fund of the Helmholtz Association within the Helmholtz Alliance on Systems Biology. This work was also supported by the Institute for Modeling and Simulation in the Biosciences (BIOMS) in Heidelberg.

I would like to thank my first supervisor, Prof. Dr. Dieter W. Heermann, for his continuous support and encouraging discussions.

I am especially indebted to my second supervisor and group leader, Prof. Dr. Matthias Weiß, who gave me the great opportunity to dive deeply into biophysical research. The numerous stimulating, reassuring, and insightful discussions carried me through the ups and downs of scientific business.

I thank all the current and former group members of the BIOMS Group Cellular Biophysics at the German Cancer Research Center for the joyful and motivating atmosphere throughout the years. Explicitly, I would like to mention Nina Malchus, Diana Morozova, and Jens Kühnle who improved parts of this manuscript by their critical remarks. I am also much obliged to the Statistical Physics and Theoretical Biophysics Group at the University of Heidelberg. In particular, the science-related and "trivial" discussion with Manfred Bohn were a constant source of motivation and distraction.

I furthermore thank Kathrin Nußbaum and Andreas Kühne for the critical review of the manuscript and the numerous cakes that brightened up so many busy days.

Finally, I am happy to thank my family and my friends for their never-ending moral support that made this work possible in the first place. Especially, the patience and love of Julia and Livia mean more to me than words can express.

Publications

Parts of this work have been submitted for publication separately:

- Marcel Hellmann, Joseph Klafter, Dieter W. Heermann, and Matthias Weiss,
  Challenges in determining anomalous diffusion in crowded fluids,
  Journal of Physics: Condensed Matter
  accepted (2010)
- Marcel Hellmann, Dieter W. Heermann, and Matthias Weiss,
  Anomalous reaction kinetics and domain formation on crowded membranes,
  EPL **94**(1), 18002 (2011)
- Marcel Hellmann, Dieter W. Heermann, and Matthias Weiss,
  Enhancing phosphorylation cascades by anomalous diffusion
  submitted